

Implementation of Grover's Quantum Search Algorithm with Two Trapped Cadmium Ions

by

Kathy-Anne Brickman

A dissertation submitted in partial fulfillment
of the requirements for the degree of
Doctor of Philosophy
(Physics)
in The University of Michigan
2007

Doctoral Committee:

Professor Christopher Monroe , Chair
Professor Paul Berman
Professor Timothy Chupp
Associate Professor Eitan Geva
Assistant Professor David Reis

© Kathy-Anne Brickman 2007
All Rights Reserved

DEDICATION

For my mom and dad

ACKNOWLEDGEMENTS

My graduate school experience here at Michigan has been amazing and that is due, in large part, to the people that I have met and the friends that I have made along the way. First and foremost I need to thank Chris for letting me work in his lab, Chris, thank you so much. In my six years here I have learned more than I could have possibly imagined. When I look back to when I first joined the lab, compared to where I am now the difference, in my mind at least, is unreal. In your lab I had the opportunity to learn about so many different aspects of experimental physics, from microwave sources, to optics and lasers, to atomic physics. Thank you for all of the opportunities you have given me and for supporting me along the way. I feel well prepared for whatever my physics future holds and I am truly grateful.

Next I need to thank all my colleagues especially Louis, Patty, and Paul with whom I worked and from whom I learned the most. Louis and Patty, thank you for showing me the ropes when I first joined the lab and always being there to answer my questions. Paul, thank you for setting an outstanding example for us all. You taught me what it means to be a great scientist through your hard work and dedication. Working on the entanglement experiment with all of you was a great deal of fun even through the late nights and long work weeks.

Two more people I worked closely with were Mark and Ming. Mark joined the entanglement experiment towards the end and then, when that experiment finished, we

both started on the MOT experiemnt. Ming joined us about a year and a half later and made welcome and timely contributions to the MOT search. In the last few months our undergrad, Andrew, has also helped out with the experiment and I appreciate his help building electronics and making us a resonator.

To everyone else in the lab that I did not work with directly, Boris, Winni, Peter, Dzmitry, Russ, David, Martin, Dan, David H., Mark Y., Rudy, Steve, Kelly, Jon, Yisa, Simcha, Dan C., and Liz, thank you for being there to lend a hand, answer questions, or provide a welcome distraction. I also need to thank our visitors, Vanderlei and Jim, who both made helpful contributions to various experiments.

Other people in the physics department that deserve a huge thank you are the staff, especially Kimberly and Michelle. Kimberly, thank you for keeping me on track and helping me with any problems that arose. Michelle, thank you for everything and always remembering our lab when there was free food.

And of course I cannot forget about my friends who were always there for me. Thankyou all so much!

A big thanks needs to go out to family for all their love and support. Thank you mom and dad for everything you have given me and all the sacrifices you made to get me where I am today.

And last but certainly not least I need to thank Mitch. Mitch, thank you for your love and support during the last six years. I would not be where I am today without you.

TABLE OF CONTENTS

DEDICATION	ii
ACKNOWLEDGEMENTS	iii
LIST OF FIGURES	vii
LIST OF TABLES	x
LIST OF APPENDICES	xi
ABSTRACT	xii
CHAPTER	
1. Introduction	1
2. Ion Trapping	7
2.1 RF-Paul Traps Theory	7
2.1.1 Nulling Excess Micromotion	13
2.2 Ion Trap Components	13
2.2.1 The Vacuum System	14
2.2.2 The RF Resonator	14
2.2.3 The Cd atomic oven: metal vs. oxide ovens	17
2.2.4 Creating Ions	17
3. Cd as a qubit	21
3.1 Energy levels of Cd-111	21
3.2 Experimental Set-up	26
3.2.1 The laser system	26
3.2.2 Imaging System	31
3.2.3 Computer Control	31
4. Coherent single qubit operations	38
4.1 Single Qubit Operations	39
4.2 Accessing the motional levels	42
4.3 Microwave Transitions	44
4.4 Stimulated Raman Transitions	45
4.5 Implementing Stimulated Raman Transitions	50
4.6 Creating the Raman beams with an EOM	52
4.7 Ground State Cooling	55

5. Two-ion Entangling Gates	60
5.1 Cirac and Zoller Gate Scheme	60
5.2 Spin Dependent Forces	61
5.2.1 Spin Dependent Forces	61
5.2.2 σ_z force	64
5.2.3 σ_ϕ force	68
5.2.4 Producing the sideband frequencies	69
5.2.5 Testing the σ_ϕ force on a single ion	71
5.3 Geometric Phase Gates	77
5.3.1 Molmer-Sorensen Gate	80
5.4 Characterizing the performance of the gate	84
6. Quantum Algorithms	93
6.1 Quantum Algorithms	93
6.1.1 Deutsch-Jozsa Algorithm	93
6.1.2 Shor's Factoring Algorithm	95
6.1.3 Grover's Search Algorithm	96
6.2 Experimental Implementation of Grovers Algorithm	97
7. The Magneto-optical Trap	105
7.1 Introduction	105
7.2 Background	106
7.3 Experimental Set-up and Procedure	109
7.4 Results and Discussion	112
7.5 Fermionic Isotopes	116
7.6 Conclusion	119
8. Conclusion	120
APPENDICES	122
BIBLIOGRAPHY	133

LIST OF FIGURES

Figure

2.1	Two types of rf Paul traps used in this thesis work.	8
2.2	Four rod linear ion trap.	12
2.3	Vacuum chamber housing the linear rf trap.	15
2.4	Quarter wave helical resonator.	16
2.5	Top: A stainless steel and alumina oven with a tungsten coil.	18
2.6	Energy level diagram of neutral Cd.	20
3.1	Energy level diagram of $^{111}\text{Cd}^+$	22
3.2	The eight stable isotopes of Cd.	24
3.3	Initialization and detection energy level diagrams for Cd.	25
3.4	Detection laser system.	26
3.5	Tellurium setup for laser feedback.	28
3.6	AOM frequencies to generate the initialization, detection, and Doppler cooling beams. .	29
3.7	Raman laser system.	32
3.8	Energy level diagram for the Raman transitions.	33
3.9	Schematic diagram of the pulsed laser system.	33
3.10	Typical experimental pulse sequence.	35
3.11	Detection histograms for a single ion.	36
3.12	Detection histograms for two ions.	37
4.1	Representation of the Bloch sphere	42
4.2	Microwave Rabi flopping for the carrier and Zeeman transition.	46
4.3	Top: Energy level diagram for the Raman transitions.	47
4.4	Effect of AC Stark shift on qubit levels.	49

4.5	Energy level diagram for a motional stimulated Raman transition.	51
4.6	Raman beams going into the chamber.	52
4.7	Electric dipole transition probabilities from the $S_{1/2} \rightarrow P_{3/2}$ manifolds.	53
4.8	AO scan showing the frequency spectrum of the Raman transitions.	56
4.9	Raman cooling scheme.	57
4.10	Spectrum of a Doppler cooled and Raman cooled ion for a trap frequency $\omega_x/(2\pi) = 5.8$ MHz.	59
5.1	Energy level and phase space diagram for the σ_z gate.	65
5.2	σ_z signal vs. detuning for a single ion.	68
5.3	Two possible Raman beam set-ups to create the Mølmer-Sørensen σ_{phi} gate on a single ion.	70
5.4	Final calibration method for setting the red sideband and blue sideband detunings, δ_r and δ_b , repsectively.	71
5.5	Probability for the ion to be in the bright state vs. detuning of the σ_ϕ force for (a) a ground state cooled ion and (b) a Doppler cooled ion, initially prepared in the $ \uparrow\rangle$	73
5.6	Single ion evolution from σ_ϕ force.	74
5.7	Demonstration of the phase sensitivity of the σ_ϕ force for different Raman beam configurations.	78
5.8	Two views of the Mølmer-Sørensen entangling gate for two ions in (a) energy space [23] and (b) motional phase space [29] for the gate-diagonal spin basis.	81
5.9	Signal from the M-S entangling gate as the detuning is scanned.	84
5.10	Signal from the M-S entangling gate as the gate duration is scanned.	85
5.11	Detection histograms for the state after applying the M-S gate.	86
5.12	Parity vs. phase of analysis $\pi/2$ pulse applied to the Ψ_1 state.	87
5.13	Laser beam generating differential Stark shift and phase scan showing the two ions out of phase with each other.	88
5.14	Tomography of the state directly after the M-S gate for the four possible input states. .	90
5.15	State preparation for the $ \downarrow\downarrow\rangle$ and $ \downarrow\uparrow\rangle$ states.	91
6.1	Circuit diagram to implement Shor's algorithm.	95
6.2	Schematic diagram of Grover's quantum search algorithm over a space of n qubits ($N = 2^n$ entries).	98
6.3	Quantum circuit to implement Grover's searching algorithm for N=4 entries [37].	99
6.4	(a.) Output of the algorithm.	102

7.1	Cadmium energy level diagram (not to scale).	107
7.2	Left: Schematic diagram of the laser system and the laser lock (DAVLL).	110
7.3	Left: Typical loading curve showing the buildup in the MOT fluorescence vs. time. . . .	112
7.4	Observed steady-state MOT number vs. axial magnetic field gradient B' (points), along with the 3-D model (solid line) for $P=0.8$ mW, $\delta=-0.6$, and $w=2.5$ mm.	113
7.5	Atom cloud rms diameter vs. B' for $P=0.8$ mW, $\delta=-0.6$, and $w=2.5$ mm.	114
7.6	Observed steady-state atom number vs. δ (points) along with the 1-D (dotted line) and 3-D (solid line) models for $P=1.8$ mW, $B'=500$ G/cm and $w=2.5$ mm.	115
7.7	Observed steady-state atom number vs. power (points) for $\delta=-0.7$, $B'=500$ G/cm and $w=2.5$ mm along with the 1-D (solid line) and 3-D (dotted line) models.	115
7.8	MOT cloud diameter vs. total MOT laser power for $\delta=-0.6$, $B'=500$ G/cm and $w=2.5$ mm.	115
7.9	Top: Observed trapped atom number $N(t)$ for two different Cd background vapor pressures.	116
7.10	Observed loading rate vs the saturation parameter $s=I/I_{sat}$	117
7.11	Top: Scan across frequency showing the different Cd isotope MOTs.	117

LIST OF TABLES

Table

4.1	Truth table for both single and multi-bit classical and quantum gates.	39
5.1	Projective measurement for tomography.	88

LIST OF APPENDICES

Appendix

A.	Raman Beam Effects: Rabi Flopping, Spontaneous Emission, and the AC Stark Shift . . .	123
A.1	Raman Beam Effects	123
A.2	Rabi Flopping	123
A.2.1	Mach-Zehnder contribution	124
A.2.2	Polarization	125
A.3	Spontaneous Emission	127
A.4	Stark Shift	127
B.	Decoherence Effects: Temperature and Heating	129
B.1	Decoherence from temperature and heating	129
B.2	Temperature	129
B.3	Heating	130
C.	1-D Cooling Model and 3-D Monte Carlo simulation	131
C.1	1-D derivation for steady-state number of atoms cooled to rest in a vapor cell . .	131

ABSTRACT

Implementation of Grover's Quantum Search Algorithm with Two Trapped Cadmium Ions

by
Kathy-Anne Brickman

Chair: Christopher Monroe

Over the past decade, the field of trapped ion quantum computing has emerged as one of the leaders in quantum information processing due the level of manipulation available and the long coherence times possible in the system. As this thesis will demonstrate, all of the necessary building blocks for a quantum computer have been exhibited in ion traps and small scale quantum algorithms have been implemented in this system.

In the trapped ion system presented here, quantum bits (qubits) consist of the first order magnetic field insensitive ground state hyperfine levels of $^{111}\text{Cd}^+$. The qubits are manipulated via both resonant and off-resonant coherent laser interactions. We experimentally realize Grover's quantum search algorithm over a space of $N=4$ elements with $n=2$ trapped $^{111}\text{Cd}^+$ ion qubits. One of the four states is marked, and with a single query it is recovered, on average, with a 60% probability. This exceeds the performance of any possible classical search, which can only succeed with 50% probability following a single query. The algorithm consists of two Molmer-Sorensen entangling gates, that utilize bichromatic stimulated Raman transitions to create a spin dependent force on the ions, paired with several single-qubit rotations and near-perfect qubit measurements. The spec-

tral arrangement of the Raman beams is tailored to suppress phase noise accumulation between gates. This suppression is critical for reliably performing consecutive operations during the algorithm.

Additionally, this thesis discusses the possibility of combining trapped ions with trapped neutral atoms for the purpose studying ultra-cold charge exchange interactions. It may be possible to conceal quantum information, initially prepared in an ionic qubit, inside a pure nuclear spin qubit for the purpose of transportation and storage. As a first step towards this investigation, we present the laser-cooling and confinement of Cd atoms in a magneto-optical trap, and characterize the loading process from the background Cd vapor. The trapping laser drives the $^1S_0 \rightarrow ^1P_1$ transition at 229 nm in this two-electron (valence electron) atom and also photoionizes atoms directly from the 1P_1 state. This photoionization overwhelms the other loss mechanisms and allows a direct measurement of the photoionization cross section, which we measure to be $2(1) \times 10^{-16} \text{ cm}^2$ from the 1P_1 state.

CHAPTER 1

Introduction

“When we get to the very, very small world—say circuits of seven atoms—we have a lot of new things that would happen that represent completely new opportunities for design. Atoms on a small scale behave like nothing on a large scale, for they satisfy the laws of quantum mechanics. So, as we go down and fiddle around with atoms down there, we are working with different laws, and we can expect to do different things. We can manufacture in different ways. We can use, not just circuits, but some system involving the quantized energy levels, or the interactions of quantized spins, etc.”

It was this truly visionary statement by Richard Feynman in 1959 that jump started the field of quantum computing [1]. About twenty years later, Benioff and Feynman showed that, even at the atomic scale, classical bits could still be stored and manipulated [2, 3]. However, after technology reaches this point there will be no way to make circuits any smaller and something more will need to happen to increase the speed and capacity of computers. Shrinking classical bits to the atomic scale allows us to take advantage of a much more powerful mechanism since, on this small scale, particles are governed by the laws of quantum mechanics. Classically, bits can be stored in either the 0 or the 1 state, but quantum particles can be prepared in superposition states of 0 and 1. This allows

us to encode 2^N states with N quantum bits (qubits). The problem is that measuring the system collapses the superposition into an arbitrary state and gives a random result. However, in 1985, David Deutsch introduced a new way to think about quantum bits and their interactions [4]. He presented the concept of quantum parallel processing and showed that, by using quantum entanglement and quantum interference, it is possible to compute a function that simultaneously acts on a superposition of all 2^N input states and results in a single coherent output state that depends on *all* the input states. Not too long after Deutsch's discovery, in 1994, Peter Shor developed a quantum factoring algorithm capable of factoring large numbers exponentially faster than any known algorithm run on a classical computer [5]. If realized, this algorithm would be a major threat to most of the current encryption schemes, since they rely on the inability of classical computers to factor large numbers. After Shor presented this algorithm, there was an explosion in the number of groups working towards a quantum computer.

Among these is the field of trapped ion quantum computing, which got its start in 1995 when Cirac and Zoller proposed the first entangling gate scheme for trapped ions [6]. Later that same year, the gate was realized experimentally on a single trapped beryllium ion [7]. The work done for atomic frequency standards made the jump from spectroscopy to quantum computing a fast one for trapped ions, since many of the necessary techniques had already been accomplished for atomic clocks [8]. Since 1995 the field of trapped ion quantum computing has come a long way and is one of the current leaders in the development of a full scale quantum computer.

As stated earlier, researches at NIST demonstrated the first trapped ion entangling gate in 1995 by utilizing the scheme laid out by Cirac and Zoller that involves entangling the ions' spin states through the collective motional mode. In 1996 the first qubit register was initialized through ground state cooling and later in that same year a single ion

Schrödinger cat state was created. In 1998 further control over trapped ions was gained when ground state cooling was achieved for the motional modes of two trapped Be^+ ions. Over the years several two ion entangling gates have been realized. They include the Cirac-Zoller gate [Schmidt-Kaler, Nature], a geometric phase gate proposed by Mølmer and Sørensen that acts in the x-basis, and a similar geometric phase gate that acts in the z-basis proposed by Milburn, Schneider, and James[ref CZ, MS, milburn, Sackett Nature, Liebfried Nature]. In 2003 the first quantum algorithm was preformed on a single ion by the Innsruck group. They showed an implementation of the Deutsch-Jozsa algorithm on a single trapped Ca^+ ion. In 2004 the group at NIST implemented a teleportation algorithm on three trapped ions. Grover's quantum search algorithm was performed on two trapped Cd^+ ions at Michigan in 2005. And in that same year NIST showed a six ion Schrödinger cat state and the Innsbruck group entangled eight ions simultaneously.

The last big task left for trapped ion quantum computing is to scale the system up to arbitrary numbers of qubits. Current efforts towards this include fabricating multi-zone ion trap arrays that occupy less volume and hold more qubits [Mich, NIST].

In 2000 David DiVincenzo outlined the requirements for a large scale quantum computer for any system [9]. They are:

1. A scalable system with well characterized quantum bits (qubits).
2. The ability to initialize the state of the qubits.
3. Long, relevant decohherence times, much longer than gate operation times.
4. A universal set of quantum gates.
5. A qubit specific measurement.

In this thesis I will show how all of the DiVincenzo requirements have been fulfilled in trapped cadmium (Cd) ions, and how they are combined to perform Grover's quantum

database search algorithm over a four element database. In addition I will present a system that combines trapped ions with trapped neutral atoms for the purpose of studying ultra-cold charge exchange collisions.

In order to have a good system for quantum computing you need a qubit that is well shielded from the environment but that can be strongly coupled to the environment for readout. Rf Paul traps allow this to be carried out in trapped ion quantum computing. Chapter 2 describes how these ion traps work and the necessary components to build a trapped ion experiment. In particular I show a novel three layer ion trap geometry that allows for good control over the ions by allowing stray fields and excess micromotion to be nulled. The other equipment needed for a trapped ion system is also discussed, this includes the vacuum system, the rf resonator, and an atomic Cd source.

The next three chapters focus on how Cd is manipulated with laser interactions and describes how all of the above requirements are met in this system. The quibits reside in the ground state hyperfine levels of $^{111}\text{Cd}^+$ ions. Due to the simple structure of Cd operations such as detection and initialization can be accomplished with high fidelity, this will be discussed in more detail in Chapter 3. Chapter 4 discusses single quibit operations and outlines the protocol for ground state cooling. Ground state cooling is important because many of the entanglement schemes require that the ions be cooled to near the ground state of motion. The reason for this is so that the ions wavepacket will be well localized compared to the wavelength of the applied light. If the ion wavepacket extends further than the wavelength of the light, then different parts of the ion will feel different phases of the applied light. This will lead to excess decoherence in the system.

Chapter 5 concentrates on two-ion entanlging gate schemes and in particular deomonstrates the realization of a gate scheme first proposed by Mølmer and Sørensen. In this gate scheme we apply bichromatic light to the ions which allows us to entangle the spin

states of the ions through a collective motional mode. Although this type of gate has been previously demonstrated, the version described here is the first implementation with the ability to cancel excess phase noise that can occur during the gate evolution. We achieve this by choosing the correct spectral arrangement of the bichromatic beams that generate the gate. This is an advantageous feature of the gate since extra phase noise can lead to decoherence in the system and degrade the fidelity of the operations. In addition this gate acts on the magnetic field insensitive ground state hyperfine levels in $^{111}\text{Cd}^+$, the $|F = 0, m_F = 0\rangle$ and $|F = 1, m_F = 0\rangle$ states. This may make it a more desirable entanglement scheme due to the longer coherence time of these states in the presence of magnetic fields. This is in comparison to the qubit states in other systems that rely on Zeeman levels which are more susceptible to magnetic field fluctuations.

In chapter 6 all the requirements are combined to implement Grover's quantum search algorithm on two trapped Cd ions. We perform a search over a four element database and find the desired state with 60% fidelity. The algorithm shows how the phase interference between two entangling gates can constructively interfere to produce a single outcome that relies on all four input states. Although the search space is rather trivial, this algorithm can be scaled up to an arbitrary number of qubits without exponential overhead in the amount of operations or resources required. The implementation of the algorithm shown in this thesis is meant as a proof of principle demonstration.

The last chapter introduces a new system to combine trapped ions with neutral atoms trapped in a magneto-optical trap for the purpose of studying ultra-cold charge exchange collisions. It is possible that this system could be used to conceal quantum information in the nuclear spin of a neutral atom. As a first step towards this we present a characterization of the first neutral cadmium magneto-optical trap. This MOT is unique because the same laser beams that form the MOT can also cause atoms to be photoionized inside

the MOT. This leads to an additional loss term, and in this case the photoionization loss is the dominant loss term. As a result we are able to measure the photoionization cross section for Cd from the 1P_1 state using 229 nm photons.

CHAPTER 2

Ion Trapping

Although there are many ways to trap an ion, the radio frequency (rf) or “Paul” trap is an ideal candidate for the purpose of trapped ion quantum computing. To create a robust quantum computer the qubits must be well shielded from the environment for most operations but capable of having a strong interaction to the environment for measurement purposes. In addition, the qubits must be strongly coupled to each other. The radiofrequency ion traps presented in this chapter prove to be a viable system to fulfill these requirements.

2.1 RF-Paul Traps Theory

We use traps employing an electric quadrupole field with an oscillating rf potential. This type of rf trap, or “Paul” trap, is credited to work done by Wolfgang Paul and Hans Dehmelt in the 1950’s [10]. Two types of traps used in this thesis are an asymmetric “ring and fork” quadrupole trap and a three layer linear trap shown in Fig. 2.1.

For the ring and fork trap we apply an rf voltage $V_0 \cos(\Omega_{rf} t)$ to the ring and a static potential U_0 is applied to the endcaps (the fork). This results in an assymetric quadrupole

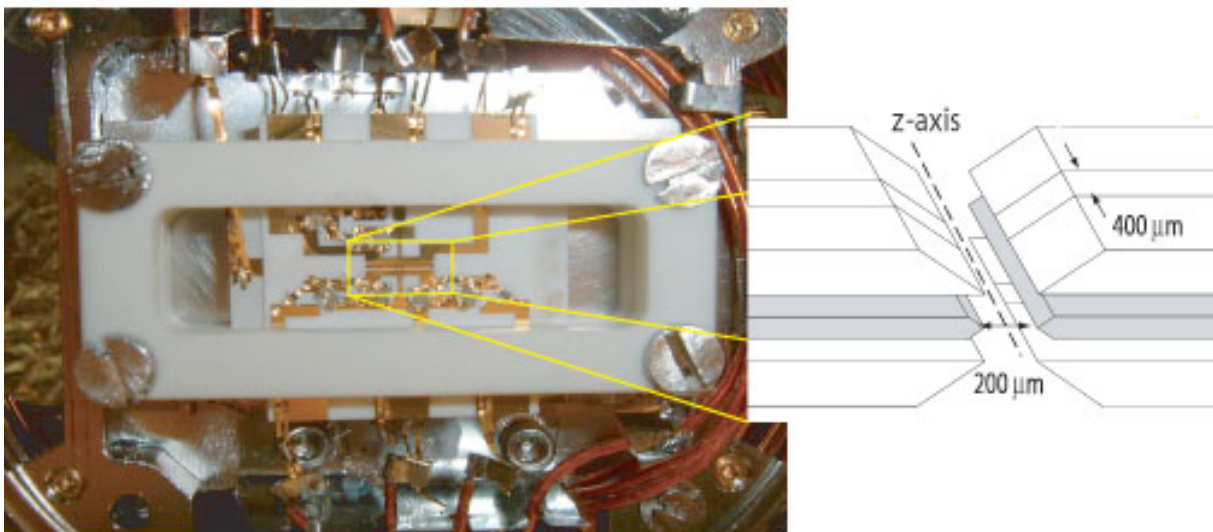
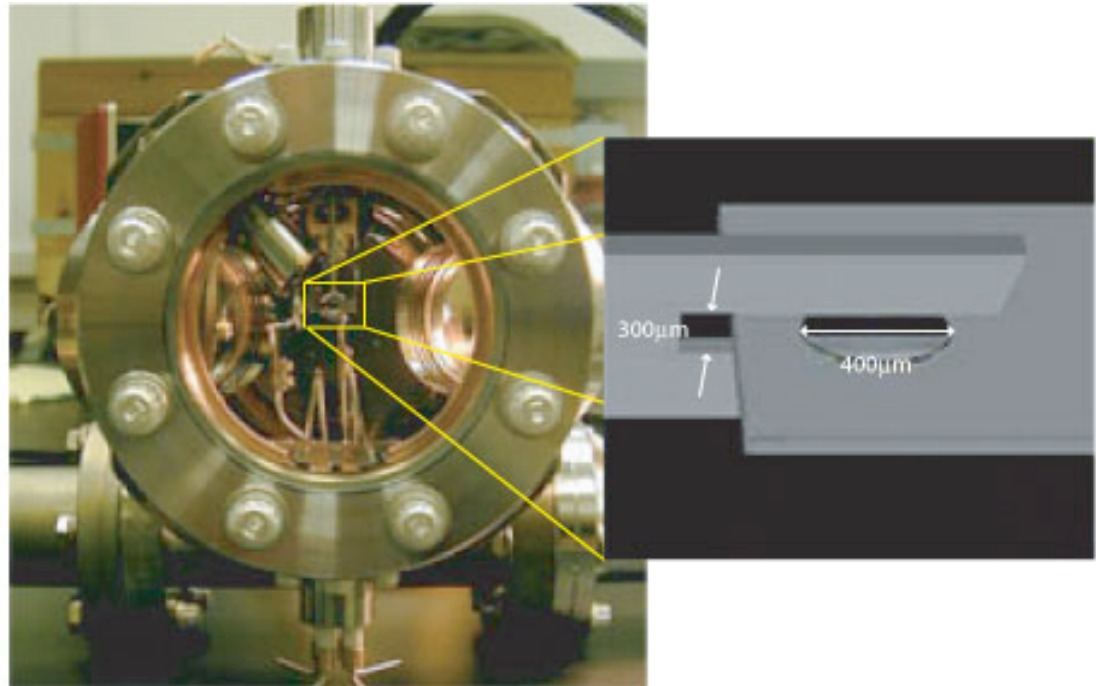


Figure 2.1: Two types of rf Paul traps used in this thesis work. The top trap is an asymmetric quadrupole trap consisting of a ring electrode and a fork electrode. The ring electrode has a diameter of $400 \mu\text{m}$ and the slit in the fork is $300 \mu\text{m}$ wide. The resulting potential from this geometry is an rf node that is a single point in space. The bottom ion trap is a 3-layer linear rf trap. The middle layer is a continuous rf electrode and the outer layers are segmented dc electrodes. The top and bottom layers are $250 \mu\text{m}$ thick while the middle layer is $125 \mu\text{m}$ thick. Each layer is separated by a $125 \mu\text{m}$ alumina spacer (not shown). The gold coating on each layer is approximately $0.3 \mu\text{m}$ thick. This geometry results in a linear node producing linear ion crystals.

potential near the trap center given by

$$V(x, y, z, t) = \kappa [U_0 + V_0 \cos(\Omega_{rf}t)] \left[\frac{\alpha x^2 + (2 - \alpha)y^2 - 2z^2}{d_0^2} \right] \quad (2.1)$$

where α and κ are determined by the electrode geometry and for the case of the ring and fork $\alpha \simeq \kappa \simeq 0.8$, $d_0^2 = r_0^2 + 2z_0^2$, where r_0 is the radius of the ring electrode and $2z_0$ is the spacing of the endcaps, and Ω_{rf} is the rf drive frequency. The equations of motion for a single ion of mass m and electric charge e are

$$\ddot{x} + \frac{2e\alpha\kappa}{md_0^2}(U_0 + V_0 \cos(\Omega_{rf}t))x = 0 \quad (2.2)$$

$$\ddot{y} + \frac{2e(2 - \alpha)\kappa}{md_0^2}(U_0 + V_0 \cos(\Omega_{rf}t))y = 0 \quad (2.3)$$

$$\ddot{z} - \frac{4e\kappa}{md_0^2}(U_0 + V_0 \cos(\Omega_{rf}t))z = 0. \quad (2.4)$$

These equations can be transformed into the Mathieu equation [11] and if we look at the motion in only the x direction we get the dimensionless equation

$$\frac{d^2x}{d\tau^2} + (a + 2q \cos(2\tau))x = 0, \quad (2.5)$$

here

$$a = \frac{8eU_0\alpha\kappa}{md_0^2\Omega_{rf}^2} \quad (2.6)$$

$$q = \frac{4eV_0\alpha\kappa}{md_0^2\Omega_{rf}^2} \quad (2.7)$$

$$\tau = \frac{\Omega_{rf}t}{2}. \quad (2.8)$$

To lowest order the solution to eqn 2.5 is

$$x(t) = x_0 \cos(\omega_x t) [1 - \frac{q}{2} \cos(\Omega_{rf}t)] \quad (2.9)$$

where x_0 depends on the initial conditions and $\omega_x = \sqrt{(a + q^2/2)\Omega_{rf}/2}$.

Equation 2.9 contains two parts: the secular frequency oscillating at ω_x , and a faster micromotion component oscillating at the rf drive frequency Ω_{rf} . If we assume that $a \ll q^2 \ll 1$ and $U_0 \approx 0$, then the micromotion term is suppressed by a factor of $q/2$ compared to the secular motion and can be neglected. In this case the motion of the ion is well approximated as a simple harmonic oscillator with oscillation frequency ω_x .

In practice the ring and fork trap is constructed from two thin sheets of molybdenum metal, one with a hole drilled through it to form the “ring” electrode, and the other has a large slit providing the “fork” electrode. Each sheet is $125\mu\text{m}$ thick, the radius of the ring electrode is $200\mu\text{m}$ and the gap in the fork is $300\mu\text{m}$. There are additional compensation electrodes used to null the excess micromotion, a topic that will be discussed later in the chapter.

The linear trap is best modeled by thinking of four segmented parallel rods along the z-direction, as shown in fig. 2.2. The ions are trapped by superimposing two different confining potentials to the trap electrodes, an rf potential and a static potential. All of the electrodes provide a confining ponderomotive potential in the x and y directions, while the outer electrodes serve as “endcaps” and confine the ions along the z-direction.

For the transverse confinement the potential $V_0\cos(\Omega_{rft}) + U_t$ is applied to the rf electrodes. To ensure that each rod segment has the same rf potential the segments are capacitively coupled to each other. Near the axis of the trap the potential is

$$V_t(x, y) = \frac{\beta(V_0\cos(\Omega_{rft}) + U_t)}{2} \left(1 + \frac{x^2 - y^2}{R^2}\right) \quad (2.10)$$

where β is a geometric factor, V_0 and U_t are the applied transverse rf and static voltages, Ω_{rf} is the rf drive frequency, and R is the distance from the trap center to the nearest

electrode. The U_t term is important to break the symmetry in the x and y directions so there are well defined transverse principle axes of motion [12].

For confinement in the z-direction a static voltage U_0 is applied to the eight outer electrodes. The resulting potential is

$$V_{DC}(x, y, z) = \frac{\kappa U_0}{z_0^2} [2z^2 - x^2 + y^2] = \frac{m\omega_z^2}{2e} [2z^2 - x^2 + y^2] \quad (2.11)$$

where κ is a geometric factor and $\omega_z/2\pi$ is the longitudinal trap frequency

$$\omega_z = \sqrt{\frac{2eU_0\kappa}{mz_0^2}}. \quad (2.12)$$

The secular frequencies for this trap are

$$\omega_{x,y} = \sqrt{\left(\frac{\beta e V_0}{\sqrt{2m}\Omega_{rf}R^2}\right)^2 - \frac{\kappa e U_0}{mz_0^2} \pm \frac{\beta e U_t}{mR^2}} \quad (2.13)$$

where \pm denotes the x and y directions respectively.

This DC potential results in an anti-trap along the transverse directions x and y, but the ponderomotive rf potential easily overwhelms this anti-trapping effect from the static voltage U_0 .

The advantage of linear traps over 3D quadrupole traps is that these traps have a linear rf node along which the ions line up, whereas in the ring and fork trap the rf node is a single point in space. If there are more than a few ions trapped in the ring and fork trap they will bunch up at the center and this makes individually addressing and controlling the ions collective (secular) motion difficult.

In practice the linear trap we use has a different geometry than the four rod trap described above, but the physics is identical. Instead of four segmented rods, the linear trap used in the experiments has a three layer geometry as shown in figure 2.1. The middle

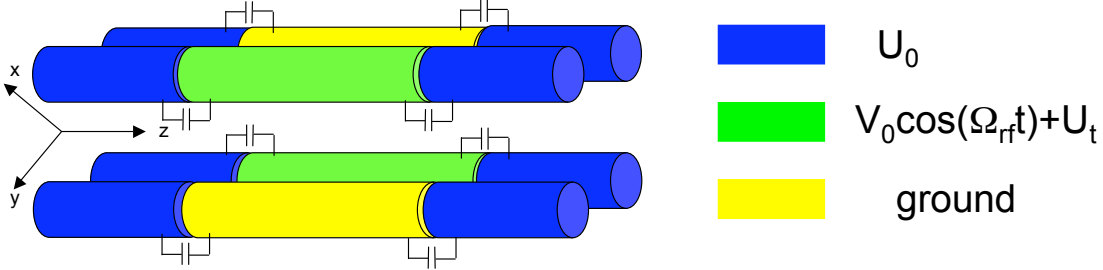


Figure 2.2: Four rod linear ion trap. The potential $V_0\cos(\Omega_{rf}t) + U_t$ is applied to two of the four inner electrodes to create the alternating confining potential and the other two inner electrodes are grounded. The static component, U_t , on the rf electrodes breaks the symmetry in x and y to allow for efficient Doppler cooling. Static voltages are applied to the outer electrodes to create confining endcaps in the z -direction.

layer is a continuous rf electrode and the outer two layers are segmented dc electrodes. Each dc layer is separated into six electrodes which can be individually controlled. Individual control of the dc electrodes is important because it allows excess micromotion, which will be discussed in the next section, to be cancelled. The inner dc electrodes are $400 \mu\text{m}$ wide and separated by $200 \mu\text{m}$. The trap is fabricated from laser machined gold plated alumina. Typically a potential with amplitude $V_0 \approx 400 \text{ V}$ is applied to the rf electrodes, yielding trap frequencies of $\omega_x/2\pi \sim 8.1 \text{ MHz}$ and $\omega_y/2\pi \sim 8.3 \text{ MHz}$. Typical rf driving frequencies are on the order of 50 MHz . Typical dc voltages range from 5 V to 275 V between the inner and outer segments, this results in a range of longitudinal trap frequencies from $\omega_z/2\pi = 400 \text{ kHz}$ to 4 MHz . The advantage of a three layer geometry over a four rod geometry is the ability to compensate for stray fields in any direction and it allows for more complicated geometries, such as T-junctions, which have been helpful in other trap iterations where multiple trapping zones are needed [13].

2.1.1 Nulling Excess Micromotion

If there are any static background electric fields present at the trapping location, then equation 2.5 becomes

$$\frac{d^2x}{d\tau^2} + (a + 2q\cos(2\tau))x = \frac{eE_0}{m} \quad (2.14)$$

this assumes an electric field with a component E_0 along the x-direction. The solution to equation 2.14 is

$$x(t) = x_0\cos(\omega_x t)[1 - \frac{q}{2}\cos(\Omega_{rf}t)] + \frac{eE_0}{m\omega_x^2} + \frac{\sqrt{2}eE_0\cos(\Omega_{rf}t)}{m\omega_x\Omega_{rf}}, \quad (2.15)$$

which is similar to eqn. 2.9, but has two additional terms. The second term in eqn. 2.15 represents a constant offset xE_0 in the ion position that pushes the ion away from the rf zero. The third term is a component driven at Ω_{rf} which leads to excess micromotion in the ion. This micromotion differs from the micromotion present in the second term in that it is a driven motion proportional to the background electric field E_0 . The amplitude of this motion could be larger than the secular motion of the ions and therefore it can inhibit laser cooling due to excess Doppler broadening of the spectrum. To cancel the constant offset term and null this extra micromotion requires either additional compensation electrodes, in the case of the ring and fork trap, or different electrode geometries, such as the three layer linear trap.

2.2 Ion Trap Components

Other than the trap itself, there are several other crucial pieces needed to realize an ion trap system. An ultra-high vacuum is necessary so that stray background particles do not collide with the ion and cause unwanted charge exchange interactions. An rf resonator is

needed to provide the high trapping voltages and, lastly, there must be a source of Cd inside the vacuum chamber to produce ions.

2.2.1 The Vacuum System

The ion trap is housed in a vacuum chamber pumped down to below 10^{-11} torr. This low pressure limits the number of background gas collisions, which can result in charge exchange interactions with the trapped ion. The chamber itself, shown in Fig. 2.3, has a 4 1/2" front window and 2 smaller windows positioned at 45° from the equator and forming a 90° with each other. The windows allow the necessary optical access to address the ions. Each chamber has its own ion pump with pumping speed of 20 L/sec, a Ti-Sublimation pump, and an ion gauge to monitor the chamber pressure.

To achieve such low pressures, great care must be taken when assembling the vacuum system. First, all the pieces are cleaned in an ultrasonic cleaner and then the stainless steel pieces are prebaked for a few days at 350 degrees C. The system is assembled and the entire chamber is baked to 225° C. During the bake the system is pumped out with an external 500 L/sec ion pump. Typically the chamber is left at 225° C for several days, this is mainly to get rid of any water that may be present.

2.2.2 The RF Resonator

An rf resonator produces the necessary voltages to drive the alternating trapping potentials in the ion trap. A quarter wave helical resonator [14] converts approximately 2W of rf power to several hundred volts giving tens of MHz secular frequencies in the ion trap. The resonator, shown in Fig. 2.4, is attached to the trap electrodes through a vacuum feedthrough. Typically the feedthrough limits how much voltage can be applied to the trap since the feedthrough breakdown voltage is a few thousand volts. A helical coil placed inside a copper cylinder comprises the resonator. The rf source is inductively coupled to

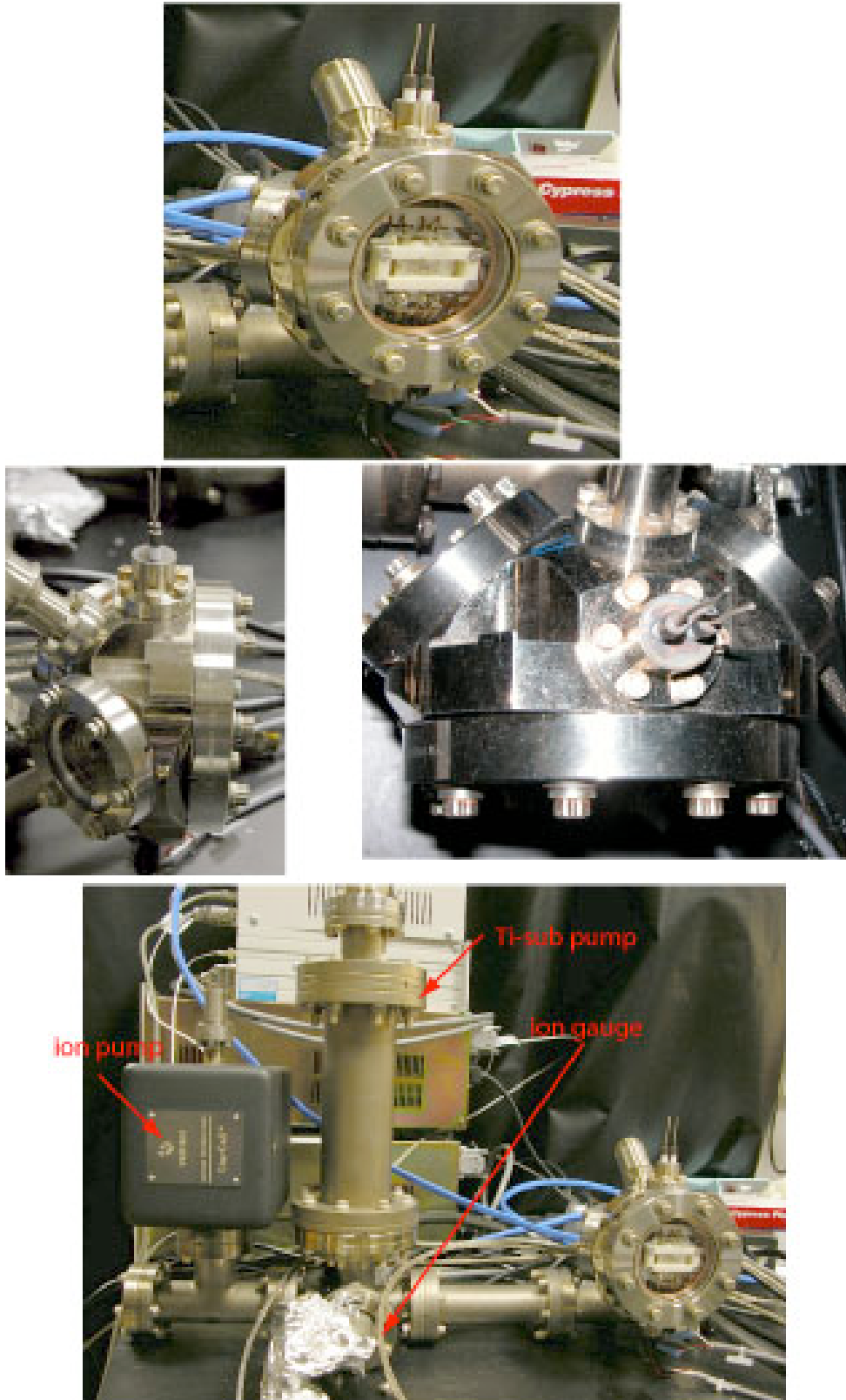


Figure 2.3: Vacuum chamber housing the linear rf trap. The front window is 4.5" across and the two side windows are 2.75". The smaller side windows are positioned at 45° degrees from the front window and make a 90° with each other, this is to allow sufficient optical access. The chamber also has an ion pump, a Ti-sublimation pump, and an ion gauge to monitor the pressure.

the resonator via an additional coil attached to the cylinder lid, see fig. 2.4. This coil loop allows the final coupling to be accomplished in situ. Changing the spacing between the smaller coil and the main resonator coil changes the inductance between the two coils and this allows one to maximize the power coupled into the resonator. As a day to day gauge for the transmitted power into the resonator, the power reflection is monitored on an oscilloscope. Typical loaded resonator Q's are greater than 300, this gives about 200 V at the trap. Since the rf electrodes must sometimes be biased with static potentials, care is taken to isolate the electrodes by placing ' π '-filter networks between the static power supplies and the resonator.



Figure 2.4: Quarter wave helical resonator. The resonator is composed of a copper helical coil placed inside a copper cylinder. There is an additional coil loop attached to the lid of the cylinder to allow for the coupling between the rf source and the resonator.

2.2.3 The Cd atomic oven: metal vs. oxide ovens

To produce Cd in the vacuum chamber a small oven is placed inside the chamber to create a Cd atomic beam. There are two types of ovens, stainless steel ovens filled with metal Cd and alumina ovens wrapped with a tungsten filament filled with CdO powder. The stainless steel ovens are produced with about a 1 cm long hypodermic needle tube having an inner diameter of 0.09 cm and an outer diameter of 0.11 cm. One end of the tube is crimped and spot welded shut and then filled with 0.02 grams of metal Cd. The oxide ovens are constructed from a 1 cm long piece of alumina with an inner diameter of 0.12 cm and an outer diameter of 0.20 cm. One end of the alumina tube is sealed shut with an oxygen/natural gas torch so that no Cd leaks out of the back. The oven is wrapped with tungsten forming about 10 windings on the alumina tube and filled with CdO. Alumina ovens must be used for CdO since its melting point is about 5 times higher than that of Cd (1773 K compared to 593 K), and the stainless steel oven cannot get hot enough to melt the oxide. When stainless steel ovens with natural Cd are used, there is a noticeable layer of Cd coating the trap electrodes at the end of the bake. This could be detrimental to the ion trap because it could cause an electrical short between the trap electrodes. However, if CdO is used, there is no noticeable layer of Cd on the electrodes as seen in Fig. 2.5.

2.2.4 Creating Ions

To create ions, neutral Cd atoms, produced from the ovens, are directed towards the center of the ion trap where they are ionized and trapped. Several methods have been used over the years to ionize Cd inside the trap. The first method uses electron bombardment where an electron gun is fired towards the center of trap near the Cd atomic beam. The electron gun is simply a tungsten filament that is resistively heated by running a current

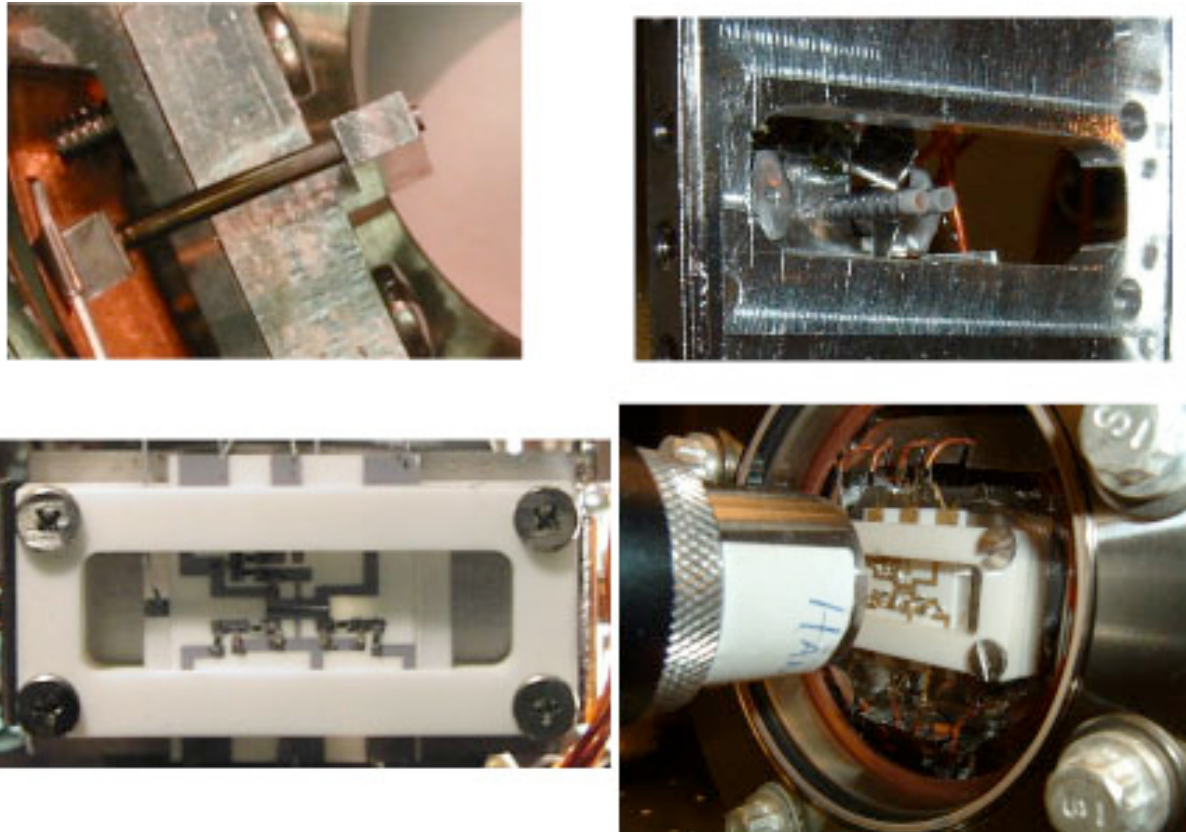


Figure 2.5: Top: A stainless steel and alumina oven with a tungsten coil. Bottom: Two different chambers after completing the bake. The chamber on the lower left had a Cd metal oven inside and its electrodes are covered in a dull gray coating. This is a layer of Cd that has formed during the bake. The chamber in the lower right used a CdO oven and the electrodes are still gold. Since CdO has a much higher melting point than Cd, no noticeable layer of Cd is emitted during the bake.

through it. The high energy electrons emitted from the filament are accelerated through a hole in a metallic plate that sits in front of the filament and is biased at about -130 V. An electron striking a neutral Cd atom removes one of the outer electrons and creates an ion. Though effective, this method is not terribly efficient and it is detrimental to the vacuum pressure since it causes the pressure to rise several orders of magnitude. After trapping an ion, you must wait 20-30 minutes for the vacuum pressure to recover before addressing the ion. The pressure rise is due to the heat generated by the electron guns when they are fired. A second way to trap Cd ions is to direct the detection beam onto the metal trap electrodes and then move the laser beam back to the center of the trap. Often times when this process is repeated, an ion is trapped after a few minutes. Presumably, this is because the work function of the ultra-violet (UV) photons is large enough to strip an electron off of the metal electrode surface. This electron can then ionize a nearby neutral Cd atom inside the ion trap. Although this method does not disrupt the vacuum and is a reliable way to trap an ion, it is a very slow process. It could take up to an hour or more to trap a single ion in this manner. When more than one ion is needed, this process becomes too slow and often, while trying to trap a second ion, the first ion is lost. The third most reliable and least invasive method at creating ions is to directly photoionize the atoms inside of the ion trap. Fig. 2.6 shows the energy level diagram for neutral Cd. A 229 nm photon can excite the atom from the ground state, 1S_0 , to the first excited state, 1P_1 , and a second photon of the same color can ionize the atom directly from the 1P_1 state. A pulsed laser operating at 915 nm is quadrupled to produce the 229 nm ionization beams. When the pulsed laser is directed into the trap many ions can be trapped in a few seconds, which is useful for multi-ion experiments. An additional benefit is that this trapping scheme does not affect the vacuum pressure.

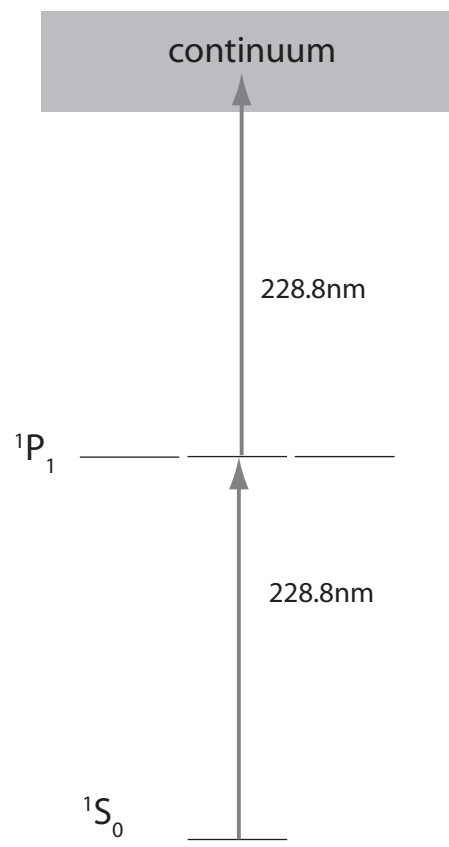


Figure 2.6: Energy level diagram of neutral Cd. A 229 nm photon will excite the atom from the 1S_0 , to the first excited state, 1P_1 , and a second photon of the same color will ionize the Cd.

CHAPTER 3

Cd as a qubit

This chapter will describe the relevant level structure of Cd and explain why Cd is a good choice for trapped ion quantum computing. The initialization and detection procedures will be covered followed by a description of the laser system, the imaging system, and the computer control program.

3.1 Energy levels of Cd-111

Fig 3.1 shows the energy levels for the odd isotopes of Cd⁺. The ground state hyperfine levels, $S_{1/2} |F = 0, m_f = 0\rangle = |0\rangle = |\uparrow\rangle$, $S_{1/2} |F = 1, m_f = 0\rangle = |1\rangle = |\downarrow\rangle$ serve as qubit states. These states make ideal qubits due to the long lifetimes, the magnetic field insensitivity to first order, and the large hyperfine splitting of 14.5 GHz allows for excellent detection efficiency between the two qubit states. The level structure is greatly simplified in Cd due to its spin 1/2 nucleus. This makes operations such as optical pumping very efficient since there are at most three levels involved in the ground state and four involved in the excited state. Qubit manipulation is focused on the $^2S_{1/2} \rightarrow ^2P_{3/2}$ transition, and the absence of a low lying D-state reduces the number of lasers necessary since there is no need for a repumping laser as in other systems such as Ca⁺, Sr⁺, Ba⁺, and Yb⁺.

Cd⁺ has eight stable isotopes, six of which are relatively abundant. Figure 3.2 shows

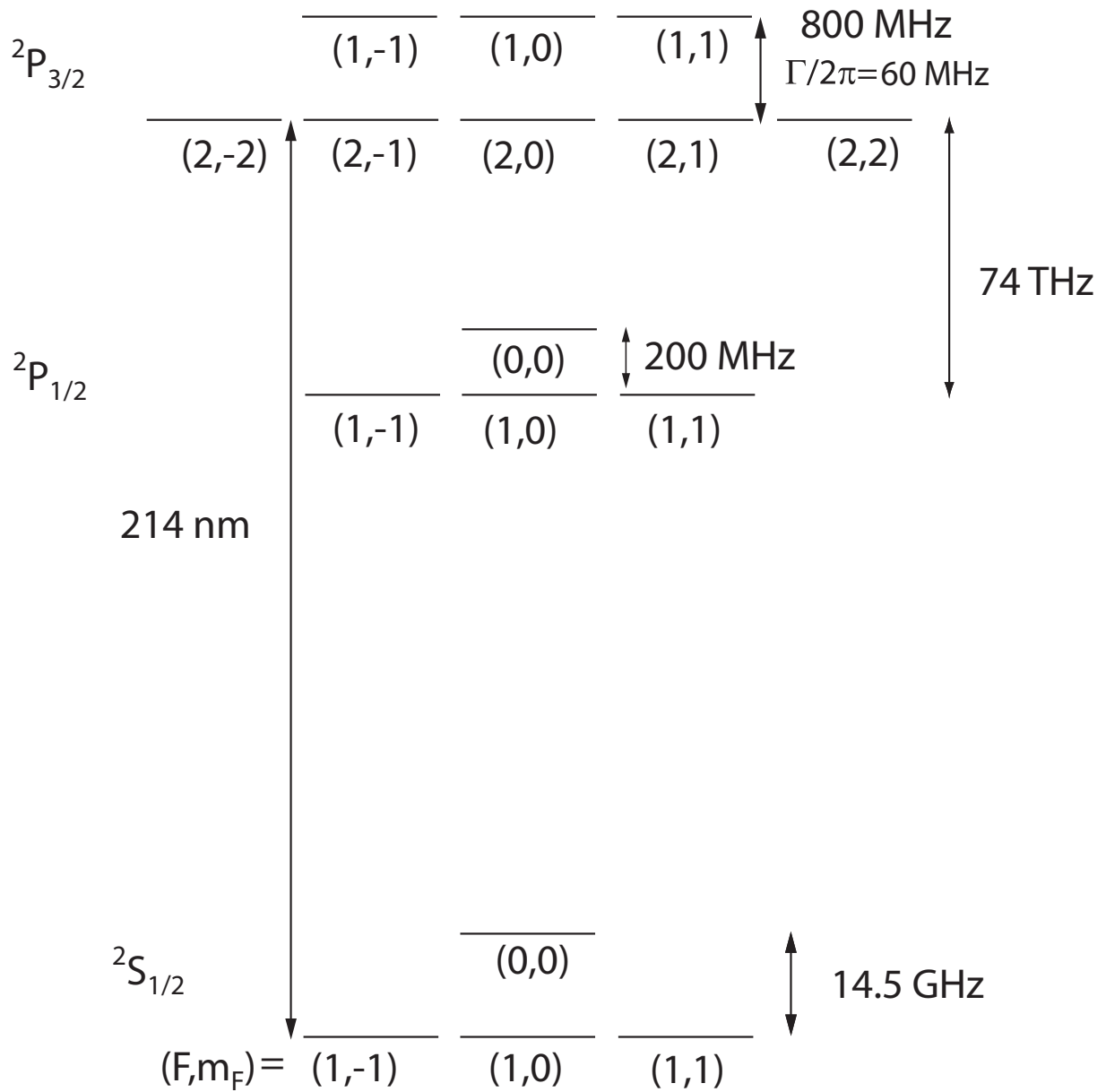


Figure 3.1: Energy level diagram of $^{111}\text{Cd}^+$. The ground state hyperfine levels serve as qubits and are defined as $S_{1/2} |F = 0, m_f = 0\rangle = |0\rangle = |\uparrow\rangle$ and $S_{1/2} |F = 1, m_f = 0\rangle = |1\rangle = |\downarrow\rangle$. The large hyperfine splitting of 14.5 GHz allows for near perfect detection efficiency between the two qubit levels. In addition the large hyperfine splitting of 74 THz allows for a large detuning during certain qubit operations, this large detuning leads to low spontaneous emission rates.

the different isotopes of Cd plotted versus their relative cycling transitions. Only the odd isotopes of Cd, $^{111}\text{Cd}^+$ and $^{113}\text{Cd}^+$, can be used as qubit states since they are the only isotopes with hyperfine structure due to the nonzero nuclear spin, in this work we use $^{111}\text{Cd}^+$ predominantly. However, the even isotopes may be beneficial in the future for sympathetic cooling. In large ion trap arrays, where there are multiple zones for operations such as computation, storage, and shuttling, sympathetic cooling ions may be necessary to quench any extra motion the ions may acquire during transport. The even isotopes would be useful for this purpose since they are well separated in frequency from the odd isotopes, therefore the cooling light for the even isotopes would not have much of an effect on the odd isotopes holding the quantum information.

Two important requirements for quantum computing are the ability to initialize the system and to have a qubit specific measurement capability. Initialization is accomplished with near perfect efficiency by applying π -polarized light tuned to the $^2S_{1/2}|F=1\rangle \rightarrow ^2P_{3/2}|F=1\rangle$ transition, this optically pumps any population in the $^2S_{1/2}|F=1\rangle$ states to the $^2S_{1/2}|F=0\rangle$ state. Measurement, or detection, of the ions is accomplished via σ^+ polarized light resonant with the $^2S_{1/2} \rightarrow ^2P_{3/2}$ transition. Any population in the $|\downarrow\rangle$ qubit state is optically pumped to the $^2P_{3/2}|F=2, m_f=2\rangle$ state where it undergoes a cycling transition. Since this is a resonant process, a great deal of photons are scattered and this state is called the "bright" state. On the other hand, if this same resonant light is applied to the ions when the population is in the $|\uparrow\rangle$ qubit state, very few photons are scattered since the light is now 14.5 GHz off resonance and so this is referred to as the "dark" state. Using this detection scheme we are able to detect the state of a single ion with 99.7% efficiency [15]. Both the initialization and detection schemes are shown in fig.

3.3.

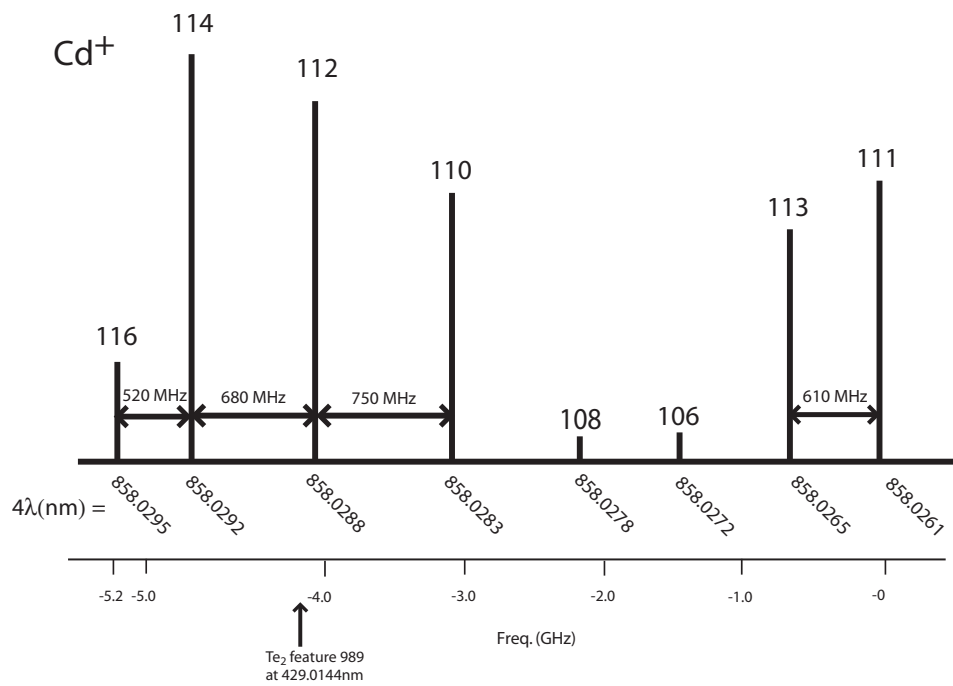


Figure 3.2: The eight stable isotopes of Cd. The isotopes are plotted versus their relative cycling frequency. The wavelengths are given in the IR since the wavemeter used to determine the wavelength only works in the IR. Only $^{111}\text{Cd}^+$ and $^{113}\text{Cd}^+$ can be used as qubit states since they are the only isotopes with non-zero nuclear spin. For the work in this thesis almost all the experiments were done on $^{111}\text{Cd}^+$.

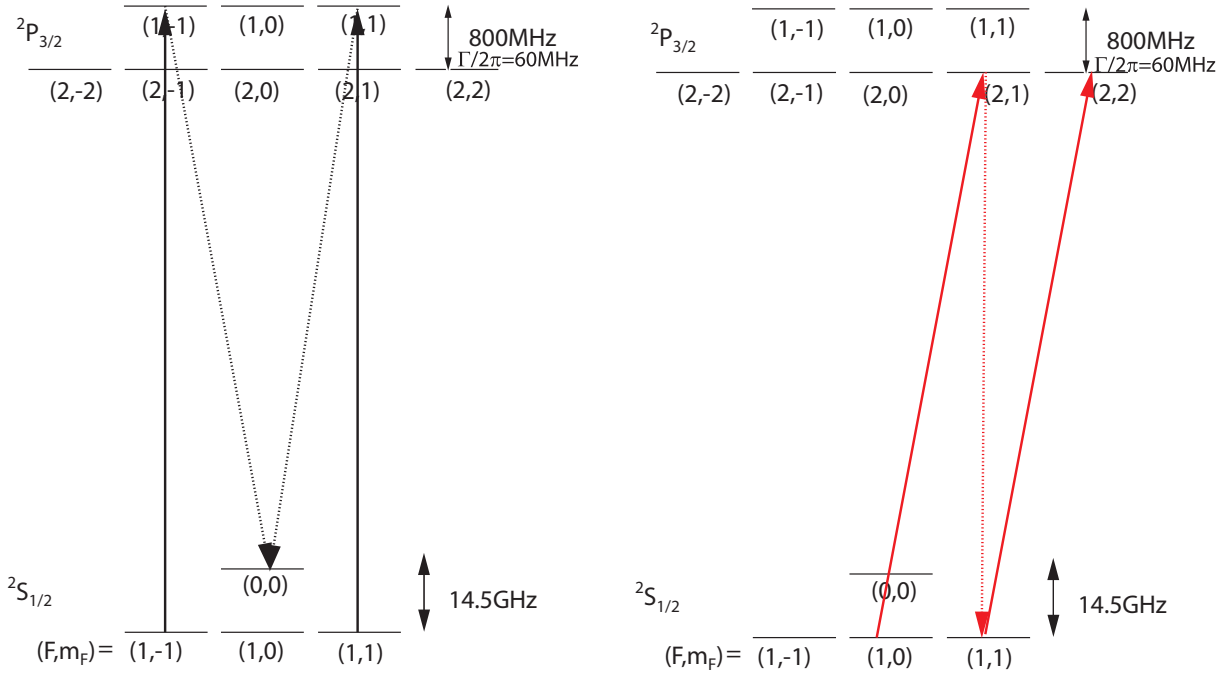


Figure 3.3: Initialization and detection energy level diagrams for Cd. Left: Scheme to initialize the qubits. π -polarized light tuned to the $^2S_{1/2}|F = 1\rangle \rightarrow ^2P_{3/2} |F = 1\rangle$ transition optically pumps any population in the $|F = 1\rangle$ states to the $|\uparrow\rangle$ state. Right: Scheme to detect the ions. When population is in the $|\downarrow\rangle$ qubit state it is optically pumped to the $|1, 1\rangle$ state. From here it undergoes a cycling transition between $^2S_{1/2}|1, 1\rangle \rightarrow ^2P_{3/2}|2, 2\rangle$ and since this is a resonant process a great deal of photons are scattered. However when the population is in the $|\uparrow\rangle$ qubit state the light is no longer resonant and very few photons are scattered.

3.2 Experimental Set-up

3.2.1 The laser system

The experiment uses three primary laser systems, a detection/initialization laser, a Raman transition laser, and a pulsed photoionization laser. As fig. 3.4 shows, the detection laser system is composed of four components starting with a doubled $Nd : VO_4$ laser producing 10.5 W at 532 nm. The next stage is a tunable single mode Ti:Saph laser yielding 2 W at 858.02 nm. This output is doubled twice via two Spectra Physics Wave-train doubling cavities. The first Wavetrain converts 858 nm to 429 nm via a Lithium Triborate (LBO) crystal and has a conversion efficiency of 10%. This blue light is sent to a second doubling cavity using a Beta-Barium Borate (BBO) crystal yielding ~ 4 mW at 214.5 nm.

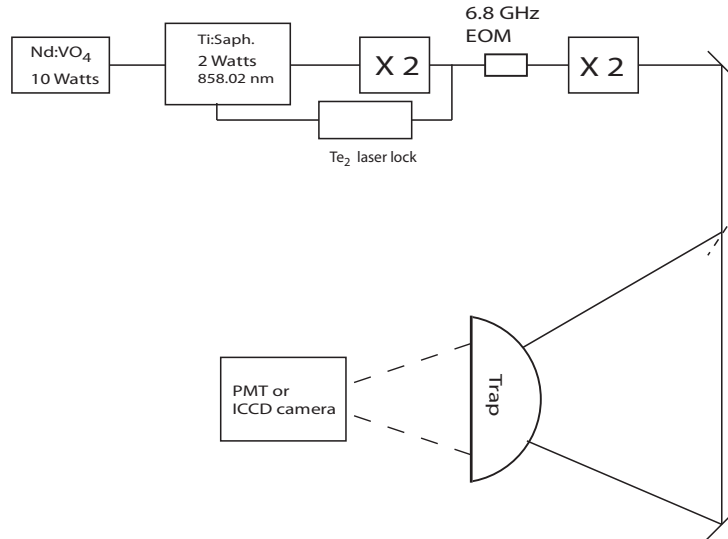


Figure 3.4: Detection laser system. A 10 Watt $Nd : VO_4$ pumps a single mode tunable Ti-Saphairre laser that outputs 2 W at 858 nm. The output of the Ti-Saph is frequency quadrupled via two Wavetrain doubling cavities. The final output is 5 mW at 214 nm.

A small fraction of the blue light from the LBO doubler (~ 10 mW) is split from the main beam line and directed towards a saturated absorption Te_2 vapor cell to stabilize the laser frequency. The basic setup for the Te_2 lock is shown in Fig 3.5. The light is double

passed through a 894MHz AO to bridge the 1.8 GHz frequency difference between the Cd $^2S_{1/2} \rightarrow ^2P_{3/2}$ transition and the nearest tellurium line (after frequency doubling). The double passed beam is broken up into a pump beam, a probe beam, and a reference beam. The Te vapor cell is heated to 500° C to increase optical absorption. The pump and probe beam enter the cell from opposite directions and overlap inside the cell while the reference beam enters the cell next to and in the same direction as the probe beam. When the laser is off resonance the pump and probe beam are absorbed by different velocity groups and the probe and reference beam experience the same optical attenuation. However when the laser frequency is on resonance the stronger pump beam absorbs most of atoms in its path saturating the atomic transition, this results in the probe beam experiencing very little optical attenuation as it traverses the cell. When the laser frequency is on resonance, the reference beam is almost fully attenuated as it passes through the cell. After exiting the cell, the powers of the probe and reference beams are measured on a photodetector and the difference in absorption of the two beams gives a Doppler free lineshape. Before entering the cell the pump beam is sent through an 80 MHz acousto-optic modulator (AOM) modulated at 20 kHz to provide a signal for a lock-in amplifier. From the saturated error signal we derive a dispersive error signal to externally lock the MBR laser.

To generate the detection beam, the light exiting the last doubling stage is sent through a +215 MHz (AOM) yielding a beam resonant with the $^2S_{1/2}|F=1\rangle \rightarrow ^2P_{3/2}|F=2\rangle$ transition. A Doppler cooling beam is also derived from the detection beam by shifting the frequency of the light by +185 MHz instead of +215 MHz. This 185 MHz shift produces a beam that is shifted 30 MHz to the red of the main cycling transition and results in a cooling force on the ions. Doppler cooling will be discussed in more detail in the next chapter. The zeroth order beam is double passed through a second 450 MHz

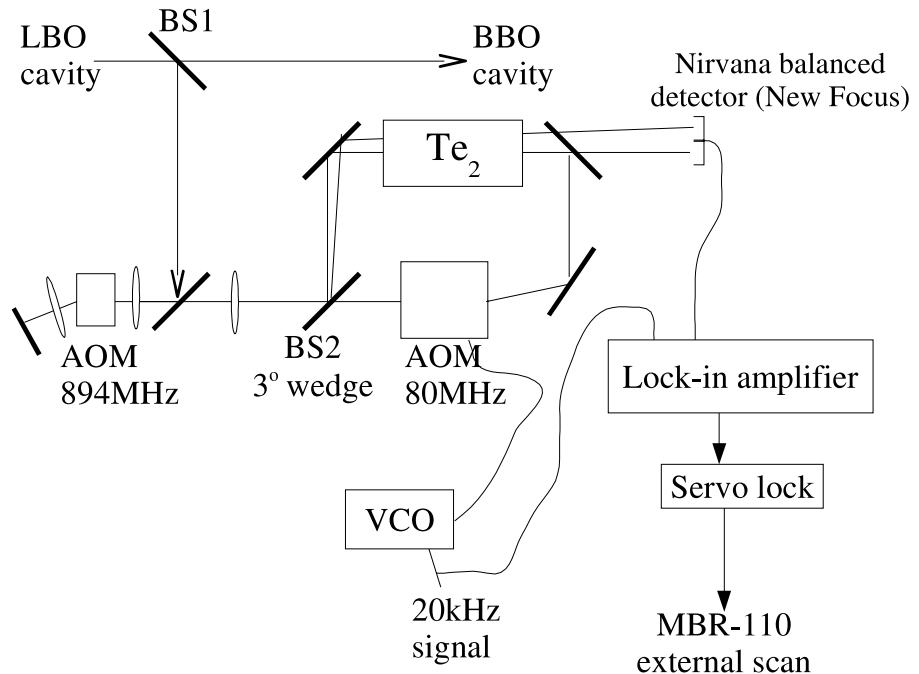


Figure 3.5: Tellurium setup for laser feedback. Approximately 10 mW of blue light is picked off from the main beam line and sent to Te_2 for laser feedback. The light is double passed through a 900 MHz AOM to bridge the frequency difference between the 429 nm light and the nearest Te_2 absorption line. Before entering the cell the laser beam is split into three separate beams, a pump beam, a probe beam, and a reference beam. The pump and probe beam enter and travel through the chamber in opposite directions while the reference beam enters the cell and travels alongside the probe beam. When the laser is on resonance the pump beam saturates the transition and the probe beam passes through the cell mostly unattenuated. However the reference beam is almost fully attenuated. The signals between the probe and reference beam are sent on to a Nirvana photodetector that subtracts the two signals to give a Doppler free lineshape. The output of the detector is sent to a lock-in amplifier to derive an error signal.

AOM, this gives the 900 MHz frequency shift needed to initialize the qubits as can be seen in fig. 3.6.

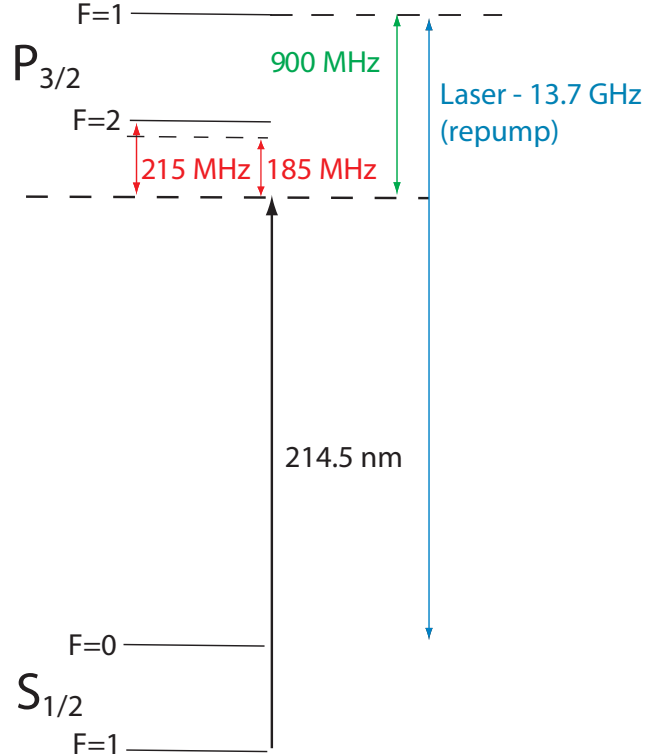


Figure 3.6: AOM frequencies to generate the initialization, detection, and Doppler cooling beams. The output of the last doubling stage is 214.5 nm. The beam is upshifted by 215 MHz to generate the detection beam and the same AOM upshifts the frequency by 185 MHz to Doppler cool the ions. Since the Doppler cooling beam and detection beam are not on simultaneously, sending two frequencies to the same AOM is not a problem. A different AOM upshifts the frequency of the main 214.5 nm beam to generate the initialization beam. And finally an EOM placed in the blue light adds a sideband frequency at 214.5 nm-13.7 GHz to create a repump beam. This stops population from being trapped in the dark state during Doppler cooling.

During Doppler cooling it is possible for population to get trapped in the $|\uparrow\rangle$ qubit state since the Doppler beam does not couple this state to the $^2P_{3/2}|F=1\rangle$ state. When this happens, cooling is no longer possible for that fraction of population. To prevent this, an additional laser frequency is needed to pump population out of the $|\uparrow\rangle$ qubit state and back to the $|\downarrow\rangle$ qubit state. This is accomplished with a 6.8 GHz electro-optic modulator

(EOM) placed in the blue light. Since 13.6 GHz EOM's are not available in the UV, the modulation must occur in the blue light. This adds a frequency comb onto the light and each comb line spaced by 6.8 GHz. The last doubling stage is modified so that both the 429 nm light and the 429 nm + 6.8 GHz sideband are resonant inside the doubling cavity. For the remainder of the thesis the Doppler cooling set-up will refer to both the 185 MHz red detuned detection beam and this additional repumping beam.

Fig. 3.7 shows a second laser system, similar to the detection laser, used to produce the Raman beams. Again we quadruple a single mode tunable Ti-Saph laser to produce UV light, but this Ti-Saph operates at 858.16 nm, which is about 300 GHz detuned from the $^2P_{3/2}$ state in the UV. The Raman beams are used for both single qubit operations and multi-qubit entangling gates, as will be discussed in the next chapter. A schematic diagram for the Raman transitions is shown in figure 3.8. To produce a stimulated Raman transition, which transfers population between the two qubit states, two laser beams detuned from the excited state and having a frequency difference equal to the hyperfine splitting are needed. Instead of using two separate laser systems and phase locking them together, we derive the Raman beams from a single source and use an EOM to produce the frequency difference. A 7.25 GHz EOM is placed in the blue light before the second doubling stage. This adds a frequency comb on to the laser the light and each comb line is separated by 7.25 GHz. The last doubling stage is modified so that the carrier and first sidebands are resonant inside the doubling cavity. This provides a frequency comb in the UV such that any two comb lines spaced in frequency by 14.5 GHz can drive the Raman transition. Upon exiting the last doubling stage the laser beam is split into two paths to form a Mach-Zehnder (M-Z) interferometer. This interferometer is necessary in order for the ions to see a beatnote between the two beams [16]. To form the M-Z, the laser beam exiting the final doubling stage is sent through a 212 MHz AOM and the first order

diffracted beam is picked off to form one arm of the interferometer. The zeroth order beam is sent to a second variable AOM operating around 212 MHz to form the second arm of the M-Z interferometer. This second AOM can be scanned to create any of the necessary Raman transitions. This second beam line also contains retro-reflecting mirror which is composed of two 90° degree mirrors mounted on a translation stage, this allows the path length between the two arms to be adjusted.

To photoionize neutral Cd atoms inside the iontrap we built a femtosecond pulsed laser system operating at 915 nm with a repetition rate of 86 MHz and pulse bandwidth of about 10 nm, as shown in fig. 3.9. The output of the pulsed laser is doubled twice yielding an average power about 10 mW at 229 nm. We estimate that this light is capable of photoionizing nearly all the atoms that traverse the laser beam, which results in highly efficient loading [17].

3.2.2 Imaging System

The ion fluorescence is collected and either imaged onto an intensified charge coupled device (ICCD) camera or sent a photomultiplier tube (PMT) to measure photon counts. The ion fluorescence is collected with a microscope objective f/2.1 lens placed about 11 mm from the front chamber window. A 400 μm aperture is placed at the focus of this lens to cut down on any scattered light that does not come directly from the ion. A second lens images the ion onto either the ICCD camera or the PMT. A flipper mirror just before the camera allows the light to be sent to either detector.

3.2.3 Computer Control

The entire experiment is managed via a Labview program controlling a National Instruments 6534 pulser PCI card. The PCI card outputs a 32 bit TTL signal, each bit controls an rf switch that is connected to an AOM or EOM in the experiment. Some of

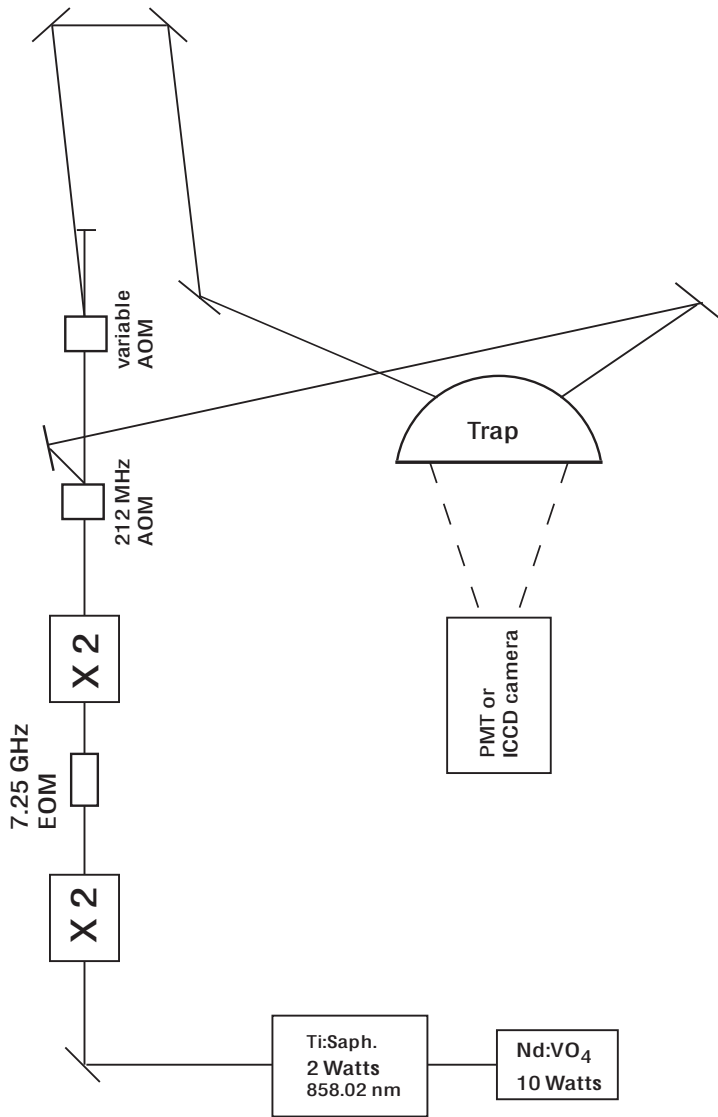


Figure 3.7: Raman laser system. A Nd:VO₄ pumps a single mode tunable Ti-Saph laser outputting 2 W at 858 nm. The IR light is frequency quadrupled to produce about 4 mW of UV output. An EOM is placed between the two doubling stages to add a frequency comb onto the laser. Each time in the combline is spaced by 7.25 GHz and the doubler is modified so that the carrier and sidebands are resonant with the doubling cavity. The light out of the UV doubler is split into two to form a M-Z interferometer. When the two arms combine at the ion, each pair of frequency comb lines spaced by 14.5 GHz can drive a stimulated Raman transition.

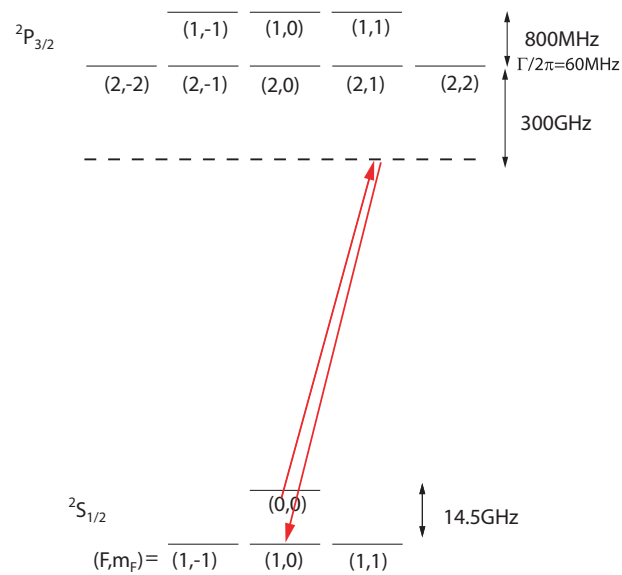


Figure 3.8: Energy level diagram for the Raman transitions. Two laser beams detuned from the excited state and with a frequency difference of 14.5 GHz drive the stimulated Raman transitions. These transitions can create any arbitrary superposition of the qubit states.

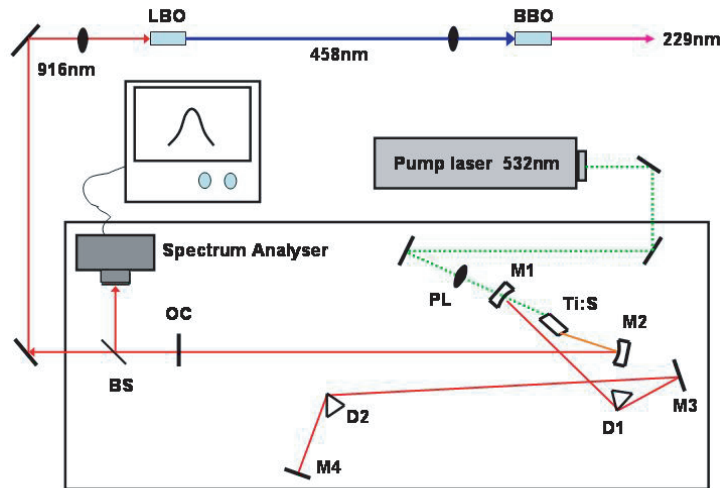


Figure 3.9: Schematic diagram of the pulsed laser system. A homemade Ti-Sapphire pulsed laser was fabricated to generate the 229 nm photoionization beam.

these rf switches act as multiplexors to send two rf signals to a single AOM at different times. An example of this is the detection/Doppler cooling AOM that requires two different frequencies. The Labview program itself has many different chapters, each chapter controls a different part of the experiment. A typical experiment consists of the following pulse sequence as shown in fig. 3.10: 1. Doppler cooling (~ 1 ms), 2. optical pumping to initialize the system ($\sim 5 \mu\text{s}$), 3. a pulse sequence tailored to a specific experiment, and 4. a detection pulse ($\sim 200 \mu\text{s}$). During detection photons are collected by either the camera or PMT and sent to a National Instruments 6602 counter card. This card is gated by the pulser card so that it only counts photons during the detection phase of the experiment. The photon counts from each gate pulse are stored in a buffer and downloaded after a specified amount of time set by the user. This is to improve the duty cycle of the experiment since downloading the count rate can take up to several milliseconds. The collected data is first turned into a histogram and then other parameters, such as the average number of photons, can be extracted from the data and shown on a graph in the Labview program.

For many experiments the collected histograms are split into two distributions, one for the bright state and one for the dark state. This allows a discriminator to be set and gives better detection efficiency between the two states. As can be seen in Fig. 3.11, setting a discriminator value at 1 or 2 counts separates the dark state from the bright state almost completely.

In the case of two ions these detection histograms become more complicated since there are four possible states to detect: both ions bright, both ions dark, and one bright ion and one dark ion. In order to have good discrimination for two ions, the double bright state must have a high enough count rate to make a noticeable divide between the double bright state and the bright/dark+dark/bright states, as shown in figure 3.12. For a single

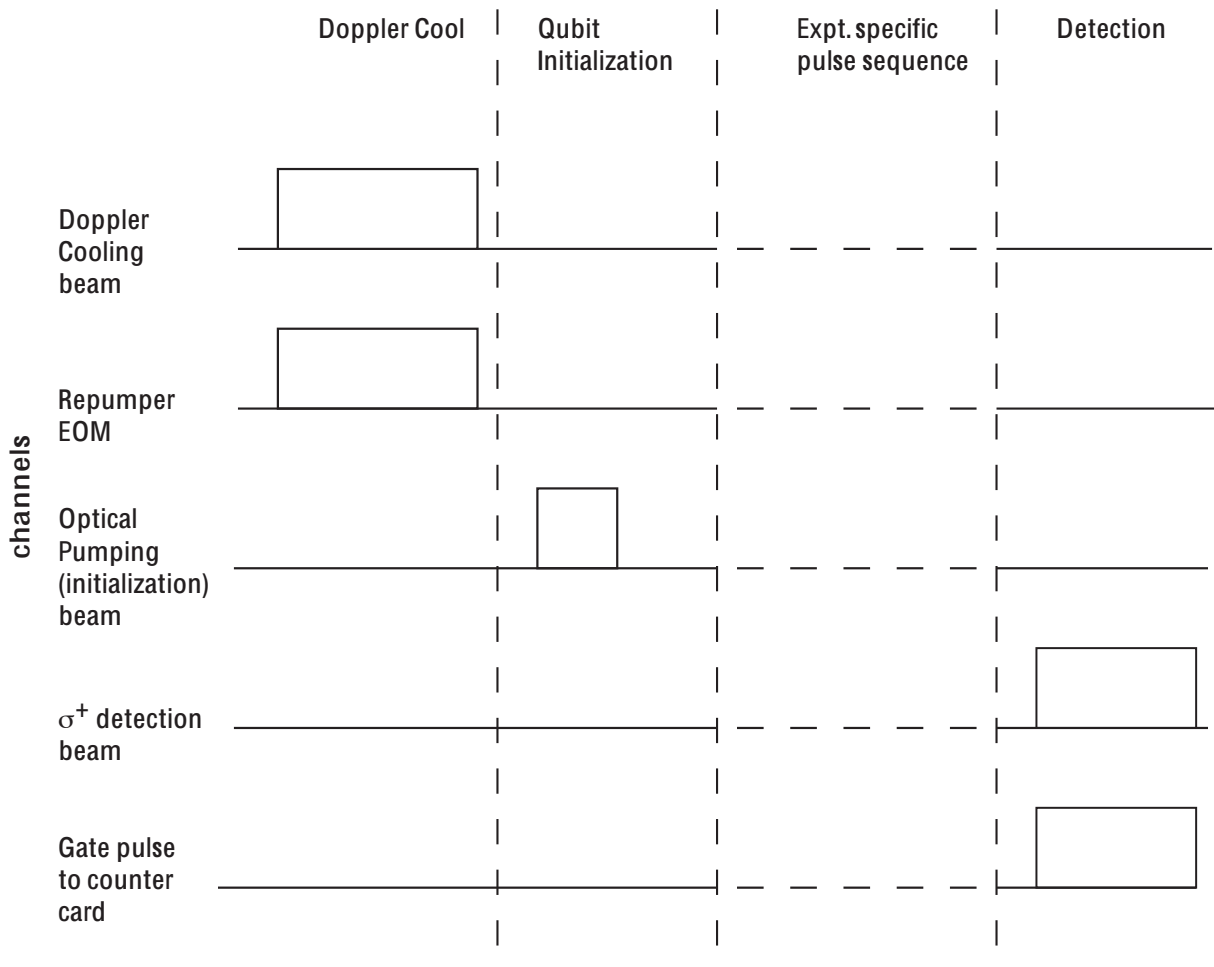


Figure 3.10: Typical experimental pulse sequence. First the ions are Doppler cooled for ~ 1 ms and then the ions are initialized to the $|\uparrow\rangle$ state, this takes about 5 μ s. The next pulse is tailored to a specific experiment such as Raman sideband cooling. For the final step the detection light is applied for ~ 200 μ s.

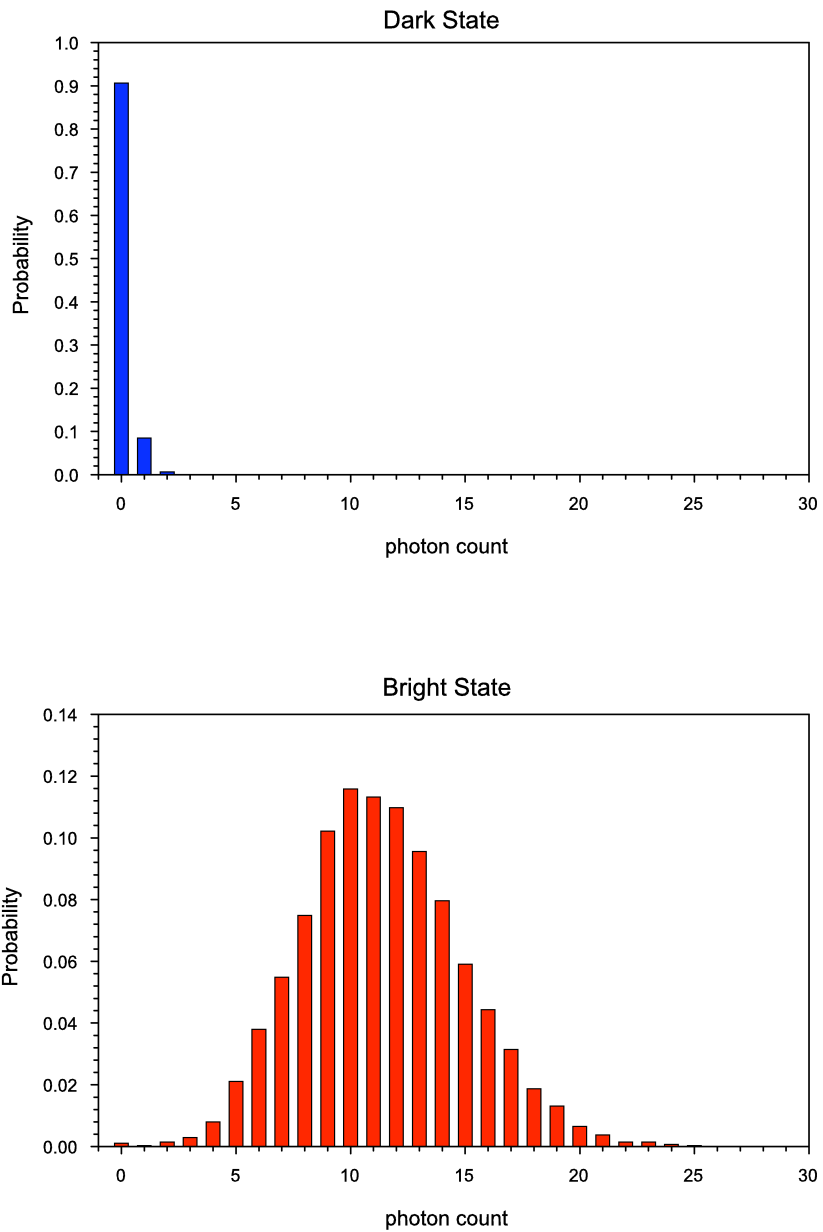


Figure 3.11: Detection histograms for a single ion. With a discriminator, separating the two distributions for counts greater than 1 or 2, yields a detection fidelity of 99.7% for a single ion.

ion the detection efficiency can be as high as 99% between the bright and dark state, but for two ions this efficiency drops to 97%.

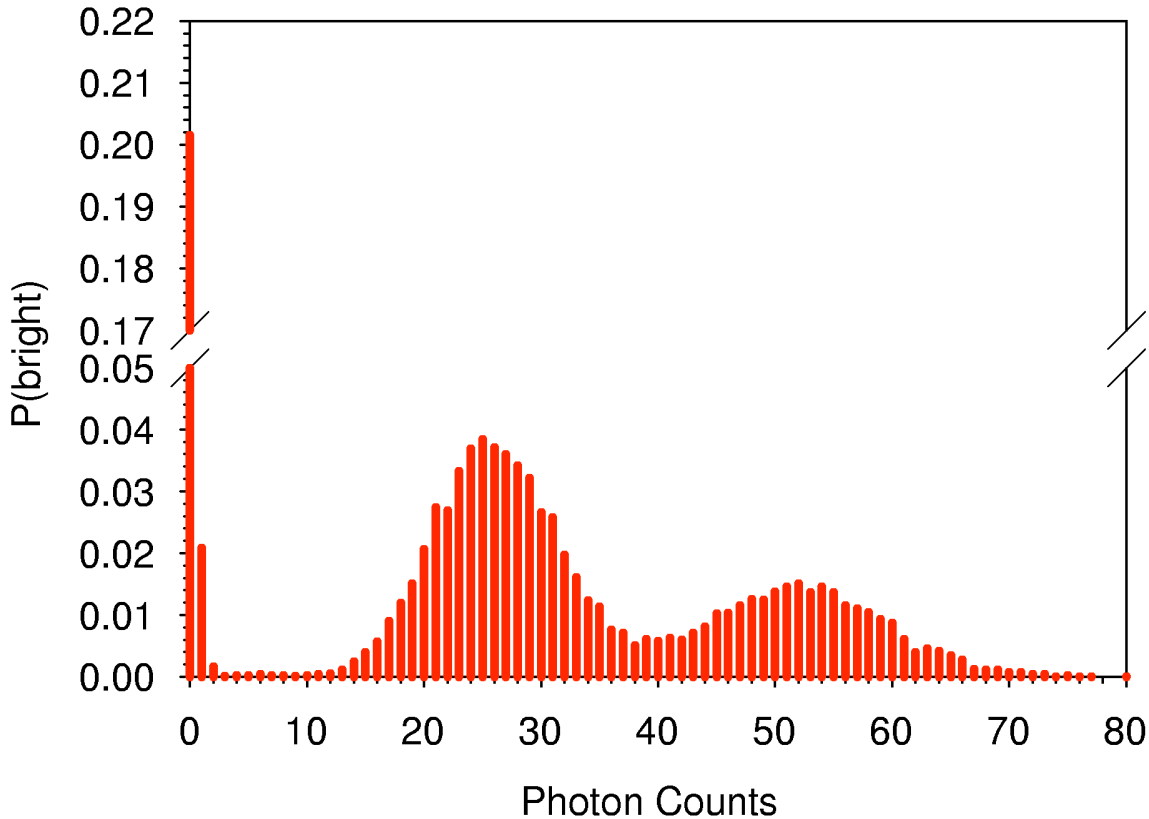


Figure 3.12: Detection histograms for two ions. Detecting two ions is more complicated than a single ion since there can be a great deal of overlap between the double bright ion distribution and the single bright ion distribution. To prevent this the count rate from double bright state is set high enough to minimize the overlap between the two outcomes. For two ions the greatest detection fidelity possible is 97%.

CHAPTER 4

Coherent single qubit operations

An important requirement for quantum computing is the need for a universal set of gates that includes both single qubit gates and multi-qubit entangling gates. In classical computing, single bit operations comprise of gates such as a NOT-gate, which creates a bit flip as shown in table 4.1. The quantum computing counterparts to these gates are single qubit rotations, these rotations allow us to take advantage of the quantum mechanical principle of superposition by allowing a rotation into any arbitrary state $\alpha|\uparrow\rangle + \beta|\downarrow\rangle$. This allows us to store more information because N bits we can store 2^N states. The second type of gate is a multi-bit gate. A classical example of this gate is an AND gate, whose truth table is shown in table 4.1. In quantum computing, two qubit gates such as the controlled-NOT (CNOT) gate, also shown in table 4.1, allow us to turn superposition states into entangled states. Applying a CNOT gate to the state $(|\uparrow\rangle + |\downarrow\rangle)_{q1}(|\downarrow\rangle)_{q2}$ gives the entangled state $(|\uparrow\rangle_{q1}|\downarrow\rangle_{q2}) + (|\downarrow\rangle_{q1}|\uparrow\rangle_{q2})$, where q1 and q2 represent the state of qubit 1 and 2, respectively. This state is entangled since mathematically it cannot be written as a product of two states. Together the multi-qubit entangling gates and single qubit gates comprise a universal set of gates, this is a necessary component for a universal quantum computer [9].

This chapter will describe in detail how the single qubit gates are implemented and

	classical	quantum	
single bit operations	NOT gate $\uparrow \rightarrow \downarrow$ $\downarrow \rightarrow \uparrow$	single qubit rotation $ \uparrow\rangle \rightarrow \cos(\frac{\theta}{2}) \uparrow\rangle + e^{i\phi}\sin(\frac{\theta}{2}) \downarrow\rangle$ $ \downarrow\rangle \rightarrow \cos(\frac{\theta}{2}) \downarrow\rangle - e^{-i\phi}\sin(\frac{\theta}{2}) \uparrow\rangle$	
	2 bit AND gate $\uparrow\uparrow \rightarrow \uparrow$ $\uparrow\downarrow \rightarrow \uparrow$ $\downarrow\uparrow \rightarrow \uparrow$ $\downarrow\downarrow \rightarrow \downarrow$	2 qubit controlled-NOT (CNOT) $ \uparrow\uparrow\rangle \rightarrow \uparrow\uparrow\rangle$ $ \uparrow\downarrow\rangle \rightarrow \uparrow\downarrow\rangle$ $ \downarrow\uparrow\rangle \rightarrow \downarrow\downarrow\rangle$ $ \downarrow\downarrow\rangle \rightarrow \downarrow\uparrow\rangle$	
2 bit operations			

Table 4.1: Truth table for both single and multi-bit classical and quantum gates.

describe the tools needed to form the multi-qubit gates that will be discussed in the following chapter.

4.1 Single Qubit Operations

The trapped ion system can be thought of as a spin-1/2 magnetic moment in a constant magnetic field [18]. This two-level system is a valid approximation since the applied light strongly couples the two qubit levels and only weakly couples to off-resonant states. As mentioned before, the qubit states are the ground state hyperfine levels of the odd Cd⁺ isotopes, we define these states as

$$\begin{aligned} |0\rangle &= |\uparrow\rangle = |S_{1/2}, F = 0, m_F = 0\rangle = \begin{pmatrix} 1 \\ 0 \end{pmatrix} \\ |1\rangle &= |\downarrow\rangle = |S_{1/2}, F = 1, m_F = 0\rangle = \begin{pmatrix} 0 \\ 1 \end{pmatrix} \end{aligned} \quad (4.1)$$

where both the bra-ket and matrix notation are shown.

For this system, we can write the Hamiltonian as

$$H_0 = \frac{\hbar\omega_0}{2}\hat{\sigma}_z + \hbar\omega_x\hat{a}^\dagger\hat{a}. \quad (4.2)$$

Here $\hat{\sigma}_z = \begin{pmatrix} 1 & 0 \\ 0 & -1 \end{pmatrix}$ is the Pauli spin operator matrix, $\hbar\omega_0$ is the natural energy splitting between the two qubit states, \hat{a} and \hat{a}^\dagger are the raising and lowering (creation and annihilation) operators, ω_x is the frequency of motion along the x-axis, and we can represent the state of the system by

$$|\Psi(t)\rangle = \sum_{n=1}^{\infty} (a_{\uparrow,n}(t)|\uparrow\rangle + a_{\downarrow,n}(t)|\downarrow\rangle)|n\rangle. \quad (4.3)$$

When an external electromagnetic field is applied, the Hamiltonian becomes $H_T = H_0 + H'$, where the perturbed Hamiltonian H' is given by

$$H' = -\mu_b \cdot \mathbf{B}(r, t). \quad (4.4)$$

Here μ_b is the effective magnetic dipole moment of the two-level system and $B(r, t) = B_x \cos(\mathbf{k}\mathbf{r} - \omega t + \phi)\mathbf{x}$ is the applied effective magnetic field. In the experiment the coupling mechanism does not need to be a magnetic dipole interaction, but it must yield a Hamiltonian of the form

$$H' = \frac{\hbar\Omega}{2} (\sigma_+ e^{i(\mathbf{k}\mathbf{r} - \omega t + \phi)} + \sigma_- e^{-i(\mathbf{k}\mathbf{r} - \omega t + \phi)}), \quad (4.5)$$

where $\Omega = \frac{-\mu_b B_x}{2\hbar}$ is the Rabi frequency, $\sigma_+ = \begin{pmatrix} 0 & 1 \\ 0 & 0 \end{pmatrix}$, and $\sigma_- = \begin{pmatrix} 0 & 0 \\ 1 & 0 \end{pmatrix}$.

For simplicity, we will assume a scenario where the magnetic field propagates such that $\mathbf{k} \cdot \mathbf{z}_t = 0$, that is the magnetic field propagation is perpendicular to the direction of the harmonic potential. Since the photons have no momentum in the z-direction, they cannot couple to the harmonic oscillator levels in this interaction. Later in the chapter we will discuss the more general case when $\mathbf{k} \cdot \mathbf{z}_t \neq 0$, but for the present case it is not

necessary. Under this assumption the factor $e^{ik \cdot r}$ will contribute at most a phase factor of e^{ikr_0} , which can be absorbed into the phase ϕ .

We can express the Hamiltonian in the interaction picture by applying the transformation $H_{int} = U_0^\dagger H' U_0$, where $U_0 = e^{-\frac{iH_0 t}{\hbar}}$ is the time evolution operator for the unperturbed system with Hamiltonian H_0 . Applying this transformation and making the RWA yields:

$$H_I = \frac{\hbar\Omega}{2}(\sigma_+ e^{-i(\delta\omega t + \phi)} + \sigma_- e^{i(\delta\omega t + \phi)}) \quad (4.6)$$

where $\delta\omega = \omega - \omega_0$ is the field detuning from resonance. The solution to the Rabi two-level problem is [19]:

$$\begin{aligned} \dot{c}_{\uparrow,n} &= \frac{i\Omega}{2}e^{-i((\delta\omega)t + \phi)}c_{\downarrow,n} \\ \dot{c}_{\downarrow,n} &= \frac{-\Omega}{2}e^{i((\delta\omega)t + \phi)}c_{\uparrow,n} \end{aligned} \quad (4.7)$$

where $c_{m,n}(t)$ are the amplitudes of the corresponding levels $|m\rangle|n\rangle$ for the qubit state in the rotating frame

$$|\Psi(t)\rangle = \sum_{n=1}^{\infty} (c_{\uparrow,n}(t)e^{-i\omega_0 t/2}|\uparrow\rangle + c_{\downarrow,n}(t)e^{i\omega_0 t/2}|\downarrow\rangle)e^{in\omega_x t}|n\rangle. \quad (4.8)$$

When $\delta\omega = 0$ the field is on resonance and the state evolves under the time-evolution operator $U(t)$ by $|\Psi(t)\rangle = \hat{U}(t)|\Psi(0)\rangle$, here $\hat{U}(t)$ is defined as (in the $c_{\uparrow,n}, c_{\downarrow,n}$ basis),

$$\hat{U}(t) = \begin{pmatrix} \cos(\frac{\Omega t}{2}) & -ie^{-i\phi}\sin(\frac{\Omega t}{2}) \\ -ie^{i\phi}\sin(\frac{\Omega t}{2}) & \cos(\frac{\Omega t}{2}) \end{pmatrix} = R(\Omega t, \phi). \quad (4.9)$$

This matrix, $R(\Omega t, \phi)$, is a rotation on the Bloch sphere by $\theta = \Omega t$ about a torque vector pointing along the equatorial plane given by $\cos(\varphi)\mathbf{x} + \sin(\varphi)\mathbf{y}$, as shown in figure

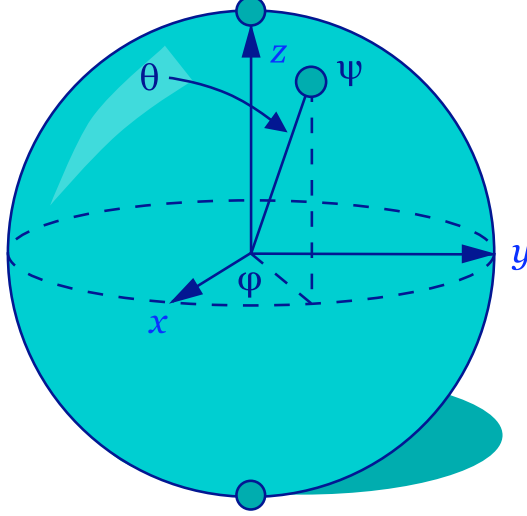


Figure 4.1: Representation of the Bloch sphere. The positive z-direction represents the $| \uparrow \rangle$ state and the negative z-direction represents the $| \downarrow \rangle$ state. Rotations by $R(\theta, \varphi)$ show how the qubit state evolves under single qubit rotations. Rotations are made about the torque vector pointing in the x-y plane and z-rotations are formed through composite pulse sequences in x and y.

4.1. We define the following rotations using Eq. 4.9: $R_x(\theta) = R(\theta, 0)$ is a rotation about the x-axis and $R_y(\theta) = R(\theta, \pi/2)$ is a rotation about the y-axis. For a universal quantum computer we need to be able to make rotations in all three directions, x, y, and z, but Eq. 4.9 only allows us to make rotations in x and y. To make a z-rotation we use a composite pulse sequence consisting of x and y rotations through the following: $R_z(\theta) = R_x(\pi/2)R_y(\theta)R_x(-\pi/2)$. This is equivalent to applying a phase shift of θ to the ions.

Since we have control over both Ωt and ϕ , Eq. 4.9 allows us to make rotations giving any superposition of $| \uparrow \rangle$ and $| \downarrow \rangle$ that we need, therefore fulfilling the requirement for the single qubit rotations.

4.2 Accessing the motional levels

Recall in the last section that we restricted the magnetic field propagation direction to simplify the calculations since, for single qubit rotations, it is not necessary to couple to

the motional harmonic oscillator levels. However, in order to make multi-ion gates we will need to access these motional modes since they act as a quantum databus for the system. For this purpose, we will consider a more general case for the interaction Hamiltonian where $\mathbf{k} \cdot \mathbf{z}_t \neq 0$ and we are able to couple to the motional modes of the ion crystal.

In this case, the position operator $\hat{\mathbf{z}}_t = z_0(\hat{a} + \hat{a}^\dagger)\vec{z}_t$ (here \vec{z} is a unit vector in the z-direction) couples to the harmonic oscillator levels giving the interaction Hamiltonian

$$H_I = \frac{\hbar\Omega}{2}(\sigma_+ e^{i\eta(\hat{a}e^{-i\omega_x t} + \hat{a}^\dagger e^{i\omega_x t})} e^{-(\delta\omega t - \phi)} + h.c.). \quad (4.10)$$

Here $\eta = k_z z_0$ is the Lamb-Dicke parameter, $k_z = \mathbf{k} \cdot \vec{z}_t$ is the component of the wavevector in the z_t direction, and $z_0 = \sqrt{\hbar/2m\omega_x}$ is the position spread of the ion's wavepacket in the ground state. If we are in the resolved sideband limit, when $\Omega \ll \omega_x$, then the individual motional levels can be addressed. To access the motional levels we tune the laser frequency such that $\delta\omega = (n - n')\omega_x + \omega_0$, and this allows us to bridge the energy spacing between the vibrational levels. By doing this we can couple the states $|\uparrow\rangle|n\rangle \rightarrow |\downarrow\rangle|n'\rangle$, where n and n' are different motional levels. The coefficients of these coupled levels evolve as

$$\begin{aligned} \dot{c}_{\uparrow,n'} &= -\frac{\Omega_{n,n+\Delta n}}{2} e^{-i(\delta t + \phi)} c_{\downarrow,n}, \\ \dot{c}_{\downarrow,n} &= -\frac{\Omega_{n,n+\Delta n}}{2} e^{i(\delta t + \phi)} c_{\uparrow,n'}, \end{aligned} \quad (4.11)$$

where $\Omega_{n,n+\Delta n}$ is the generalized Rabi frequency given by $\Omega D(n,n')$. Here the Debye-Waller factor, $D_{n',n}$, factor is defined as

$$\begin{aligned}
D_{n,n'} &= |\langle n | e^{i\eta(a+a^\dagger)} | n \rangle| \\
&= e^{-\eta/2} \left(\frac{n_{<}!}{n_{>}!} \right)^{1/2} \eta^{|n'-n|} L_{n_{<}}^{|n-n'|}(\eta^2).
\end{aligned} \tag{4.12}$$

Here $n_<(n_>)$ is the lesser (greater) of n' and n and L_n^α is the generalized Laguerre polynomial [11].

For most trapped ion experiments, the ions must be in the Lamb-Dicke limit (LDL). This means that the extent of the ions wavepacket is much smaller than the wavelength of the exciting light, that is $\sqrt{\langle k_z^2 \hat{z}_t^2 \rangle} \ll 1$. If the ions are not in the LDL, then different parts of the wavepacket feel different phases of the applied light and rotate at different rates. This can result in incoherent operations. In most experiments we are concerned with three main transitions: the carrier ($n'=n$), the first red sideband ($n'=n+1$), and the first blue sideband ($n'=n-1$). Under the LDL, $\eta^2 n \ll 1$, the corresponding Debye-Waller factor for each transition is: $D_{n,n}=1$ for the carrier transition, $D_{n,n-1}=\eta\sqrt{n}$ for the first blue sideband, and $D_{n,n+1}=\eta\sqrt{n+1}$ for the first red sideband. The Debeye-Waller factor scales like η^k for the k^{th} sideband and the sideband strength goes to zero as η goes to zero.

4.3 Microwave Transitions

In practice the single qubit rotations are achieved with either resonant microwaves or with optical Raman transitions. Resonant microwaves at 14.5 GHz can drive a complete spin flip, $|\uparrow\rangle$ to $|\downarrow\rangle$, or create an arbitrary superposition, $\alpha|\uparrow\rangle + \beta|\downarrow\rangle$, of the qubit levels. Microwaves are generated by broadcasting an amplified microwave source through a horn into the ion trap. The horn propagation direction is positioned perpendicular to the quantization axis resulting in the microwave polarization lying parallel to the quantization

axis. With this setup the Lamb-Dicke parameter is $\eta = 5 \times 10^{-6}$, this means that the sidebands are a factor of 10^{-6} weaker than the carrier transition and makes using microwaves to drive the motional transitions inefficient.

From Eq. 4.9 we can see that the population oscillates in time between the $|\uparrow\rangle$ and $|\downarrow\rangle$ states, this is called as Rabi flopping. Fig. 4.2 shows microwave Rabi flopping for both the clock state qubits, $|\uparrow\rangle \rightarrow |\downarrow\rangle$, and the Zeeman transition, $|\uparrow\rangle \rightarrow |F=1, m_F=1\rangle$, for a power of $P=1\text{ W}$ sent to the horn. In the lower plot a magnetic field of $B=3.75\text{ G}$ is applied to the ion giving a 5.25 MHz splitting of the Zeeman levels. This plot clearly shows how sensitive the Zeeman levels are to magnetic field fluctuations compared to the clock state qubits. This is not surprising since the sensitivity of the clock states to magnetic field noise is $\delta\nu_{clock} = \frac{600}{G^2} Hz B \delta B$ whereas the Zeeman levels sensitivity is $\delta\nu_{clock} = \frac{1.4}{G} MHz \delta B$. At a magnetic field of 3.25 G, the Zeeman levels are about 620 times more sensitive to magnetic field fluctuations than the clock states. The clock state Rabi flopping rate is roughly twice as fast as the Rabi flopping rate of the Zeeman levels due to microwave polarization effects.

4.4 Stimulated Raman Transitions

A second way to drive single qubit rotations is to use optical Raman transitions. These transitions are also useful because they allow access to the motional states and it is through the motional states, that we are able to cool and entangle the ions, as will be discussed later.

A Raman transition is a stimulated two photon transition involving three levels, here the levels involved are the two qubit states $|\uparrow\rangle$ and $|\downarrow\rangle$ and the excited ${}^2P_{3/2}$ state, $|e\rangle$. Two laser beams detuned from the excited state by Δ and with frequency splitting equal to the frequency difference between the two qubit levels, $\omega_0 = 14.5\text{ GHz}$ for Cd, can drive

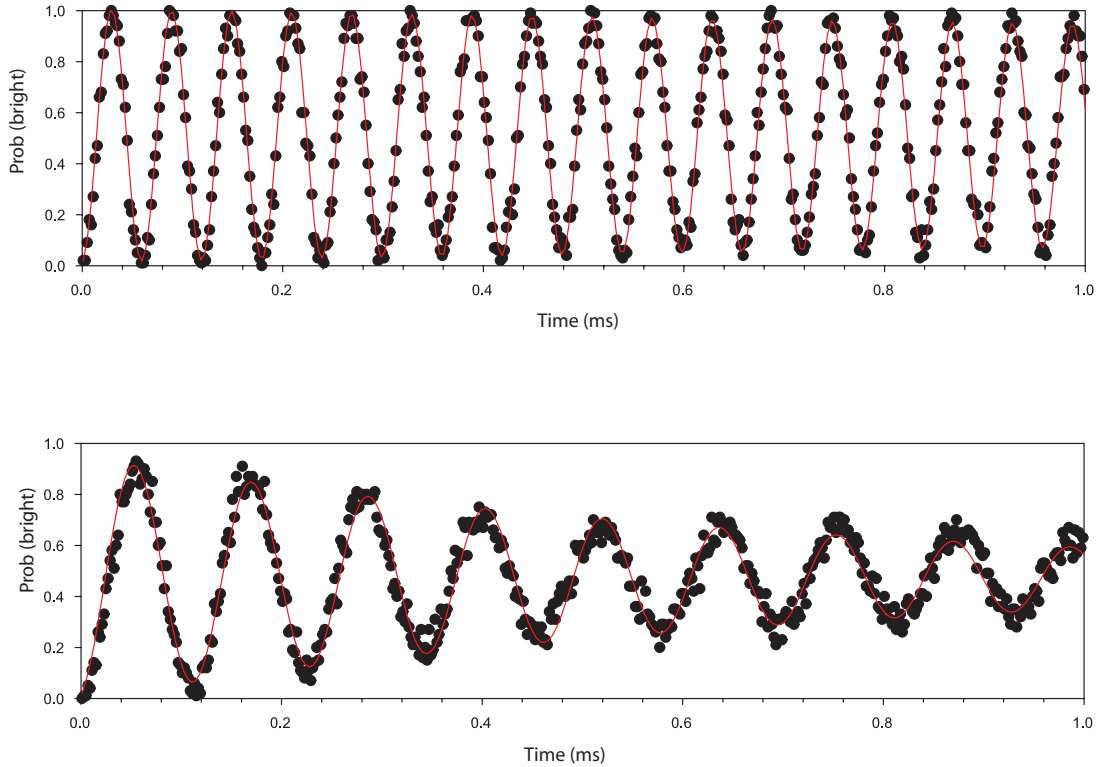


Figure 4.2: Microwave Rabi flopping for the carrier and Zeeman transition. The top plot shows Rabi flopping for the clock state carrier transition, $|\uparrow\rangle \rightarrow |\downarrow\rangle$, while the bottom plot shows Rabi flopping for the Zeeman transition, $|\uparrow\rangle \rightarrow |F = 1, m_F = 1\rangle$, with 1 W of power applied to the microwave horn for both plots. The carrier transition oscillates at about twice the frequency of the Zeeman level due to polarization of the microwaves. Clearly the Zeeman levels are more sensitive to magnetic field fluctuations than the carrier.

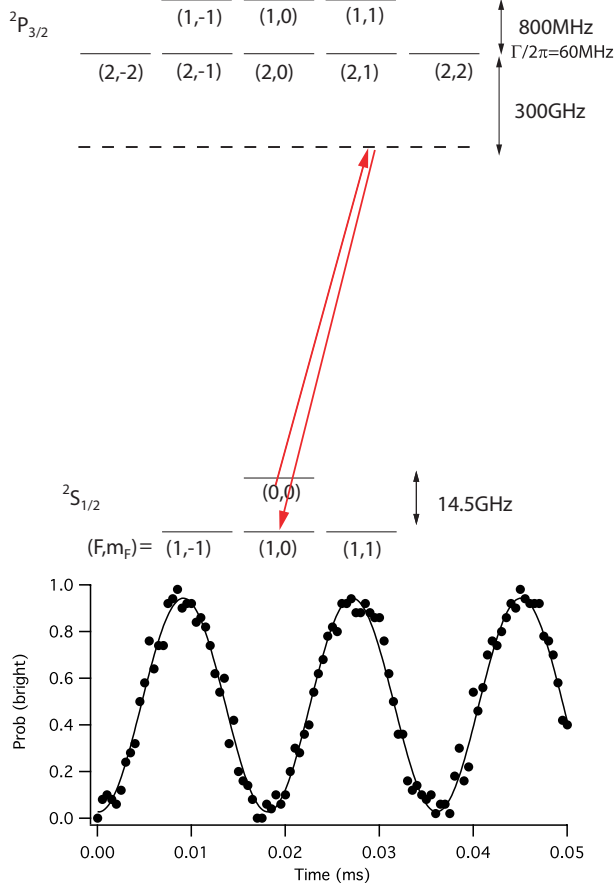


Figure 4.3: Top: Energy level diagram for the Raman transitions. Two laser beams detuned from the excited state and with a frequency difference of 14.5 GHz drive the stimulated Raman transitions. These transitions can create any arbitrary superposition of the qubit states. Bottom: Stimulated Rabi flopping for a detuning of $\Delta = 2\pi \times 150$ GHz, with $\Omega = 2\pi \times 55$ kHz.

transitions between the spin states, as shown in Fig. 4.3. We represent the field from each laser beam by $\mathbf{E}_q(r) = \hat{E}_q(\mathbf{r}) \cos(\mathbf{k}_q \cdot \mathbf{r} - \omega_q t - \phi_q) \epsilon_q$, where $q = a, b$ are the two different electric fields. Each field is connected to the excited state through an electric dipole operator, $\mu_{\uparrow,\downarrow}$.

Just as before, we can transform the dipole interaction $H = -\mu \cdot \mathbf{E}$ into a rotating frame about ω_a and, using the RWA, the interaction Hamiltonian is

$$H_I = \frac{\hbar g_{\uparrow,a}}{2} (e^{i\mathbf{k}_a \cdot \hat{\mathbf{r}} + i\phi} |e\rangle \langle \uparrow| + h.c.) + \frac{\hbar g_{\downarrow,b}}{2} (e^{i\mathbf{k}_b \cdot \hat{\mathbf{r}} + i\phi} e^{-i(\omega_0 - \delta\omega)t} |e\rangle \langle \downarrow| + h.c.) + \frac{\hbar\Delta}{2} |e\rangle \langle e|. \quad (4.13)$$

Here $\hbar g_{s,l} = -\mu_m \cdot \epsilon E_l(\hat{r})/2$ is the dipole coupling strength from the laser field ($l=[a,b]$) between the qubit spin state ($s=[|\uparrow\rangle, |\downarrow\rangle]$) and the excited state $|e\rangle$.

When the detuning is much larger than both the natural linewidth and the coupling strengths, $\Delta \gg \gamma, |g_{s,l}|$, the spontaneous emission is negligible and the state $|e\rangle$ can be adiabatically eliminated [20]. Applying the RWA again, this time on the microwave frequencies, gives

$$H_I = \frac{\hbar\Omega}{2}(e^{i(\Delta\mathbf{k}\cdot\hat{\mathbf{r}}-(\delta\omega)t+\Delta\phi)}|\uparrow\rangle\langle\downarrow| + h.c.) + \frac{\hbar\chi_\uparrow}{2}|\uparrow\rangle\langle\uparrow| + \frac{\hbar\chi_\downarrow}{2}|\downarrow\rangle\langle\downarrow| \quad (4.14)$$

where $\Delta\mathbf{k} = k_b - k_a$ and $\Delta\phi = \phi_b - \phi_a$ are the differences in the wavevectors and phases of the applied fields, $\Omega = g_{\uparrow,a}g_{\downarrow,b}^*/2\Delta$ is the base Rabi frequency between the two qubit states, and $\chi_m = (|g_{m,a}|^2 + |g_{m,b}|^2)/2\Delta$ is the shift on qubit level $|m\rangle$ by both optical fields. Rewriting this in terms of spin operators gives

$$\hat{H}_I = \frac{\hbar\Omega}{2}(\sigma_+ e^{i(\Delta k\cdot\hat{r}-(\delta\omega)t+\Delta\phi)} + \sigma_- e^{-i(\Delta k\cdot\hat{r}-(\delta\omega)t+\Delta\phi)}) + \frac{\hbar\chi_-}{2}\hat{\sigma}_z, \quad (4.15)$$

where $\chi_- = \chi_\uparrow - \chi_\downarrow/2$ is the difference in the light shift on both qubit levels. The common lightshift, $(\chi_\uparrow - \chi_\downarrow)/2$, does not adversely affect the qubit levels and so can be taken out of the Hamiltonian. Writing this in terms of the interaction picture of the vibrational levels gives

$$\hat{H}_I = \frac{\hbar\Omega}{2}(\sigma_+ e^{i\eta(\hat{a}e^{-i\omega t} + \hat{a}^\dagger e^{i\omega t})} e^{-i(\delta\omega)t} e^{i(\Delta kr_0 + \Delta\phi)} + h.c.) + \frac{\hbar\chi_-}{2}\hat{\sigma}_z. \quad (4.16)$$

This equation is similar to Eq. 4.10 but now ϕ has become $\Delta\phi$, $\eta = \Delta k_z z_0$, and there is an extra term due to the light shift.

The extra term in Eq. 4.16 is called the AC stark shift, this displaces the qubit energy levels by an amount $\hbar\chi$ proportional to the intensity of the applied fields. Fig. 4.4 shows

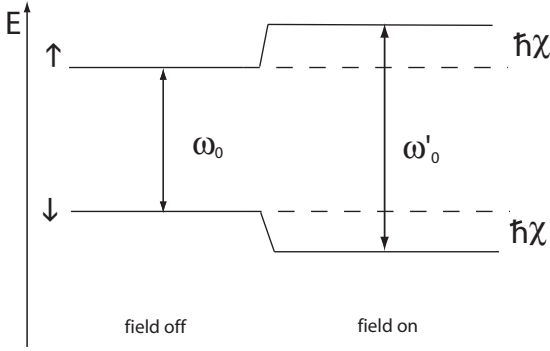


Figure 4.4: Effect of AC Stark shift on qubit levels. When the Raman beams are turned on, each qubit level is shifted by an amount $\hbar\chi$.

that, as a result of this light shift, the coupling frequency for the qubit levels changes during the stimulated Raman transitions. To see how the qubit states evolve under this Stark shift we must transform into the rotating frame, $e^{i\omega'_0 \hat{\sigma}_z t/2} H e^{i\omega'_0 \hat{\sigma}_z t/2}$, and this gives the following interaction Hamiltonian,

$$\hat{H}_I = \frac{\hbar\Omega}{2} (\hat{\sigma}_+ e^{i\eta(\hat{a}e^{-i\omega t} + \hat{a}^\dagger e^{i\omega t})} e^{-i(\delta\omega')t} e^{i(\Delta kr_0 + \Delta\phi)} + h.c.). \quad (4.17)$$

Here $\delta\omega' = \omega_b - \omega_a - \omega'_0$ is the detuning from the Stark shifted resonance, and $\omega'_0 = \omega_0 + \chi_-$ when the fields a and b are turned on. This equation has the same form as Eq. 4.16 except the detuning is replaced by the Stark shifted detuning. The states evolve as

$$|\Psi(t)\rangle = \sum_{n=0}^{\infty} (\tilde{c}_{\uparrow,n}(t) e^{i\omega'_0 t/2} |\uparrow\rangle + \tilde{c}_{\downarrow,n}(t) e^{-i\omega'_0 t/2} |1\rangle) e^{i\omega_x t} |n\rangle \quad (4.18)$$

With these beams we can either drive a pure spin flip transition or we can access the motional modes and drive transitions such as $|\uparrow\rangle|n\rangle \rightarrow |\downarrow\rangle|n'\rangle$, we do this by controlling the frequency splitting between the applied beams. A beatnote of 14.5 GHz allows us to transfer population between the two qubit states and a beatnote of $\omega_0 \pm \omega_\nu$ allows us access to the motional modes, where ω_ν is the trap frequency. Fig. 4.5 depicts the laser

beam frequencies needed to drive the motional transitions.

4.5 Implementing Stimulated Raman Transitions

To give the maximum Rabi frequency for the motional levels we need to make Δk as large as possible. Since the chamber geometry does not allow the beams to enter at a 180° angle, the best we can do is send the beams into the chamber at 45° to each other, as shown in Fig. 4.6. In addition this 90° geometry results in sensitivity in only the transverse direction and therefore simplifies the experiments because we only need to be concerned with motion along one axis instead of three.

Because we want the stimulated Raman transitions to couple only the two qubit states, there are some restrictions on the light driving the transitions. Since the Raman transition couples to the excited P state through a dipole interaction and since both qubit states must couple to the same excited state, we must drive the transition to the $|P_{3/2}, F = 1, m_F = \pm 1\rangle$ state because, as Fig. 4.7 shows, this is the only level that couples to both qubit states. The second constraint stems from the fact that the two Raman beams enter the chamber with fields pointing parallel/perpendicular to the quantization axis. To maximize the Rabi frequency under this condition we must use linearly polarized light. And the last restriction comes from the transition probabilities between the involved states. The $|P_{3/2}, F = 1, m_F = 1\rangle$ transition has a ' π '-phase shift relative to the $|P_{3/2}, F = 1, m_F = -1\rangle$ transition and so, the polarizations of the light must be 90° out of phase with each other to ensure that the two transition paths do not destructively interfere.

One source of decoherence during the stimulated Raman transitions is spontaneous emission from off-resonant coupling while the laser beams are turned on. The amount of spontaneous emission depends on both the intensity of the light and the amount of

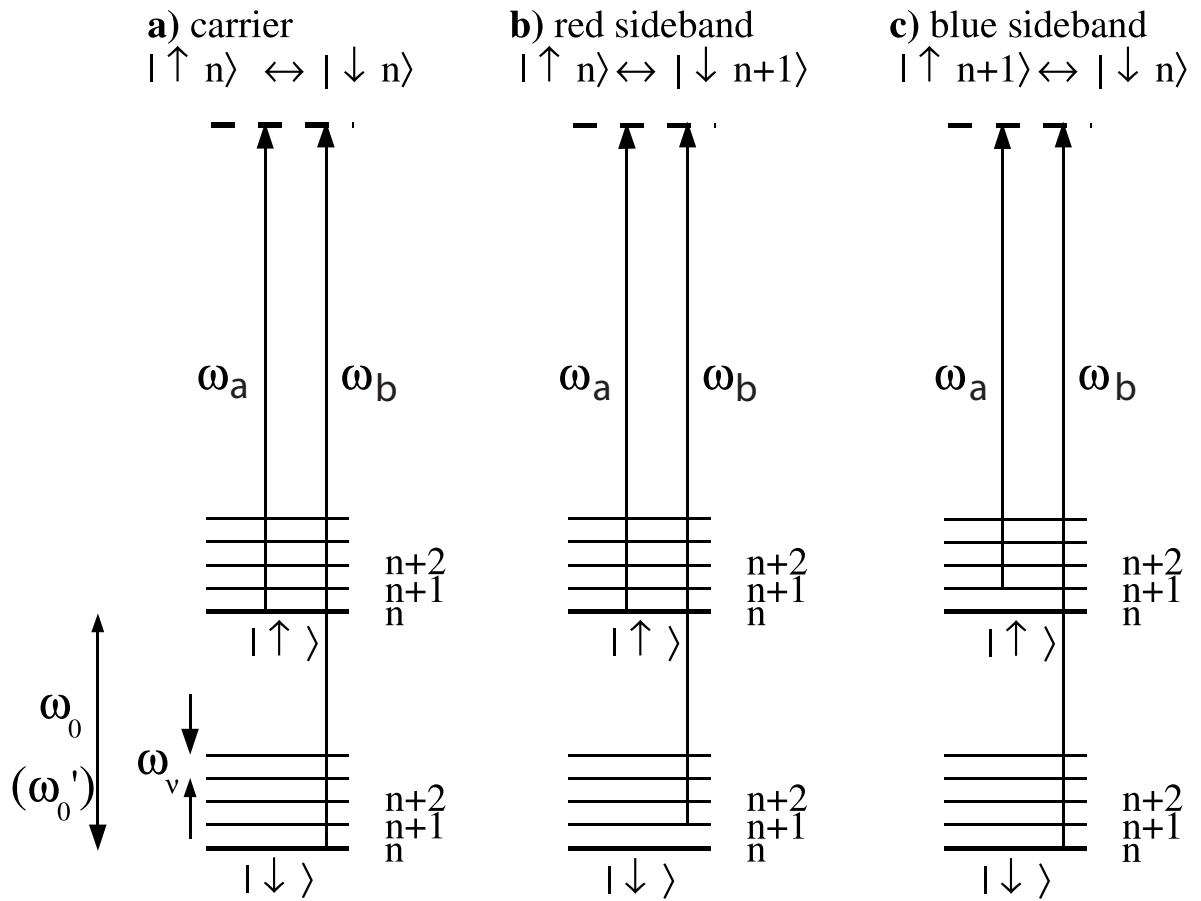


Figure 4.5: Energy level diagram for a motional stimulated Raman transition. The beatnote, $\omega_b - \omega_a$, determines which transition is driven. Here the difference frequency is a.) ω'_0 for the carrier transition, b.) $\omega'_0 - \omega_\nu$ for the redsideband, and c.) $\omega'_0 - \omega_\nu$ for the bluesideband.

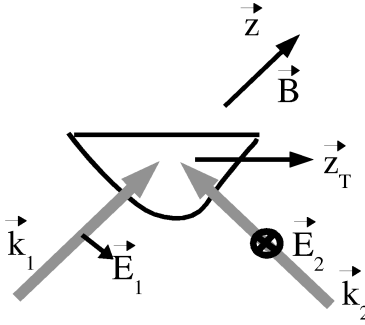


Figure 4.6: Raman beams going into the chamber. Since optical access does not allow the Raman beams to enter at a 180° angle from each other, we send them into the chamber at 45° . This allows access to the motional levels of the ions. Coupling and polarization restrictions require that both beams' polarizations be rotated by 90° from each other.

detuning from the excited state. The best way to understand how spontaneous emission effects the experiments is to compare the spontaneous emission rate for large detunings, $\gamma_p = s\gamma^3/(4\Delta^2)$, to the Raman transition rate, $\Omega = s\gamma^2/\Delta$, where $s=I/I_{sat}$ is the saturation parameter. Doing this, we get $\gamma_p/\Omega = \gamma/(2\Delta)$, which means that in the time it takes the ion to undergo a complete spin flip, the qubit has a $\gamma/(2\Delta)$ chance of undergoing a spontaneous emission event and therefore decaying to the ground state incoherently. As can be seen from the above equation, the spontaneous emission rate scales as $1/\Delta$ and so the larger the detuning, the smaller the spontaneous emission rate. But this condition only holds if the detuning is much less than the fine structure splitting and coupling to other excited states is negligible [21].

4.6 Creating the Raman beams with an EOM

As mentioned in chapter 2, we generate the Raman beams by using an EOM operating at 7.25 GHz at 429 nm. This EOM adds a frequency comb onto the laser light and the last doubling stage is modified so that all the comb lines are resonant with the cavity.

$^{111}\text{Cd}^+$ $P_{1/2} \leftrightarrow P_{3/2}$ transition 214.5nm

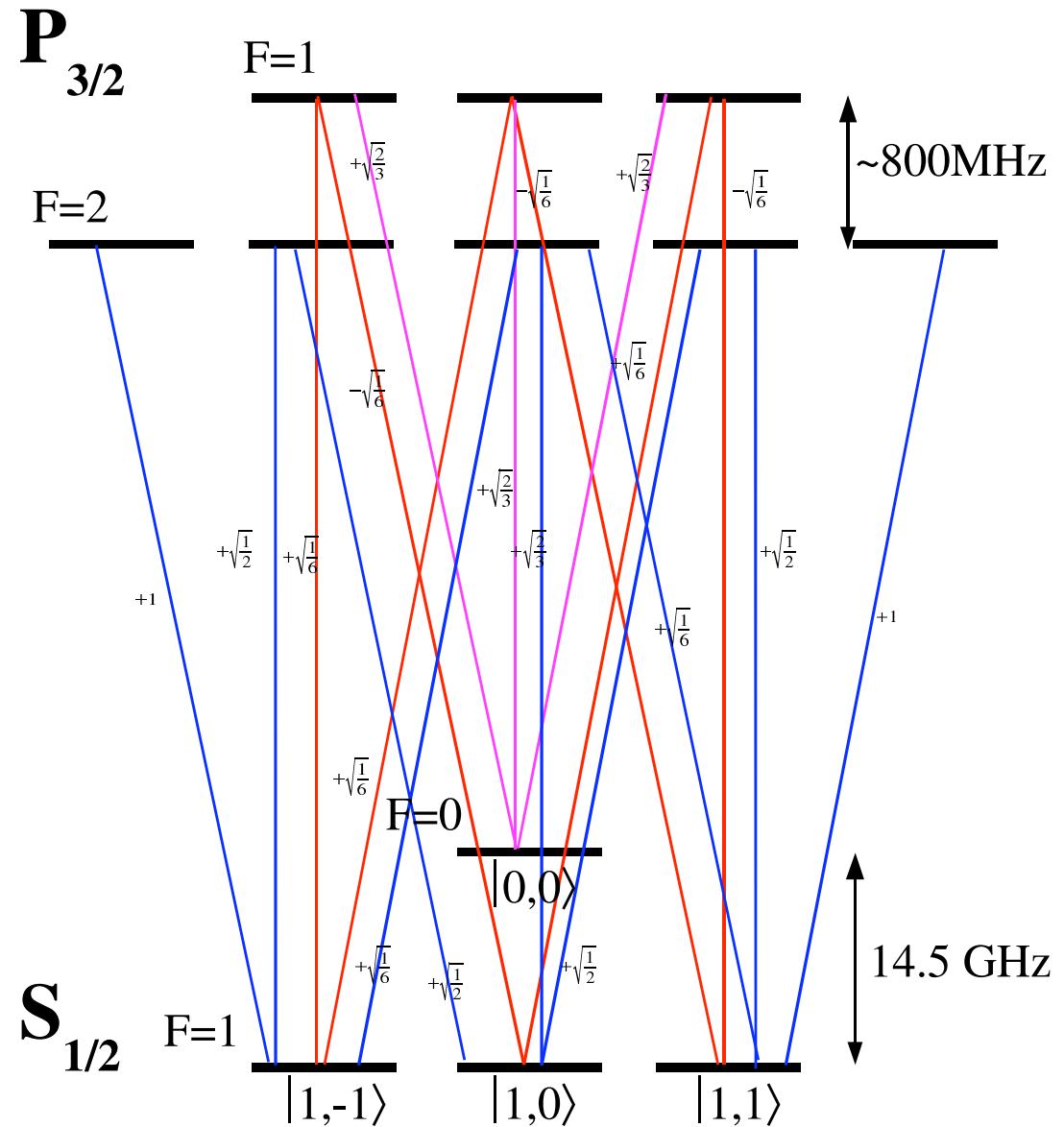


Figure 4.7: Electric dipole transition probabilities from the $S_{1/2} \rightarrow P_{3/2}$ manifolds. The only states that couple to both of the qubit levels are the $|P_{3/2}, F = 1 m_F = \pm 1\rangle$.

This EOM spectrum, when combined with the M-Z interferometer, yields a field at the ion [16]

$$E_{UV} = \alpha \frac{E_0^2}{4} e^{2i(kx - \omega t)} \sum_{n=-\infty}^{\infty} J_n(2\phi) e^{in((\delta k)x - \omega'_0 t/2)} [1 + e^{i(2k+n\delta k)\Delta x}] + c.c., \quad (4.19)$$

where α is a conversion efficiency factor, E_0 is the electric field amplitude of the EOM laser input, $J_n(\phi)$ is an n^{th} order Bessel function with modulation index ϕ , and δk is the wavevector difference between two adjacent sidebands with frequency splitting $\omega'_0/2$.

This field results in a Rabi frequency of

$$\Omega = 2\Omega_0 e^{i(\delta k)(2x + \Delta x)} \sum_{n=-\infty}^{\infty} J_n(2\phi) J_{n-2}(2\phi) \cos[(2k + (n-1)\delta k)\Delta x], \quad (4.20)$$

with $\delta k \cdot \Delta x = (2m+1)\pi$, where m is an integer. For this set up the Rabi frequency can be as high as $0.48\Omega_0$ with a modulation frequency of 0.764. The 0.48 prefactor is a consequence of the M-Z set-up. The problem with Eq. 4.20 is that the $k\Delta x$ factor inside the cosine term requires optical stability of the M-Z interferometer, this can be difficult since the path length of each arm is about 1 meter. To overcome this problem we introduce a frequency shift between the two arms of the M-Z such that $\Delta\omega \gg \Omega$. To keep the frequency beatnotes resonant with the qubit, the shift is compensated by changing the modulation frequency of the EOM by $\pm\Delta\omega/2$. The resulting Rabi frequency is

$$\Omega = \Omega_0 e^{i\beta} \sum_{n=-\infty}^{\infty} J_n(2\phi) J_{n-2}(2\phi) e^{in(\delta k)\Delta x} = \Omega_0 e^{i\beta} J_2(4\phi \sin(\delta k \Delta x)/2) \quad (4.21)$$

where $e^{i\beta} = e^{-i(k+2\delta k)\Delta x}$. For this case the maximum Rabi frequency is $0.244\Omega_0$ for a modulation index of 0.764.

Instead of scanning the EOM in our experiment to reach the desired Raman transitions, we scan one of the AOM's in the M-Z. If we scan the EOM, the sidebands move out of

resonance with the doubling cavity. But by scanning the AOM's, we are able to keep the blue light on resonance with the BBO cavity and still able to reach all the Raman transitions needed for the different experiments. Fig. 4.8 shows a plot of the Raman spectrum derived from scanning one of the AOM's in the M-Z, while leaving the other AOM at a fixed frequency. Each arm of the M-Z results in a spectral comb line and the plot shows the Raman structure of the carrier and sidebands for each comb set.

4.7 Ground State Cooling

As the next chapter will show, we use the collective motion of the ions as a quantum databus and so we must have good control over this motion. The first step to any computation is to cool the ions to near the ground state of motion. We do this by first applying the Doppler cooling beam which takes the ions to an $\bar{n} \sim 10$, where \bar{n} is the average vibrational mode of the motional population. To cool the ions further we apply a sequence of pulses consisting of a blue sideband, to lower the population by $\Delta\bar{n} = 1$ quanta on average, followed by a recycling pulse consisting of a spontaneous Raman transition as shown in Fig. 4.9. The spontaneous Raman transition does not change the vibrational level of the ions on average but only re-initializes the system. This pulse sequence is repeated many times and when the ion reaches the ground state, further cooling pulses have no effect since the blue sideband transition is no longer possible.

To measure the ions' ‘temperature’, we use the intensity of the first red and blue sideband as a gauge. First we prepare the ion in the $|\uparrow\rangle$ state and then apply the cooling pulse sequence described above. Detecting the ions gives:

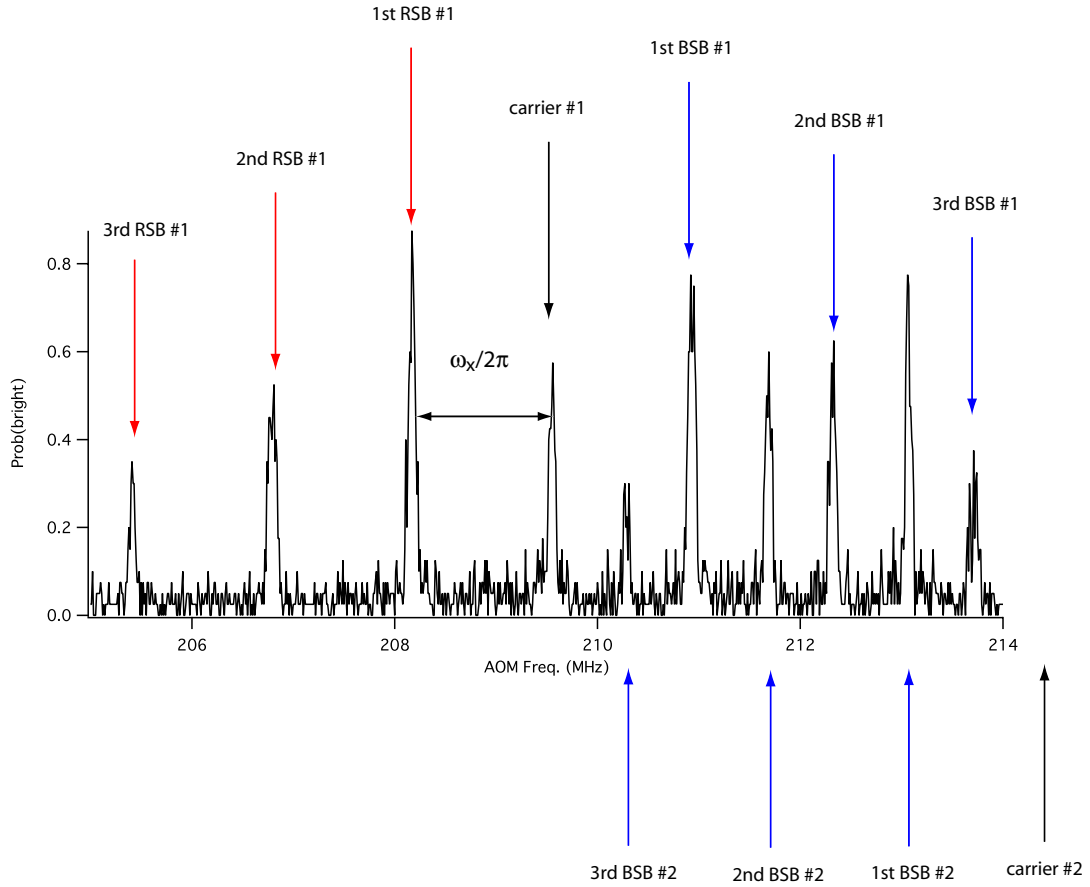


Figure 4.8: AO scan showing the frequency spectrum of the Raman transitions. There are two sets of comb lines, one from each arm of the M-Z.

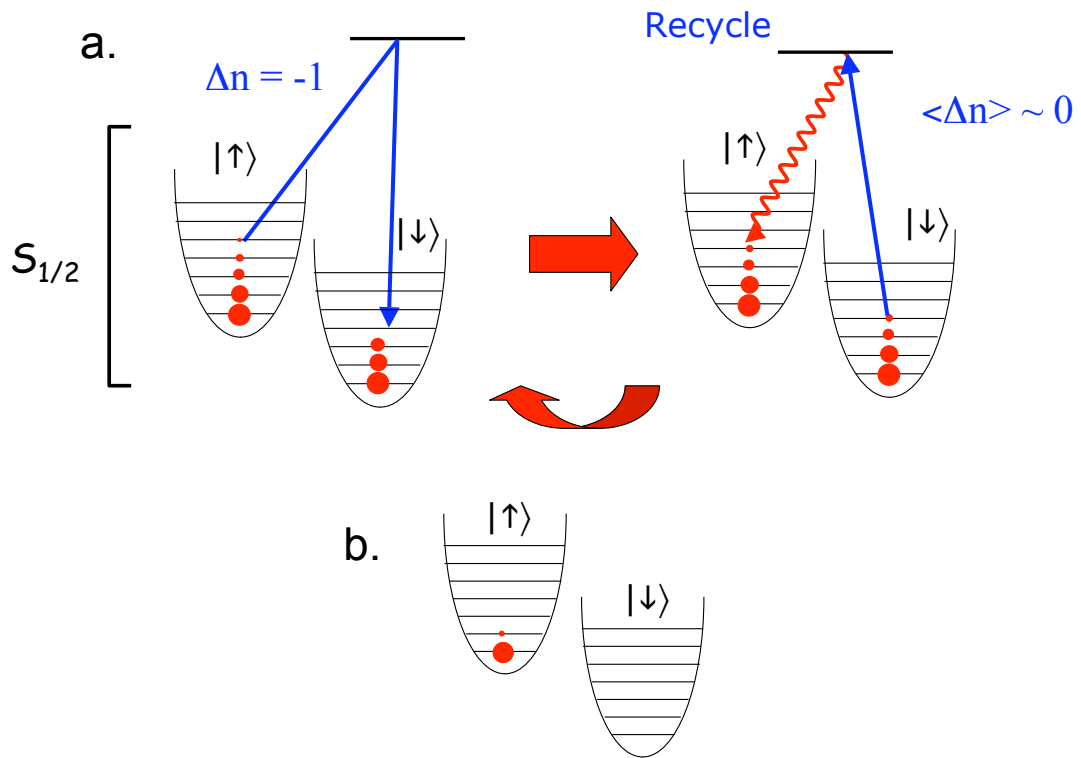


Figure 4.9: Raman cooling scheme. a. The ion is prepared in the $|\uparrow\rangle$ state and then we apply a blue sideband. This reduces the average vibrational state. This pulse is followed by a spontaneous Raman pulse to return the population back to the $|\uparrow\rangle$ state. Repeating this process many times produces an ion with most of its population in $n = 0$ ground state, as shown in b.

$$P_{rsb}(|1\rangle) = \sum_{n=0}^{\infty} P_n \sin^2(\Omega_{n,n-1} t/2) \quad (4.22)$$

$$P_{bsb}(|1\rangle) = \sum_{n=0}^{\infty} P_n \sin^2(\Omega_{n,n+1} t/2) = \sum_{n=0}^{\text{inf}} P_{n+1} \sin^2(\Omega_{n,n-1} t/2) \quad (4.23)$$

with

$$P(n) = \left(\frac{n}{1-\bar{n}}\right)^n e^{-n\hbar\omega_x/k_B T}, \quad (4.24)$$

where $P(n)$ is the occupation probability for a thermal state distribution and k_B is Boltzmann's constant. From this we can calculate the ratio of the intensities of the red and blue sidebands, $P_{bsb}(0)/P_{rsb}(0) = \bar{n}/(1 + \bar{n})$, and extract \bar{n} .

A spectra for a Doppler cooled and Raman cooled ion is shown in Fig. 4.10. In the Doppler cooled ion both the red and blue sideband have a large amplitude, this is because the ions wavepacket is spread out over many vibrational levels making it possible to transfer population to both a higher and lower vibrational level. However, in the Raman cooled case, only the red sideband is visible. This is due to the fact that after Raman cooling almost all the population resides in the $n = 0$ vibrational level, and while this still makes it possible to drive a red sideband, it is no longer possible to drive a blue sideband since the transition $|\uparrow\rangle|n = 0\rangle \rightarrow |\downarrow\rangle|n = -1\rangle$ is not allowed.

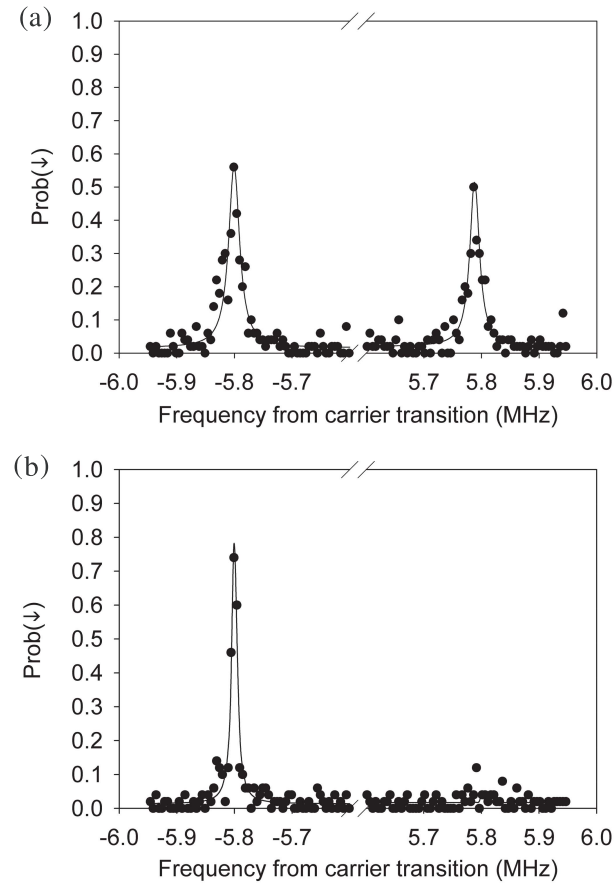


Figure 4.10: Spectrum of a Doppler cooled and Raman cooled ion for a trap frequency $\omega_x/(2\pi) = 5.8$ MHz. The top plot show the sideband spectrum on an ion after Doppler cooling, here $\bar{n} \sim 6$. The bottom plot shows the spectrum after Raman sideband cooling, here $\bar{n} \sim 0.05$. The hallmark of a cooled ion is a disappearance of the blue sideband as can be seen in the lower plot.

CHAPTER 5

Two-ion Entangling Gates

As stated in the last chapter, one of the key requirements to realizing a quantum computer is the need for a universal set of gates, consisting of both single qubit and multi-qubit gates. The multi-qubit gates presented in this chapter will allow us to map the motional state of the ions onto the spin state and entangle the ions. Although there are several schemes to realize an entangling gate, this thesis will concentrate on the gates that utilize spin dependent forces.

5.1 Cirac and Zoller Gate Scheme

The first entangling gate scheme for trapped ions was proposed by Cirac and Zoller in 1995. The proposal involved entangling two ions in a linear crystal through their collective motion. The important aspect here is that the entangled ions do not need to be neighbors for the entanglement to occur. The ions can be the first and tenth ion in the chain and this scheme will still work. The protocol to entangle any two ions k and j is:

1. Cool the ion crystal to its motional $n = 0$ ground state.
2. Apply a laser beam to ion k , this excites a motional state in the ion crystal. This maps the k^{th} qubit spin state onto the collective motional state of the ions.

3. Apply a second laser beam sometime later to ion j . Depending on the motional state, j will be unaffected by the laser beam, or its spin will be flipped.
4. Reverse step one to quench motion.

This takes the state $(|\uparrow\rangle_j + |\downarrow\rangle_j)|\uparrow\rangle_k \rightarrow (|\uparrow\rangle_j|\uparrow\rangle_k + |\downarrow\rangle_j|\downarrow\rangle_k)$, which is entangled since the state cannot be written as a product of two states. The drawbacks of this gate scheme are that the ions need to be cooled to *the* $n=0$ ground state of motion and the laser needs to be tightly focused since the ions are only spaced by a few μm . If the laser beams are not focused enough, then neighboring ions in the chain will be affected by the applied light.

Since this proposal was presented, newer gate schemes have been developed utilizing spin dependent forces to entangle the ions. These newer gate schemes, which include proposals by Milburn [22], Mølmer and Sørensen(M-S) [23], and Garcia-Ripoll [24], relax the stringent requirements necessary for the Cirac-Zoller gate.

5.2 Spin Dependent Forces

The gates proposed by Milburn, the $\sigma_z \otimes \sigma_z$, and M-S, the $\sigma_x \otimes \sigma_x$, will be the focus of the remainder of this chapter. The Garcia-Ripoll gate is an ultrafast gate and outside the scope of this thesis. This section will cover how to make a spin dependent force on a single ion.

5.2.1 Spin Dependent Forces

Applying a force to a harmonic oscillator results in the following Hamiltonian

$$H = \hbar\omega(\hat{a}^\dagger\hat{a} + \frac{1}{2}) + f^*(t)z_0\hat{a} + f(t)z_0\hat{a}^\dagger. \quad (5.1)$$

If the force $f(t)$ corresponds to a classical force of the form $F\sin[(\omega_1 - \delta)t + \phi]$ and if the detuning is much less than a trap frequency, $\delta \ll \omega$, then the interaction Hamiltonian is

written as

$$H_I = \frac{F^* z_0}{2} \hat{a} e^{-i\delta t} + \frac{F z_0}{2} \hat{a} e^{i\delta t}. \quad (5.2)$$

After a time, t , the state evolves under the evolution operator given by

$$U(t) = \exp\left[-\frac{i}{\hbar}\left(\int_0^t H_I(t') dt' + \frac{1}{2} \int_0^t dt' \int_0^{t'} dt'' [H_I(t'), H_I(t'')]\right)\right] \quad (5.3)$$

Substituting in H_I from Eq. 5.2 and just looking at the first order terms results in the displacement operator

$$D(\alpha) = e^{(\alpha \hat{a}^\dagger + \alpha^* \hat{a})}, \quad (5.4)$$

with

$$\alpha(t) = \frac{i}{\hbar} \int_0^t \frac{F z_0}{2} e^{i\delta t'} dt'. \quad (5.5)$$

This displacement operator translates motional states in position/momentum phase space and the results in coherent states of the form

$$|\alpha\rangle = e^{-1/2|\alpha|} \sum_{n=0}^{\infty} \frac{\alpha^n}{\sqrt{n!}} |n\rangle. \quad (5.6)$$

Applying two sequential displacements gives

$$D(\alpha)D(\beta) = D(\alpha + \beta) e^{i\text{Im}(\alpha\beta^*)}, \quad (5.7)$$

where the imaginary component, $\text{Im}(\alpha\beta^*)$, is the geometric phase accumulated during the operation. The complete time evolution operator can be written as $U(t)e^{i\Phi(t)}D(\alpha(t))$, and the geometric phase accumulated over the path from time 0 to t is $\Phi(t) = \text{Im}\left[\int_0^t \alpha(t') d\alpha(t')\right]$.

For a near resonant driving force with detuning δ , as in Eq. 5.2, the initial motional state moves in a circular trajectory of radius $F/(2\hbar\delta)$ and has periodicity $T = 2\pi/\delta$ in the rotating frame of harmonic motion. The state follows the path, given by Eq. 5.5,

$$\alpha(t) = \frac{Fz_0}{2\hbar\delta}(1 - e^{i\delta t}) \quad (5.8)$$

In one evolution under this force, the motional state returns to the starting position but has acquired a geometric phase of

$$\Phi_0 = \frac{\pi|Fz_0|^2}{2\hbar^2\delta^2}, \quad (5.9)$$

which is equivalent to the area enclosed by the trajectory.

Applying a spin dependent force to a single ion gives the Hamiltonian

$$H_I = \sum_{m=\uparrow_n, \downarrow_n} \left(\frac{F_m^* z_0}{2} \hat{a} e^{-i\delta t} + \frac{F_m z_0}{2} \hat{a}^\dagger e^{i\delta t} \right) |m\rangle \langle m|, \quad (5.10)$$

where m is the internal qubit state of the ion, and $|\uparrow_n\rangle$ and $|\downarrow_n\rangle$ are the eigenstates of $\hat{\sigma} \cdot \mathbf{n}$ with eigenvalues +1 and -1, respectively. Writing this Hamiltonian in terms of the $\sigma \cdot \mathbf{n}$ operator gives

$$H_I = \left(\frac{F_+^* z_0}{2} \hat{a} e^{-i\delta t} + \frac{F_+ z_0}{2} \hat{a}^\dagger e^{i\delta t} \right) \hat{\mathbf{I}} + \left(\frac{F_-^* z_0}{2} \hat{a} e^{-i\delta t} + \frac{F_- z_0}{2} \hat{a}^\dagger e^{i\delta t} \right) \hat{\sigma} \cdot \mathbf{n}. \quad (5.11)$$

Here $\hat{\mathbf{I}}$ is the identity operator and $F_\pm = (F_{\uparrow_n} \mp F_{\downarrow_n})/2$. The first term of Eq. 5.11 has no effect on the dynamics of the system and so can be ignored. Under this Hamiltonian the wavefunction evolves in time as

$$|\Psi(t)\rangle = \sum_{m=\uparrow_n, \downarrow_n} a_m e^{i\Phi(t)} |m\rangle |\alpha_m(t)\rangle, \quad (5.12)$$

where a_m is the initial amplitude of the state $|m\rangle$, $\alpha_m(t) = (F_m z_0 / 2\hbar\delta)(1 - e^{i\delta t})$ is the coherent state of spin $|m\rangle$, and $\Phi_m(t)$ is the geometric phase.

The state defined by Eq. 5.12 is a so-called Schrödinger cat state because it puts the ion in a superposition state of two places in space. The ions spin state becomes entangled with its physical position of being both “here” and “there” at the same time. When applied to a single ion, these states become a good diagnostic tool to test the phase coherence of the gate. As will be seen later in the chapter, this will be of great importance when making a two-ion entangling gate with spin dependent forces.

5.2.2 σ_z force

Making the last term Eq 5.11 proportional to $\sigma \cdot \mathbf{z}$ creates a differential force on the eigenstates of the unperturbed Hamiltonian [22]. This σ_z interaction does not require direct coupling between the two qubit spin states, but instead involves coupling between two different vibrational levels of the same spin state, as shown in Fig. 5.1. A convenient feature of this gate is that it does not require the Raman beams to bridge the 14.5 GHz frequency beatnote, but only the smaller vibrational spacing. This gate relies on a differential AC stark shift to provide a spin dependent force on the two spin states of the ion. When the beams are applied, the ion essentially sees a moving periodic potential that exerts a force on the ions in the direction of the laser beam travel. The ions will feel a force proportional to the AC stark shift amplitude, and so, if the AC stark shift has a different amplitude for each spin state, then the forces the two spin states experience are different.

The σ_z force is driven by two counter-propagating laser beams with a frequency difference of $\omega_1 - \delta$, where ω_1 is the vibrational frequency and δ is the detuning from the

$^2P_{3/2}$ —————

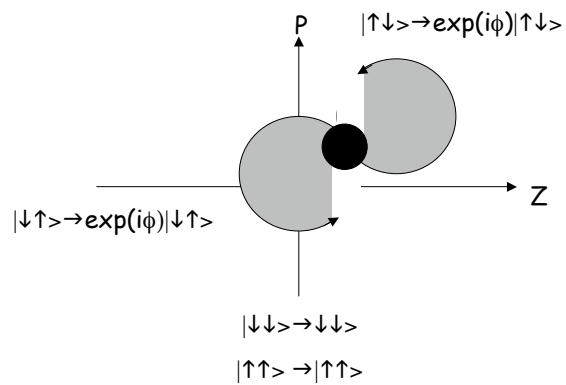
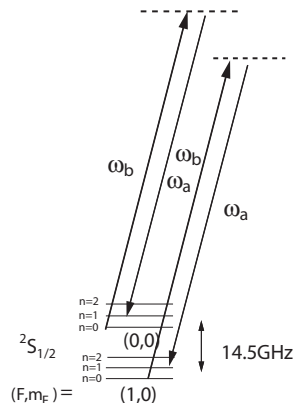


Figure 5.1: Energy level and phase space diagram for the σ_z gate. Top: Energy level diagram illustrating beam configuration for the σ_z gate. Bottom: Phase space evolution of states when σ_z gate is applied.

vibrational frequency. The resulting Hamiltonian is [25]

$$H_I = \frac{\hbar}{2} ((\chi_0 + [\Theta_0 e^{(i\mathbf{k}\cdot\hat{\mathbf{R}} - (\omega_1 - \delta)t - \Delta\phi)} + h.c.]) |0\rangle\langle 0| + (\chi_1 + [\Theta_1 e^{(i\mathbf{k}\cdot\hat{\mathbf{R}} - (\omega_1 - \delta)t - \Delta\phi)} + h.c.]) |1\rangle\langle 1|) \quad (5.13)$$

where χ_m is the time averaged Stark shift on the state $m=(0,1)$ and $\Theta_m = g_{m,A}^* g_{m,B}$ is the time-varying component in the Stark shift due to the intensity variation of the interference pattern from laser beam A and B that pushes the ion. Here $g_{m,l}$ is the single photon Rabi frequency associated with each field coupling the qubit state $|m\rangle$ to the excited state. When $\Theta_0 \neq \Theta_1$, a differential Stark shift is present and this results in a differential force between the qubit states. In the LDL, and assuming $\Delta \gg \omega_0$, the interaction Hamiltonian for two ions is

$$\begin{aligned} H_I &= \frac{\hbar}{2} \sum_{m=0,1} \eta \Theta_m D_{n,n'} (\hat{a} e^{(-i(\delta t - \phi))} + \hat{a}^\dagger e^{(i(\delta t - \phi))}) |m\rangle\langle m| \\ &= \sum_{m=0,1} \left(\frac{F_m^* z_0}{2} \hat{a} e^{-i\delta t} + \frac{F_m z_0}{2} \hat{a}^\dagger e^{i\delta t} \right) |m\rangle\langle m| \end{aligned} \quad (5.14)$$

where $F_m z_0 = (\hbar \eta D_{n,n'}/\Delta) \Theta_m e^{i\phi}$ and $\phi = \Delta\phi$.

This σ_z force only works if a differential AC stark shift exists between the two qubit levels, which is not always the case. The magnetic field insensitive clock state transitions have no differential AC Stark shift when $\Delta \gg \omega_0$ and so this gate scheme is not plausible for these levels. Instead we must use the magnetic field sensitive transitions $|\uparrow\rangle \rightarrow |S_{1/2}, F = 1 m_F = 1\rangle = |\downarrow'\rangle$ as the qubit levels for this gate. The two driving fields have a similar setup to the stimulated Raman transition fields of the last chapter. We are able to cancel the average AC Stark shift felt by the two levels while maintaining a differential AC Stark shift between the states. In this case the σ_+ and σ_- components of the fields

have opposite sign and so this results in no force on the $|\uparrow\rangle$ state, since $\Theta_0 = 0$, but the $|\downarrow'\rangle$ state feels the force $\Theta_1 = (2/3)g_A^*g_B/\Delta$ and therefore feels a differential Stark shift. Here the 2/3 prefactor comes from the transition amplitude branching ratios for the two polarization components.

Experimentally we realize the gate through the following procedure. First the ion is cooled to the ground state and initialized to the $|\uparrow\rangle$ state, applying a $\pi/2$ pulse gives $(|\uparrow\rangle + |\downarrow\rangle)/\sqrt{2}$, and then applying the $\hat{\sigma}_z$ force results in the state

$$\frac{1}{\sqrt{2}}|\uparrow\rangle|0\rangle + \frac{1}{\sqrt{2}}e^{i\Phi}|\downarrow\rangle|\alpha(t)\rangle \quad (5.15)$$

The coherent motional portion of $|\downarrow\rangle$ state evolves in time as $\alpha(t) = \alpha_0 e^{-i\phi}(1 - e^{i\delta t})$, where $\alpha_0 = \eta D_{n,n'} \Theta_0 e^{i\phi}/2\Delta$ and accumulates a geometric phase Φ . Next a $-\pi/2$ is applied to create an interference pattern between the $|0\rangle$ and $|\alpha(t)\rangle$ motional states. The probability for the ion to be in the $|\downarrow\rangle$ state is

$$P(|\downarrow\rangle) = \left| \frac{1}{2}|0\rangle_m + e^{i\Phi}|\alpha(t)\rangle_m \right|^2 \quad (5.16)$$

$$= \frac{1}{2}(1 - e^{-2|\alpha(t)|^2} \cos(\Phi(t))). \quad (5.17)$$

When we include decoherence due to temperature and motional heating effects (which are outlined in appendix B), the expected signal becomes

$$P(|\downarrow\rangle) = \frac{1}{2}(1 - e^{-1/2\dot{n}t|4\alpha_0|^2 - (\bar{n}+1/2)|2\alpha(t)|^2} \cos(\Phi(t))). \quad (5.18)$$

To realize the σ_z gate, the Raman beams are detuned from the excited state by $\Delta = 150$ GHz and have a frequency difference of $\omega_\nu - \delta$. Figure 5.2 shows the probability to be in the $|\downarrow\rangle$ state vs. the gate detuning for a gate duration of $56\mu\text{s}$.

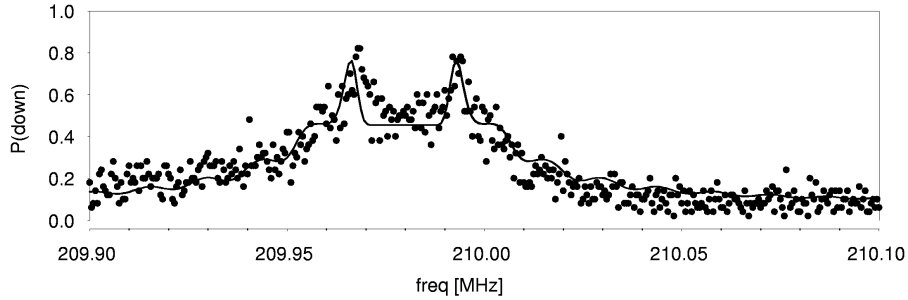


Figure 5.2: σ_z signal vs. detuning for a single ion. For this data set, the σ_z force is applied for $56\mu\text{s}$ and the data is run-time averaged with 50 experiments/point. The solid line is a fit to Eq. 5.18 with modifications to account for spontaneous emission.

Recall from Fig. 4.2 that the Zeeman transitions are extremely sensitive to magnetic field fluctuations and, as a result, may not be advantageous in algorithms that could require coherence times on the order of hundreds of milliseconds.

5.2.3 σ_ϕ force

This section will describe an alternative gate scheme that is similar to the σ_z gate but that can operate on the magnetic field insensitive clock states. Mølmer and Sørensen first proposed this gate scheme [23] and it uses a σ_ϕ -type force instead of σ_z force, where σ_ϕ is a linear combination of σ_x and σ_y operators. Since this gate operates on the clock state qubits it has a much longer coherence times than the σ_z gate. To create σ_ϕ gate, a red sideband and a blueside band with equal coupling strengths but opposite detunings are applied to the ion resulting in the Hamiltonian

$$H_I = \frac{-F_0 z_0}{2} \hat{\sigma}_\phi (\hat{a} e^{i(\delta t + \phi_m)} + \hat{a}^\dagger e^{-i(\delta t + \phi_m)}). \quad (5.19)$$

Here z_0 is the size of the harmonic oscillator ground state with center of mass oscillation frequency ω_x , the strength of the force is given by $F_0 z_0 = \hbar \Omega_{sb}$, and we assume the ions are well within the LDL. The orientation of the force's spin dependence, $\hat{\sigma}_\phi = e^{-i\phi_s} \hat{\sigma}_+ + e^{i\phi_s} \hat{\sigma}_-$,

is defined by the azimuthal angle ϕ_s where $\hat{\sigma}_\pm$ are the spin raising and lowering operators. When $\phi_s = 0$, $\hat{\sigma}_\phi = \sigma_x$. In Eq. 5.19 both the spin phase ϕ_s and motional ϕ_m depend on the phases of the red and blue sideband driving fields, ϕ_r and ϕ_b , by $\phi_s = (\phi_b + \phi_r)/2$ and $\phi_m = (\phi_b - \phi_r)/2$. In the σ_ϕ basis, the eigenstates are

$$|\uparrow_{\phi_s}\rangle = \frac{1}{\sqrt{2}}(|\uparrow\rangle + e^{i\phi_s}|\downarrow\rangle) \quad (5.20)$$

$$|\downarrow_{\phi_s}\rangle = \frac{1}{\sqrt{2}}(-e^{-i\phi_s}|\uparrow\rangle + |\downarrow\rangle). \quad (5.21)$$

Applying the σ_ϕ force to an ion initially prepared in the $|\uparrow\rangle|n=0\rangle$ state gives a wavefunction that evolves as

$$|\Psi(t)\rangle = \frac{1}{\sqrt{2}}e^{i\Phi t}|\uparrow_{\phi_s}\rangle|\alpha(t)\rangle - \frac{e^{i\phi_s}}{\sqrt{2}}e^{i\Phi t}|\downarrow_{\phi_s}\rangle|-\alpha(t)\rangle, \quad (5.22)$$

where $\alpha(t) = \alpha_0(1 - e^{i\delta t})$ with $a_0 = \eta\Omega/(2\delta)$, and $\Phi(t)$ is the geometric phase. Taking into account the effects of temperature and weak decoherence from motional heating, the probability of finding the ion in the $|\downarrow\rangle$ is

$$P_c^{(\downarrow)}(\tau) = \frac{1}{2}[1 - e^{-1/2\bar{n}\tau[4\alpha_0|^2 - (\bar{n}+1/2)|2\alpha(\tau)|^2]}], \quad (5.23)$$

where $\alpha(t) = \alpha_0 e^{i\Phi_M(1-e^{i\delta t})}$ and $\alpha_0 = \eta\Omega/(2\delta)$.

5.2.4 Producing the sideband frequencies

Fig. 5.3 shows the two possible setups for the Raman beams to generate the necessary red sideband and blue sideband beatnotes. These are the same Raman beams used in the previous chapter to drive single qubit rotations and motional transitions. As we will discuss later, the choice of geometries can greatly affect phase coherence of the spin dependent force. To generate the beams, the EOM is set to 7266 GHz and the AOM in

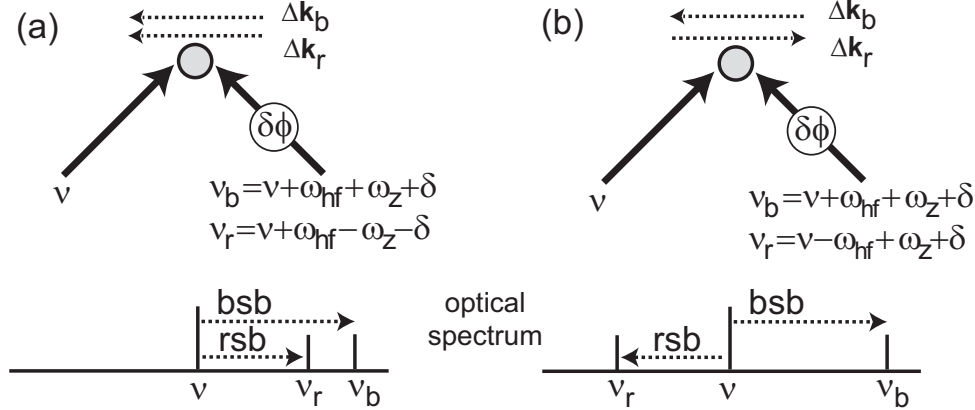


Figure 5.3: Two possible Raman beam set-ups to create the Mølmer-Sørensen σ_{phi} gate on a single ion. The top figure shows the two different setups for the Raman beams to generate the red sideband and blue sideband beatnotes. The bottom picture represents the corresponding optical spectrum. Two laser beams(solid lines) with carrier frequency ν can generate either co-propagating (left) or counterpropagating (right) Raman running waves(dotted lines) at the ion.

one arm of the M-Z is fixed at 212 MHz. For a trap frequency of $\omega_x = 3.55$ MHz, the AOM in the other arm of the M-Z is set to $\omega_a = 214.05$ MHz or $\omega_b = 209.95$ MHz to drive the first blue sideband, and at $\omega_c = 217.05$ MHz or $\omega_d = 206.95$ MHz to drive the first red sideband. For the current discussion we will chose the frequencies ω_b and ω_d to generate the gate.

Although these are the same Raman beams used to sideband cool, different microwave generators drive the cooling and gate sequences. Two frequency synthesizers are octupled in frequency to produce ω_b and ω_d and then these two frequencies are sent through a mixer, this gives the necessary difference frequency at the output of the mixer. To avoid any frequency distortion, the power is attenuated to ensure that the amplifier does not saturate. But changing the rf power changes the resonance transitions due to AC Stark shift effects. Therefore, each sideband for the gate is recalibrated by scanning the variable AOM over one of the sideband transitions while sending both sideband frequencies into the AOM. Sending both sideband frequency to the same AOM ensures that any optical fluctuations on the sidebands are common mode. The sideband that is not being directly

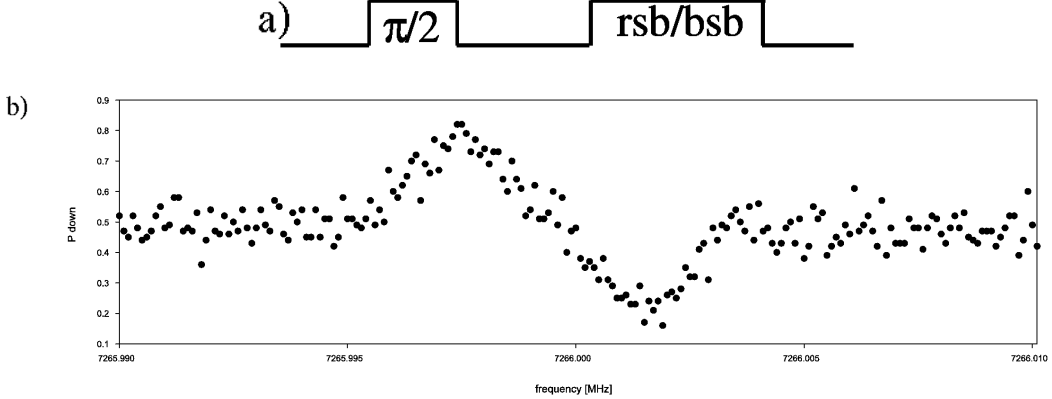


Figure 5.4: Final calibration method for setting the red sideband and blue sideband detunings, δ_r and δ_b , respectively.

scanned is put off resonance to ensure that no unwanted transitions are driven. In addition the transition rates are balanced to within 10% by attenuating one of the sideband rf sources.

Fig. 5.4 shows the final calibration method for setting the sideband detunings. Initially the sideband frequencies are set to $\delta_r = -\delta_b = 5$ kHz. We apply a microwave $\pi/2$ pulse followed by an 20 kHz EOM scan centered at 7266 MHz. The EOM scan results in an extremely accurate red and blue sideband resonance frequencies. The lower plot displays the probability of the ion to be in the $|\uparrow\rangle$ state vs. EOM frequency. For an ion initially in the $|\downarrow, n=0\rangle$ state, the red sideband produces the $|\uparrow, n=1\rangle$ state, which is the peak in Fig. 5.4, and during the blue sideband transition the population stays in the $|\downarrow\rangle$ state and this results in the dip in Fig 5.4. Setting the EOM frequency exactly between the dip and peak ensures the sideband detunings are balanced to better than 100Hz.

5.2.5 Testing the σ_ϕ force on a single ion

As a test bed for this force, we will first apply it to a single ion and this will entangle the spin and motion. This allows us to characterize the gate without the additional

complication of having a second ion. As we will see later, these single ion tests will have direct consequences for the two ion entangling gate.

The first experiment will involve fixing the duration of the force, T , while varying the detuning, δ . Fig. 5.5 shows the behavior of the gate as the detuning is varied for both an initially Doppler cooled ion and a ground state cooled ion. As Fig. 5.5(c-e) illustrates, when the detuning is far from resonance, the spin-dependent force is weak and the coherent states move in small and fast circular trajectories. As the detuning gets closer to resonance the coherent states move in larger circles and the wavepackets become further separated in space. At these larger separations the fringe contrast goes to $1/2$ because the two wavepackets are just barely overlapped and, upon measurement, each state contributes equally. When $\delta = 2r\pi/T$, where r is an integer, the coherent states return to the starting position and destructively interfere, as can be seen by a dip in the curve. On resonance, where the force is strongest, the inferred motional wavepacket separation is $\Delta z = 10z_0$, a factor of 2.8 larger than the rms size of the hot ion's thermal state. We can see from Fig. 5.5 that the hot cat has a broader envelope and narrower fringes. This is because the average over the initial thermal distribution quickly draws the experimental outcome towards $P_c = 1/2$, even for small displacements. Nevertheless, within the LDL, all initial states should return on themselves at the same moment giving a full revival. The overall decrease of contrast, clear from the non-zero baseline, is due to spin decoherence and optical pumping induced by spontaneous emission. The detuning-dependent fringe contrast is consistent with motional decoherence which has a characteristic exponential sensitivity to the motional wavepacket separation, this is largest near resonance [26, 27].

The next single ion experiment demonstrates the periodic entanglement of single ion evolution. Fig. 5.6 shows the probability of the ion to be in the $|\downarrow\rangle$ state as a function of the force duration, τ . A transition to $P_c = 1/2$ indicates the formation of an entangled state of

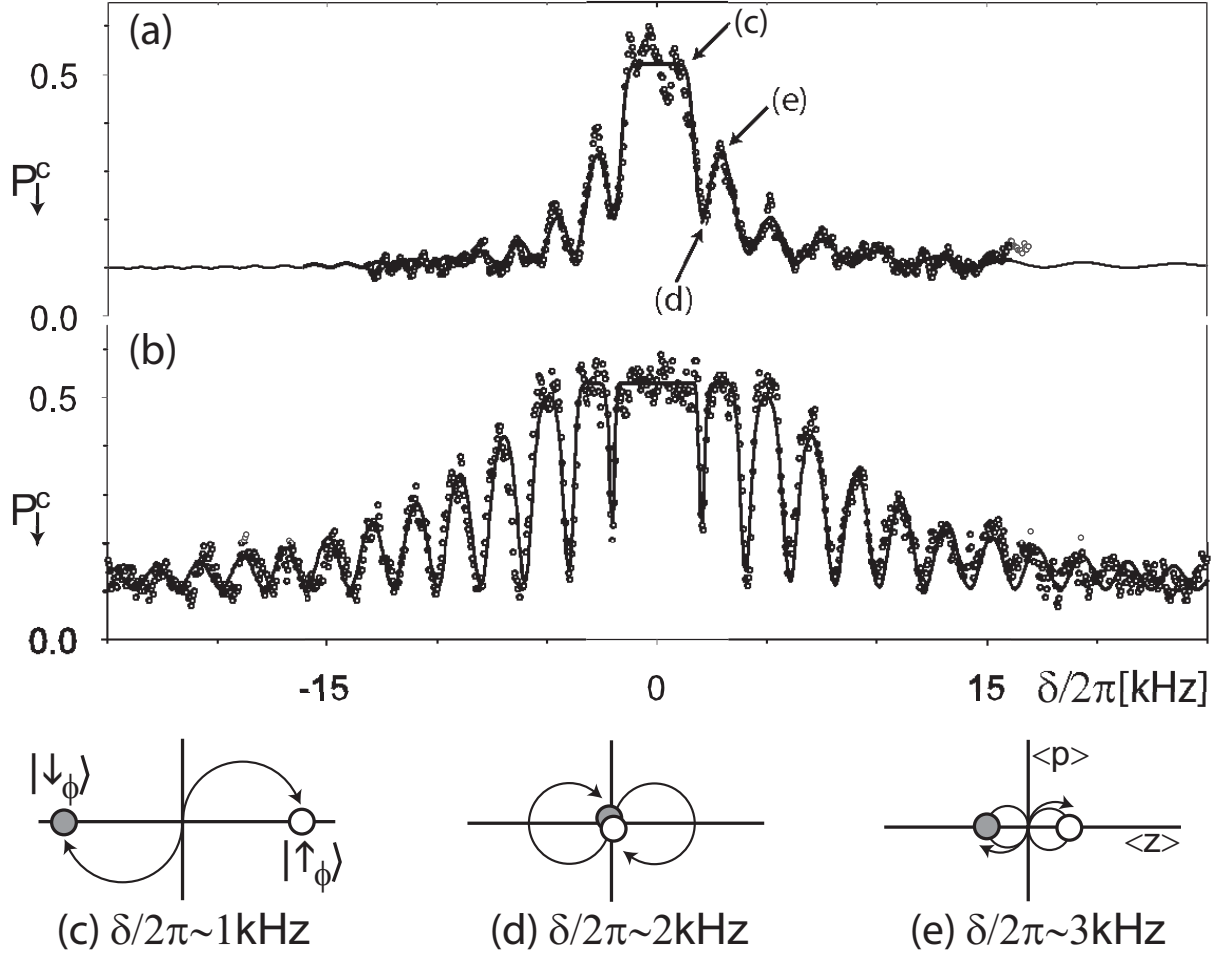


Figure 5.5: Probability for the ion to be in the bright state vs. detuning of the σ_{phi} force for (a) a ground state cooled ion and (b) a Doppler cooled ion, initially prepared in the $|\uparrow\rangle$. The force is applied for 500 μs . Data are run time-averaged with 100 shots/point. Solid lines show fits to Eq. 5.23 modified to include overall peak and contrast factors(for spontaneous emmission) and a detuning drift across the data. An initial fit to (a) assuming $\bar{n} = 0.05$ gives $\Omega_{sb}/2\pi = 1.6$ kHz and $\dot{n} = 0.4 \text{ ms}^{-1}$. A subsequent fit to (b) assuming $\Omega_{sb}/2\pi = 1.6$ kHz gives \bar{n} and $\dot{n} = 0.5 \text{ ms}^{-1}$. The values of \dot{n} are 2-3 times larger than the measure linear trap heating rate of 0.2 ms^{-1} . Phase space sketches (c)-(e) indicate ion evolution at detuning referenced in (a). [28]

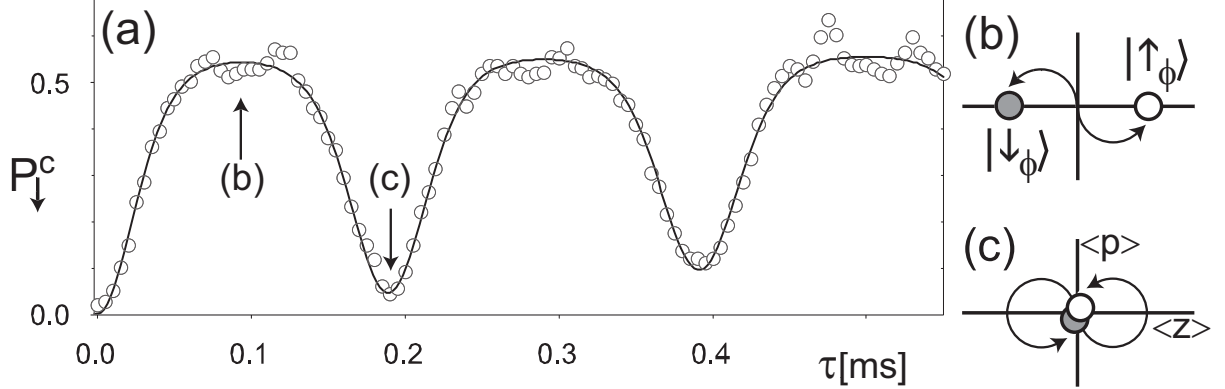


Figure 5.6: Single ion evolution from σ_{phi} force. (a). Probability P_c of measure ion in the $|\downarrow\rangle$ state plotted vs. force duration τ . Ion is initially Doppler cooled, and data run-time averaged (100shots/point). The data is fit to Eq. 5.23 but modified to include a linear change in peak and contrast (from spontaneous emission) and a detuning drift across the data. The fit gives $\delta/2\pi = -5.5$ kHz and constrains $\bar{n}\Omega_{sb}^2$ to $\bar{n} = 5 - 10$ for $\Omega_{sb}/2\pi = 2.2 - 1.6$ kHz. (b),(c) Phase space sketches of the ion motions at points indicated in (a). [28]

spin and motion. At this point, the motional wavepackets of the cat state are sufficiently far separated that spin interference is inhibited, yielding equal probability of $|\uparrow\rangle$ and $|\downarrow\rangle$. At fringe minima, corresponding to $\delta\tau = 2r\pi$ with r an integer, the motional states return to their original position and overlap. The spin interference is restored, giving the initial state $|\uparrow\rangle$ such that $P_c \approx 0$. The periodic entanglement of spin and motional degrees of freedom continues with reasonable quality for at least two oscillations.

The last experiment with a single ion is to check the phase sensitivity of the gate. Remember from earlier in the chapter that there are two possible setups for the Raman beams. From Eq. 5.19 we see that there are two phases involved ϕ_m and ϕ_s , the motional phase determines the orientation of the trajectory in phase space, while the spin phase determines spin orientation to which the differential force is applied. Both of these phases strongly depend on the optical phases of the red and the blue sideband, ϕ_r and ϕ_b . Hidden inside these sideband phases are the phases of the EOM, AOM, and the phase difference between the two Raman fields. The EOM and AOM phases can be controlled through a

stable phase lock loop between the involved generators. It is the phase difference between the two Raman fields that can be difficult to control. This phase difference is due to path length differences, $k\Delta x$, between the interferometer arms. This phase is easier to stabilize over the course of a 100 μ s gate, but difficult to maintain over longer time periods due to mechanical vibrations of the optics and the trap. For two ion experiments this phase will need to be well controlled on time scales up to 1/2 sec, to allow enough time for all the operations to be performed.

With the single ion experiments so far, there was no need to keep track of the phases ϕ_m and ϕ_s since there were no other operations being performed after the gate. But for phase gates, the spin dependent force is applied for a specific time and detuning such that the coherent states can complete an integer number of loops. After the gate is applied the spin and motion are no longer entangled, but the internal spin states of the ions are entangled. We do not want motion to play a role after the gate is applied because this could lead to motional decoherence during other operations. When we apply multiple gates to form an algorithm, the subsequent gates have no memory of the motional phase, but the spin phase is retained in the internal states of the ions and could lead to problems if it is not controlled. So we need both ϕ_m and ϕ_s to be stable over the duration of the gate and we need to be able to control ϕ_s between consecutive gates since the ions have a memory of this phase.

In order to test the phase sensitivity of the gate we need to conduct an interference experiment. Sandwiching the M-S gate between a Ramsey experiment will result in a fluorescence signal that is sensitive to the orientation of the force's spin basis. The experiment is as follows

1. Prepare the ion in the $|\uparrow\rangle$ state.

2. Apply a Raman carrier $\pi/2$ pulse with phase ϕ_0 , this creates the state $1/\sqrt{2}(|\uparrow\rangle + e^{i\phi_0}|\downarrow\rangle)$.
3. Apply the σ_ϕ force.
4. Apply a $3\pi/2$ analysis pulse to return the spin to the z-axis before measurement.

This pulse sequence will yield the ϕ_s sensitive signal

$$P_\downarrow = P_c(\tau) \sin^2(\phi - \phi_s) \quad (5.24)$$

where $P_c(\tau)$ is given by Eq. 5.23. As long as the detuning and the duration τ of the force are chosen to generate a significant displacement ($\alpha(\tau) \gg 1$), the signal is approximately $\frac{1}{2} \sin^2(\phi - \phi_s)$. If the initial $\pi/2$ pulse rotates the ion's spin state into a state in which the force is diagonal (i.e., $\phi_0 = \phi_s + r\pi$, with r an integer), a displacement occurs but no entangled spin-motion state is formed. In this case, after the analysis pulse the state returns to the initial state $|\uparrow\rangle$ and $P_\downarrow = 0$. But if the rotated initial state deviates from this special condition ($\phi_0 \neq \phi_s + r\pi$), then the state is in a superposition of the force's spin basis and an entangled spin-motion state is formed.

Experimentally a spin echo is used and the $3\pi/2$ pulse is broken up into a π pulse and a $\pi/2$ pulse, as shown in Fig 5.7. This is a convenient way to cancel the AC stark shifts that occur during the carrier pulses and the MS gate. The Stark-shift from the MS gate is canceled by applying an off-resonance bichromatic force during the second echo pulse.

The phase sensitive Raman beam setup in Fig. 5.3a produces interference fringes with nearly full contrast, as can be seen in Fig. 5.7b. In this case phase fluctuations appear on the red and blue sidebands with the same sign ($\phi_r = \phi_b$) and so they are directly written onto the MS spin phase $\phi_s = \delta_0$. For this experiment the red sideband is at 206 MHz and the blue sideband is set to 214 MHz, and the carrier sits in between at 210.5 MHz. The

carrier must sit exactly halfway between the two sidebands to ensure a consistent relative phase between the different rf signals for each trial of the experiment. The carrier pulses act as a phase reference in this experiment and are subject to the same optical phase drifts as the sidebands. And therefore, as can be seen from the fringes, the fluctuation of the forces spin phase ϕ_s are common to the reference phase ϕ_0 . These fringes remain almost at maximum contrast(maximum is 1/2) even with a piezoelectric transducer slowly modulating one Raman M-Z arm over an optical wavelength at 1 Hz.

However if the other phase insensitive Raman beam geometry is used(Fig. 5.3b), the phase correlation in the interferometric stability is washed out. Here phase fluctuations appear with opposite sign($\phi_r = -\phi_b$) and so no phase is written on the spin phase, $\phi_s = 0$. For the experiment the red sideband is set at 206 MHz, the blue sideband at 210 MHz, and the carrier at 210.5 MHz. In this case, the force's spin dependence is decoupled from instabilities and is no longer correlated with optical phase fluctuations on the carrier pulses. This configuration does not require any additional modulation to destroy the fringe contrast as the inherent phase drifts on the optical table are a sufficient noise source over the 200 ms experimental averaging time.

The phase sensitive set-up is useful for cancelling common mode fluctuations with other gate operations that are driven with Raman beams while the phase insensitive setup is useful for synchronizing operations involving microwave fields or different Raman beam geometries.

5.3 Geometric Phase Gates

After testing the σ_ϕ force on a single ion we are ready to apply it to two ions to form an entangling gate. As mentioned before, one way to create an entangling gate is with the Cirac-Zoller gate utilizes a CNOT gate. Instead of creating a CNOT gate, the gates

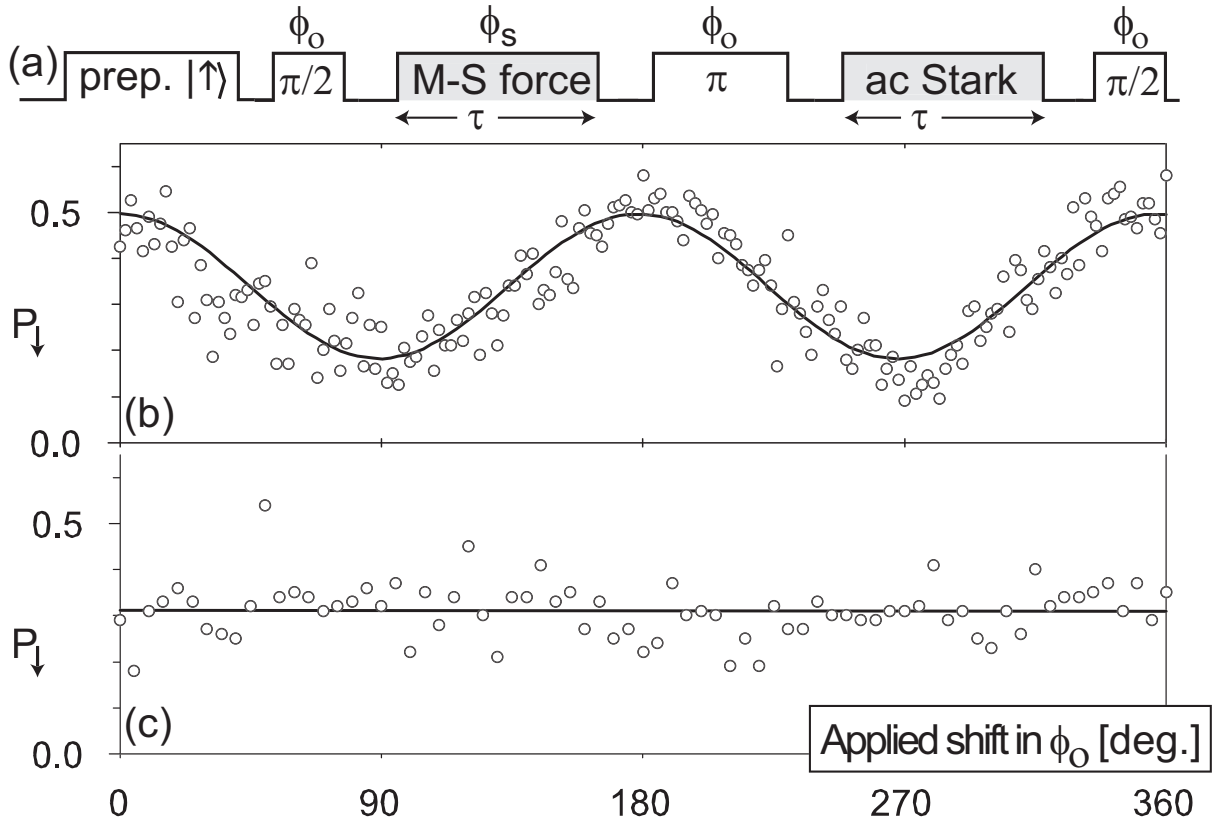


Figure 5.7: Demonstration of the phase sensitivity of the σ_{ϕ} force for different Raman beam configurations. (a) Interferometric photon-echo sequence to test optical phase sensitivity of the MS force. Phase ϕ_0 and duration of the spin-rotation pulses indicated, these are the unshaded boxes. The M-S pulse and AC Stark compensation pulse are the shaded boxes. (b),(c) Probability P_{\downarrow} plotted vs. applied shift in ϕ_0 where (b) and (c) correspond to the different Raman beam geometries. Data are run-time averaged with 100 shots/point requiring about 200 ms/point. The solid lines are a sinusoidal fit (b) and a linear fit (c).

in this chapter will focus on inducing a π phase shift on a particular state of the ions and leave the other states untouched, this section will explain how to make controlled-Z(C-Z) gates of the form:

$$\uparrow\uparrow \rightarrow \uparrow\uparrow$$

$$\uparrow\downarrow \rightarrow \uparrow\downarrow$$

$$\downarrow\uparrow \rightarrow \downarrow\uparrow$$

$$\downarrow\downarrow \rightarrow -\downarrow\downarrow$$

which can be turned into a CNOT gate with the correct choice of single qubit rotations. Together, single qubit rotations and the CNOT gate, constitute a universal set gates. Both the σ_z and σ_ϕ gates have been demonstrated experimentally [29, 30], but the σ_ϕ gate was implemented in a regime where the force is far detuned from the vibrational frequency resonance, as originally proposed by Mølmer-Sørensen. The experiment conducted here uses a near resonant spin dependent force to realize the gate.

Two ions in harmonic potential have two normal modes of vibration, they are the center-of-mass(COM) mode, $q_1 = (z_1 + z_2)/\sqrt{2}$, and the stretch mode, $q_2 = (z_1 - z_2)/\sqrt{2}$. The Hamiltonian for the system is a sum over both ions and both vibrational modes

$$H_0 = \sum_{i=1,2} \frac{\hbar\omega}{2} \hat{a}_z^i + \sum_{\nu=1,2} \hbar\omega_\nu \hat{a}_\nu^\dagger \hat{a}_\nu \quad (5.25)$$

where ω_1 and ω_2 are the COM and the stretch mode frequencies, respectively. The z component of the position operator for ion i can be written in terms of the normal mode coordinates

$$\hat{\mathbf{z}} = \frac{q_1}{\sqrt{2}} (\hat{a}_1 + \hat{a}_1^\dagger) \pm \frac{q_2}{\sqrt{2}} (\hat{a}_2 + \hat{a}_2^\dagger) \quad (5.26)$$

where $q_\nu = \sqrt{\hbar/2m\omega_\nu}$ is the root mean square spatial spread of the ground state wavepacket for the normal mode ν of oscillation, and the plus(minus) sign corresponds to $i=1(i=2)$.

The Lamb-Dicke parameters represent the strength of the coupling between the field and each normal mode and are given by $\eta_1 = \Delta k q_1 / \sqrt{2}$ and $\eta_2 = \Delta q_2 / \sqrt{2}$.

A spin-dependent force applied to two ions must couple to one of the normal modes of vibration. Here, we choose the stretch mode due to the lower heating rate. The total force now depends on the spin of both ions and the interaction Hamiltonian is

$$H_I = \sum_{m_1, m_2=\uparrow_n, \downarrow_n} \left(\frac{F_{m_1, m_2}(t) q_2}{2} \hat{a}_2^\dagger + \frac{F_{m_1, m_2}^*(t) q_2}{2} \hat{a}_2 \right) |m_1, m_2\rangle \langle m_1, m_2|. \quad (5.27)$$

Here m_1 and m_2 denote the internal qubit states of ion 1 and ion 2 and $F_{m_1, m_2} = F_{m_1} + F_{m_2}$ is the total force applied to the state $|m_1, m_2\rangle$. For a closed loop the geometric phase is $\Phi_{m_1, m_2} = 2\pi|F_{m_1, m_2} q_2|^2 / (\hbar \delta)^2$ and for simplicity we assume the force applied to both ions has equal magnitude and opposite phase, $F_{m_1} = -F_{m_2}$ for $m_1 = m_2$. Applying the gate for one full orbit results in the evolution

$$\begin{aligned} \uparrow_n \uparrow_n &\rightarrow \uparrow_n \uparrow_n \\ \uparrow_n \downarrow_n &\rightarrow e^{i\Phi_{odd}} \uparrow_n \downarrow_n \\ \downarrow_n \uparrow_n &\rightarrow e^{i\Phi_{odd}} \downarrow_n \uparrow_n \\ \downarrow_n \downarrow_n &\rightarrow \downarrow_n \downarrow_n \end{aligned}$$

where $\Phi_{odd} = 2\pi|F_{\uparrow_n, \downarrow_n} q_2|^2 / (\hbar \delta)^2$.

5.3.1 Molmer-Sorensen Gate

As mentioned earlier, in the original M-S gate scheme the σ_ϕ force is described in the limit where the frequency of the force is detuned from the resonant vibrational frequency farther than the Rabi frequency, $\delta \gg \Omega$. This results in small orbits of the coherent states and the phase is accumulated over many cycles. The operation is essentially a transition between $|\uparrow\uparrow n\rangle$ and $|\downarrow\downarrow n\rangle$ through off-resonant couplings to the $|\uparrow\downarrow n \pm 1\rangle$ and $|\downarrow\uparrow n \pm 1\rangle$ states in a four ladder system. Here we describe the case where the detuning is near resonant and the orbits are so large that the odd parity states acquire a $\pi/2$ phase

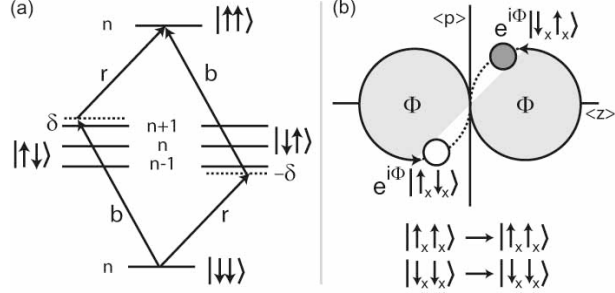


Figure 5.8: Two views of the Mølmer-Sørensen entangling gate for two ions in (a) energy space [23] and (b) motional phase space [29] for the gate-diagonal spin basis. The quantum number n and phase space coordinates describe a given collective motional mode. Red and blue Raman sideband couplings are labeled by r and b and have detuning $\delta_r = \delta = -\delta_b$. Unlike the original gate proposal, the variation shown here relies on near resonant detunings to the vibrational levels. In phase space this results in larger diameter trajectories and allows a $\pi/2$ phase shift after one complete evolution.

after one full cycle $t = 2\pi/\delta$. This situation is similar to the spin and displaced motional states described earlier in the chapter.

Fig. 5.8 shows two different views of the Mølmer-Sørensen entangling gate on two ions. Part (a) is the energy level diagram for near resonantly detuned red and blue sideband pulses. The phase space trajectory is shown in part (b). For closed trajectories in phase space, the geometric phase Φ depends on the area enclosed. To produce the gate, the red and blue sidebands are applied to both ions to give equal Rabi frequencies and balanced detunings [31, 25]. This results in a single ion Hamiltonian of the form $H \sim \hat{\sigma}_x z F_0 \sin(\omega + \delta)t$ describing a spin dependent force near resonance, here $F_0 z_0 = \eta\Omega$. The total Hamiltonian is a sum of the interactions on each ion and is a similar to Eq. 5.11. Applying the gate on the stretch mode of two ions results in a spin dependent displacement and the time evolution operator can be written as (in the σ_x basis)

$$\hat{U}(t) = |\uparrow_x \uparrow_x\rangle\langle\uparrow_x \uparrow_x| + |\downarrow_x \downarrow_x\rangle\langle\downarrow_x \downarrow_x| + e^{-i\Phi}\hat{D}(\alpha)|\uparrow_x \downarrow_x\rangle\langle\uparrow_x \downarrow_x| + e^{-i\Phi}\hat{D}(-\alpha)|\downarrow_x \uparrow_x\rangle\langle\downarrow_x \uparrow_x|, \quad (5.28)$$

where $\hat{D}(\alpha)$ is the displacement operator in the phase space of the driven normal mode.

The value of the displacement is $\alpha(t, \delta) = \alpha_0(1 - e^{-i\delta t})$ and the corresponding phase accumulated over the trajectory is $\Phi(t, \delta) = \alpha_0^2[\delta t - \sin(\delta t)]$ in terms of the parameter $\alpha_0 = \eta\Omega/\delta$. In general, the spin dependent displacement entangles the spin and motion, but for a closed trajectory, the spin and motion disentangle leaving only the spin dependent geometric phase $\Phi = 2\pi m(\eta\Omega/\delta)^2$ applied to the gate basis. A geometric phase of $\pi/2$ results in a maximally entangled state, this is achieved in the fastest time possible with $m=1$ requiring $\delta = 2\eta\Omega$ and gate time $\tau = 2\pi/\delta$. Written in the σ_z basis the gate truth table is

$$\begin{aligned}\uparrow\uparrow &\rightarrow \Psi_1 = \frac{1}{\sqrt{2}} \uparrow\uparrow + ie^{i\phi_{s1}+\phi_{s2}} \downarrow\downarrow, \\ \downarrow\downarrow &\rightarrow \Psi_2 = \frac{1}{\sqrt{2}} \downarrow\downarrow + ie^{i\phi_{s1}+\phi_{s2}} \uparrow\uparrow, \\ \uparrow\downarrow &\rightarrow \Psi_3 = \frac{1}{\sqrt{2}} \uparrow\downarrow + ie^{i\phi_0} \uparrow\downarrow, \\ \downarrow\uparrow &\rightarrow \Psi_4 = \frac{1}{\sqrt{2}} \downarrow\uparrow + ie^{i\phi_0} \uparrow\downarrow.\end{aligned}$$

The phases ϕ_0 , ϕ_{s1} , and ϕ_{s2} have been included in the even and odd parity states to account for the effect of both ac Stark shifts and Raman laser coherences, the latter modifying the spin dependence of that gate as discussed in previous sections. When $\phi_0=\phi_{s1}=\phi_{s2}=0$, the gate is reduced to $\sigma_x \otimes \sigma_x$ coupling. Note that there is no motional phase included in the above truth table, only the spin phase remains after the gate.

The experimental set up is identical to the case of one ion. The only difference with two ions is for certain Raman beam geometries the ion spacing can make a difference. To ensure that the force on the two ion stretch mode is opposite, the force of the Raman fields must be the same at the ions location. therfore the ions spacing is set equal to an integer multiple of wavelengths ($x_1 - x_2 = n\lambda$).

Just as the duration and detuning of the gate were varied in the single ion experiments, here we will repeat these processes for two ions. With both ions cooled to the ground state and initialized to the $|\uparrow\uparrow\rangle$ state, applying the gate yields a state that evolves according

to Eq. 5.28. Upon measurement, we detect the number of atoms in the $|\downarrow\rangle$ (bright) state, which is defined to be $S_{av} = 2P(\downarrow\downarrow) + P(\uparrow\downarrow) + P(\downarrow\uparrow)$. The probability to be in a particular state is

$$P(\uparrow\uparrow) = \frac{1}{4}[1 + 2e^{-\frac{1}{2}|\alpha(t)|^2} \cos\Phi(t) + \frac{1}{2}(1 + e^{-2|\alpha(t)|^2})] \quad (5.29)$$

$$P(\uparrow\downarrow) = \frac{1}{8}[1 - e^{-2|\alpha(t)|^2}] \quad (5.30)$$

$$P(\downarrow\uparrow) = \frac{1}{8}[1 - e^{-2|\alpha(t)|^2}] \quad (5.31)$$

$$P(\downarrow\downarrow) = \frac{1}{4}[1 - 2e^{-\frac{1}{2}|\alpha(t)|^2} \cos\Phi(t) + \frac{1}{2}(1 + e^{-2|\alpha(t)|^2})] \quad (5.32)$$

And so, the expected average number of ions to be in the $|\downarrow\rangle$ state is

$$S_{av} = \frac{1}{2}[1 - e^{-\frac{1}{2}|\alpha(t)|^2} \cos\Phi(t)] \quad (5.33)$$

To find the required gate detuning, we prepare the $|\uparrow\uparrow\rangle$ state and apply the gate for a time τ while scanning the detuning. We measure the average number of bright ions and compare the results to Eq. 5.33, as shown in Fig 5.9. When the time τ is set to $2\pi/\eta_2\Omega$, this plot allows us to pinpoint the required gate detuning to near $2\eta\Omega$, this condition is met when $S_{av} = 1$. Unlike the single ion case, for two ions the average brightness can be greater than 1. This is because for two of the eigenstates of $\sigma_\phi \otimes \sigma_\phi$ acquire the same geometric phase, while the remaining two states acquire no geometric phase. For the single ion case, both eigenstates experience the same geometric phase even though they experience opposite forces. So for the single ion case the brightness can never be greater than 1/2, for the two ion case it can be greater than 1.

Now that the detuning is set, the second experiment is to scan the duration of the gate pulse and monitor the average brightness. Each point of zero slope in Fig. 5.10 corresponds to the ion motion returning on itself to form a closed trajectory. The return

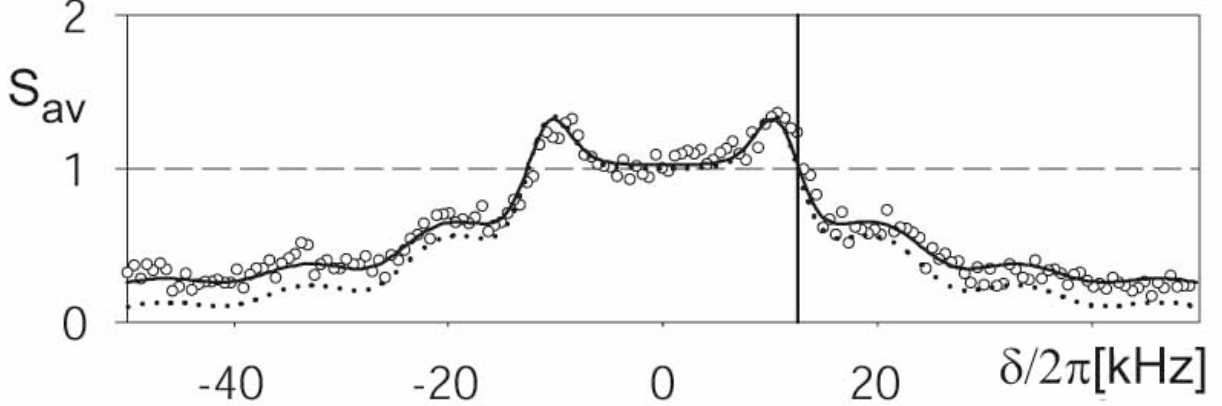


Figure 5.9: Signal from the M-S entangling gate as the detuning is scanned. When $S_{av} = 1$ the detuning is equal to $2\eta\Omega$.

points are most clearly visible in the parity signal, $\prod = (P(\uparrow\uparrow) + P(\downarrow\downarrow) - (P(\uparrow\downarrow) + P(\downarrow\uparrow))) = \frac{1}{2}(1 + e^{-2|\alpha(\tau, \delta)|^2})$. The gate operation time of $80\mu\text{s}$ corresponds to the first return. At this point the initial state $|\uparrow\uparrow\rangle$ has ideally evolved to $(1/\sqrt{2})(|\uparrow\uparrow\rangle + e^{i(\phi_{s1} + \phi_{s2})}|\downarrow\downarrow\rangle)$. After two consecutive gate pulses the system returns to the starting state $|\uparrow\uparrow\rangle$.

5.4 Characterizing the performance of the gate

The most straightforward gauge for the quality of an entangled state is the fidelity, $F = \langle \Psi || \rho || \Psi \rangle$. This is a measure of the overlap between the target state Ψ and the actual state ρ and must have a value greater than $1/2$ to show entanglement. For the Bell-like states created by the gate, the fidelity is calculated by summing the relevant diagonal terms of the density matrix with the corresponding off-diagonal terms. The diagonal density matrix terms can be extracted directly from the fluorescence histograms. From the histograms in Fig. 5.11, we can see that the sum of the diagonal elements for the target state $|\uparrow\uparrow\rangle + ie^{i(\phi_{s1} + \phi_{s2})}|\downarrow\downarrow\rangle$ is $\sim 83\%$. For the off diagonal terms a global $\pi/2$ pulse is applied to the ions, and by varying the phase of this analysis pulse, an oscillating parity signal is generated, as shown in Fig. 5.12. The amplitude of this sinusoidal is equal to

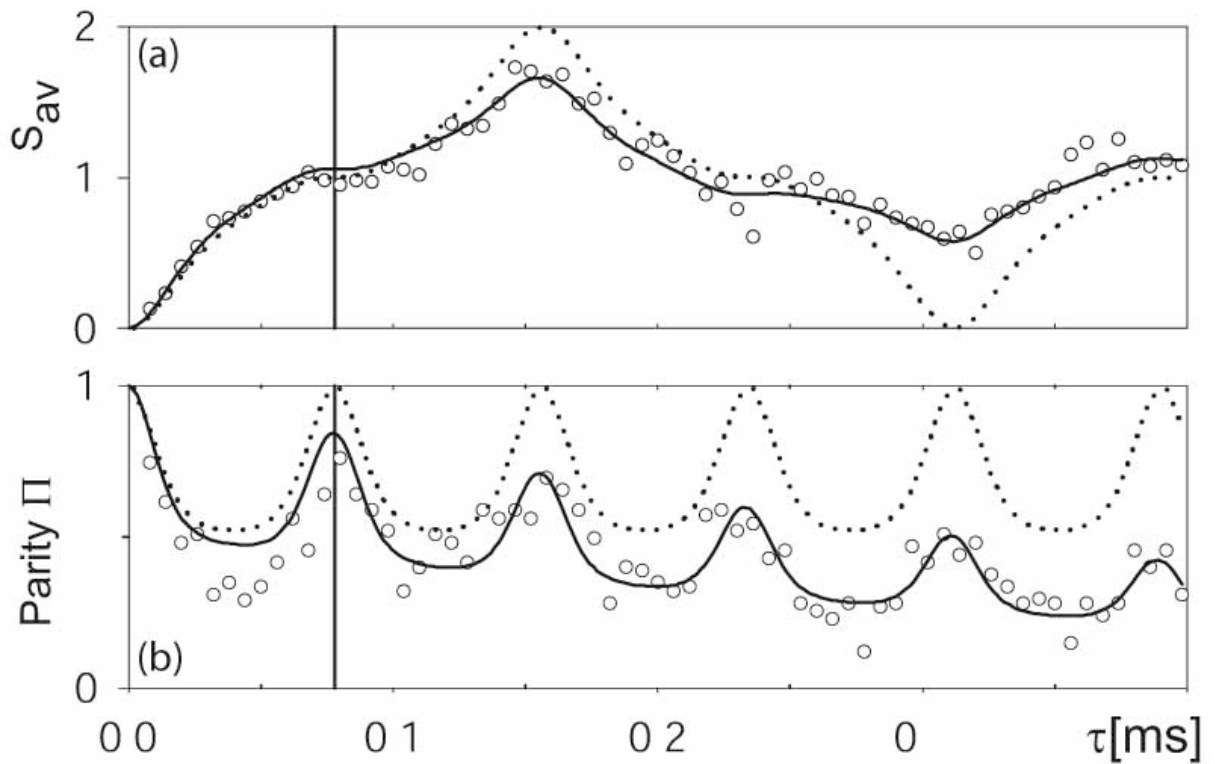


Figure 5.10: Signal from the M-S entangling gate as the gate duration is scanned. Each zero crossing corresponds to the ion motion returning on itself. As shown in the parity scan, applying the gate for $\tau = 80\mu s$ creates the state $(1/\sqrt{2})(|\uparrow\uparrow\rangle + e^{i(\phi_{s1}+\phi_{s2})}|\downarrow\downarrow\rangle)$.

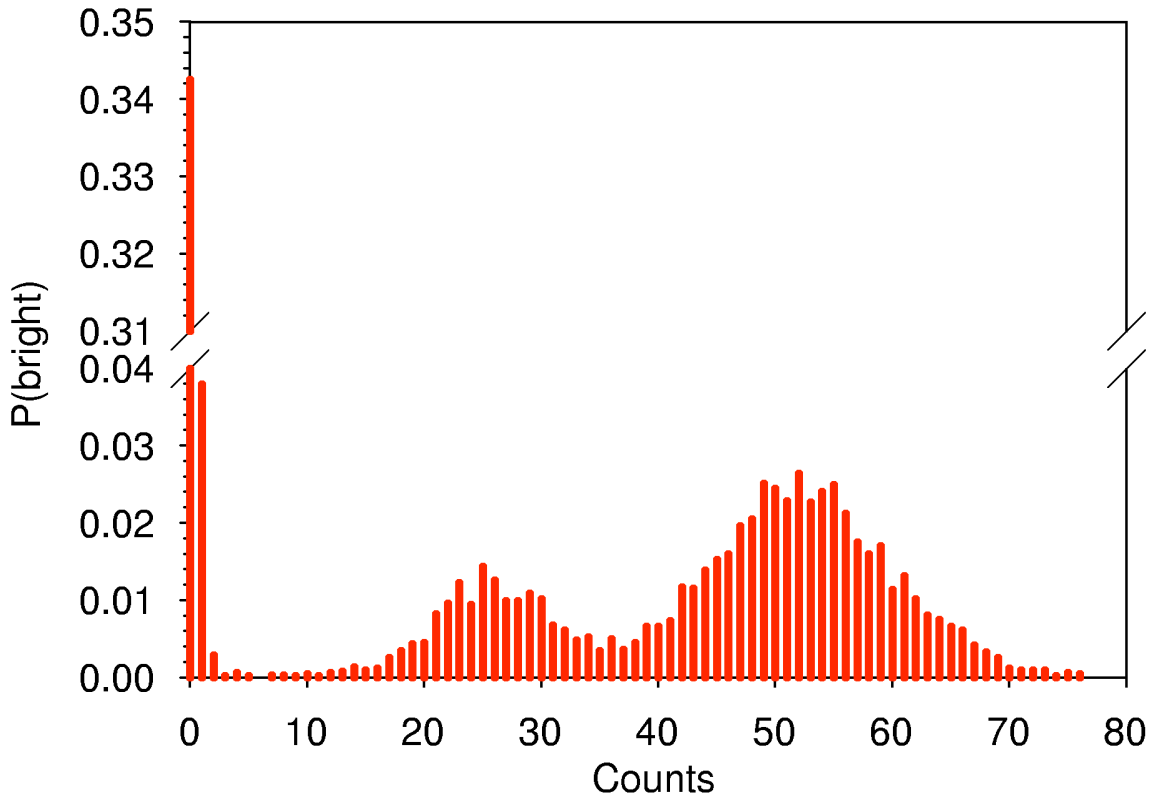


Figure 5.11: Detection histograms for the state after applying the M-S gate. The target state is $|\uparrow\uparrow\rangle + e^{i(\phi_{s_1}+\phi_{s_2})}$. The discriminators are set to 3 to distinguish the $|\uparrow\uparrow\rangle$ and $|\uparrow\downarrow\rangle + |\downarrow\uparrow\rangle$ distributions and 38 for the $|\uparrow\downarrow\rangle + |\downarrow\uparrow\rangle$ and $|\downarrow\downarrow\rangle$ distributions. With these settings, the probabilities are $P(|\uparrow\uparrow\rangle) = 0.383$, $P(|\uparrow\downarrow\rangle + |\downarrow\uparrow\rangle) = 0.168$, and $P(|\downarrow\downarrow\rangle) = 0.449$. These directly give the four diagonal elements of the density matrix.

twice the off-diagonal coherence. For the data shown the amplitude is 0.79 and, when combined with the diagonal terms, this corresponds to a fidelity of 0.81(2).

Calculating the fidelity this way gives a quick and easy measure of how well the gate is performing, but the only true way to characterize the gate is to complete a full tomographic density matrix reconstruction of the state directly following the gate. The density matrix can be decomposed in terms of a tensor product basis

$$\rho = \sum_{i,j=0}^3 r_{ij} \sigma_i \otimes \sigma_j \quad (5.34)$$

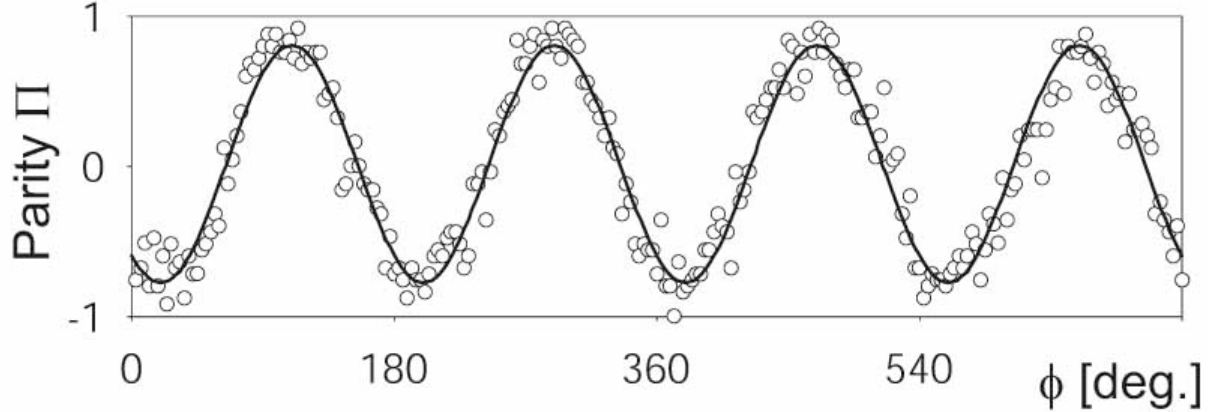


Figure 5.12: Parity vs. phase of analysis $\pi/2$ pulse applied to the Ψ_1 state. The solid line is a sinusoidal fit yielding an amplitude 0.79(2). Each point is an average over 50 PMT measurements.

where $\sigma_0 = \mathbb{I}$, $\sigma_1 = \sigma_x$, $\sigma_2 = \sigma_y$, and $\sigma_3 = \sigma_z$ are the Pauli matrices satisfying $Tr(\sigma_i\sigma_j) = 2\delta_{ij}$, and $r_{ij} = Tr(\rho\sigma_i \otimes \sigma_j)$ are real numbers. In the experiment we perform projective measurements in the nine basis combinations ($\sigma_i \otimes \sigma_j$, i,j = x,y,z) each yielding four measurement outcomes, this gives a total of 27 measurements. Experimentally we only have access to the σ_z basis, so to implement all combinations of measurements we must be able to differentially rotate single ions. Using global microwaves or Raman transitions rotates both ions by the same amount and, so, are not useful for individual qubit rotations. In order to differentially rotate the qubits we add a third beam into the experiment and purposefully misalign the beam with respect to the ions. This creates a differential Stark shift between the ions, and when combined with universal microwave rotations, allows us to rotate the ions 90° out of phase with each other, as shown in upper half of Fig. 5.13. Note that, if we apply an R_x rotation on ion 1, ion 2 will not be affected. To ensure that the ions are rotated out of phase with each other, we perform the Ramsey experiment illustrated in Fig. 5.13. The procedure to produce this graph is as follows: Apply a global $\pi/2$ pulse to both ions, introduce a differential AC Stark shift with the additional laser beam, and lastly rotate the ions with a second $\pi/2$ pulse. This last pulse rotates the ions

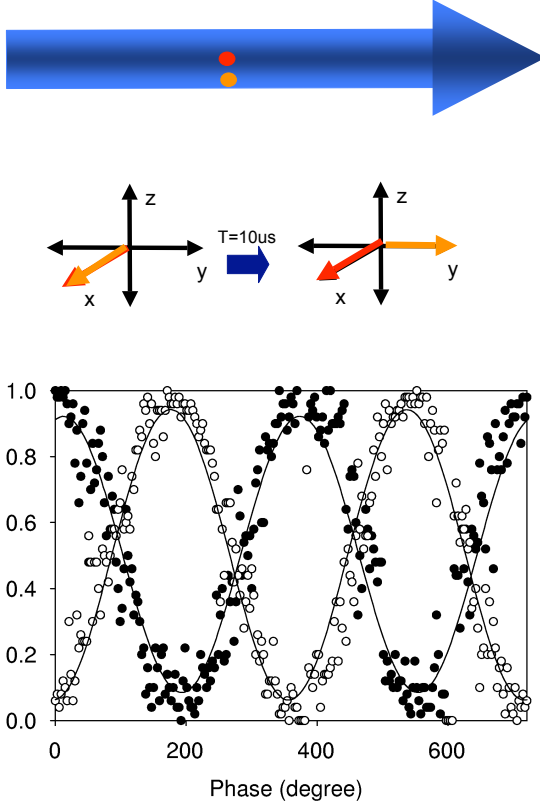


Figure 5.13: Laser beam generating differential Stark shift and phase scan showing the two ions out of phase with each other. After applying the differential Stark shifting beam we apply a global microwave $\pi/2$ pulse, since the ions are out of phase by 90° each one is rotated into a different spin state, as can be seen on the phase scan plot.

into two different basis states, as can be seen in the figure, and the two ions are 90° out of phase with each other.

projection basis	rotatation	DD	DB	BD	BB
$\sigma_z \otimes \sigma_z$	none	$\uparrow_z \uparrow_z$	$\uparrow_z \downarrow_z$	$\downarrow_z \uparrow_z$	$\downarrow_z \downarrow_z$
$\sigma_z \otimes \sigma_y$	$R(\pi/2, 0); DS; R(\pi/2, -\pi/2)$	$\uparrow_z \downarrow_y$	$\uparrow_z \uparrow_y$	$\downarrow_z \downarrow_y$	$\downarrow_z \uparrow_y$
$\sigma_z \otimes \sigma_x$	$R(\pi/2, -\pi/2); DS; R(\pi/2, 0)$	$\downarrow_z \uparrow_x$	$\downarrow_z \downarrow_x$	$\uparrow_z \uparrow_x$	$\uparrow_z \downarrow_x$
$\sigma_y \otimes \sigma_x$	$DS; R(\pi/2, 0)$	$\uparrow_y \uparrow_x$	$\uparrow_y \downarrow_x$	$\downarrow_y \uparrow_x$	$\downarrow_y \downarrow_x$
$\sigma_x \otimes \sigma_x$	$R(\pi/2, 0)$	$\downarrow_x \downarrow_x$	$\downarrow_x \uparrow_x$	$\uparrow_x \downarrow_x$	$\uparrow_x \uparrow_x$
$\sigma_x \otimes \sigma_y$	$DS; R(\pi/2, -\pi/2)$	$\uparrow_x \downarrow_y$	$\uparrow_x \uparrow_y$	$\downarrow_x \downarrow_y$	$\downarrow_x \uparrow_y$
$\sigma_x \otimes \sigma_z$	$R(\pi/2, -\pi/2; DS; R(\pi/2, -\pi/2))$	$\uparrow_x \uparrow_z$	$\uparrow_x \downarrow_z$	$\downarrow_x \uparrow_z$	$\downarrow_x \downarrow_z$
$\sigma_y \otimes \sigma_z$	$R(\pi/2, 0; DS; R(\pi/2, 0))$	$\uparrow_y \uparrow_z$	$\uparrow_y \downarrow_z$	$\downarrow_y \uparrow_z$	$\downarrow_y \downarrow_z$
$\sigma_y \otimes \sigma_y$	$R(\pi/2, -\pi/2)$	$\uparrow_y \downarrow_y$	$\uparrow_y \uparrow_y$	$\downarrow_y \uparrow_y$	$\downarrow_y \downarrow_y$

Table 5.1: Projective measurement for tomography. The second column details the rotations to transform the projection basis to the z-basis for measurement. The DS rotation is a differential stark shift rotation. For the measurement there are four possible outcomes: both ions dark DD= $|\uparrow\uparrow\rangle$ one bright ion DB= $|\uparrow\downarrow\rangle$ or BD= $|\downarrow\uparrow\rangle$, and both bright BB= $|\downarrow\downarrow\rangle$.

To reconstruct the density matrix we apply the in table 5.1. Applying this analysis to each of the four possible Bell states created from the M-S gate yields the results shown in Fig. 5.14. The reconstructed density matrices are rotated into the real coordinate for direct comparison of diagonal and off-diagonal terms. Systematics of the tomographic process are assessed after the fact based on tomographic control runs of the input states $|\uparrow\uparrow\rangle$ and $|\downarrow\downarrow\rangle$ assumed to be ideal. The results from the controls are used to extract detection biases (on the order of a few percent), microwave Rabi frequency, and applied AC Stark shifts used for qubit rotations. The inferred fidelities for the target states Ψ_1 through Ψ_4 are $F = 0.82(3), 0.89(3), 0.78(3), 0.66(3)$. The tomographically obtained fidelity for Ψ_1 agrees well with the more simple method described above. The even parity states have high fidelity because the preparations are less prone to errors since after initializing to the $|\uparrow\uparrow\rangle$ state, the $|\downarrow\downarrow\rangle$ state is created through a global π rotation with high fidelity. Fig. 5.15 displays the density matrix for the $|\uparrow\uparrow\rangle$ state, we can make this state with a fidelity of $F=0.97$ with the limitations due to the detection error of the camera. The lower fidelities for the odd-parity states is due to errors in the preparation of the $|\uparrow\downarrow\rangle$ and $|\downarrow\uparrow\rangle$ states. As Fig. 5.15 shows, a density matrix reconstruction was performed for $|\downarrow\uparrow\rangle$ state, and on average the fidelity of the preparation was $F \sim 0.85$.

Another measure of entanglement is negativity, N [32, 33]. Negativity, like fidelity, is a measure of entanglement that ranges from 0 for no entanglement to 1 for maximally entangled state. The negativity is equal to twice the absolute value of the negative eigenvalue. To obtain the negative eigenvalue, a partial transpose of the density matrix is performed and a search for a negative value in the resultant eigenvalue spectrum is performed [34, 35]. For the targets states, Ψ_i , the negativity is $0.74(6), 0.84(7), 0.60(5), 0.42(6)$. A final measure of entanglement is the entanglement of formation, E_F , which also ranges from 0 to 1. In the context of pure states, the value of E_F can be interpereted as the number nE_F

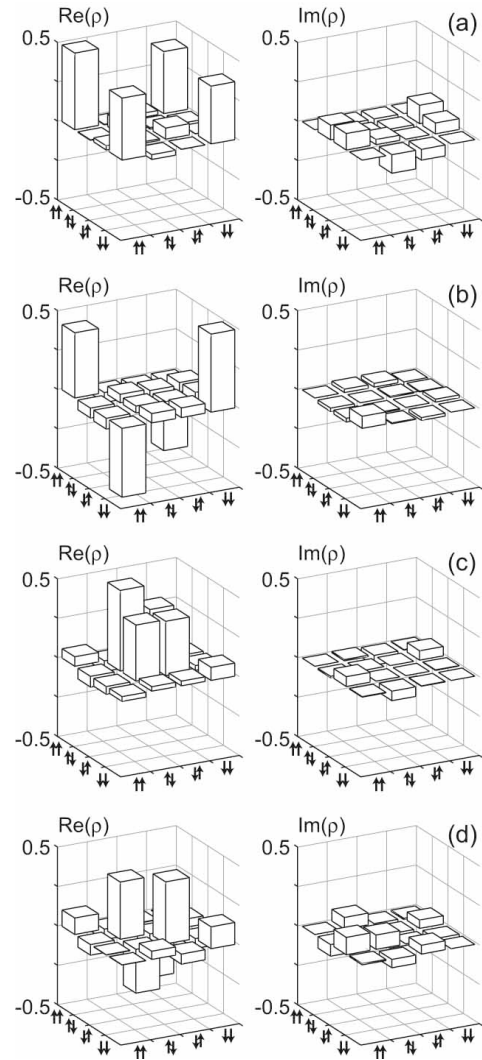


Figure 5.14: Tomography of the state directly after the M-S gate for the four possible input states. From top to bottom the input states are $\Psi_1, \Psi_2, \Psi_3, \Psi_4$, the fidelity for the odd parity states is lower due to imperfections during state preparation.

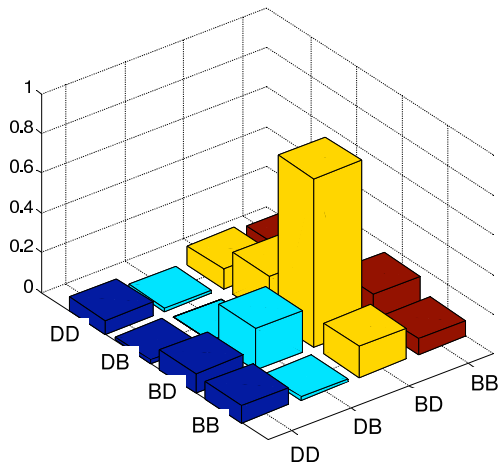
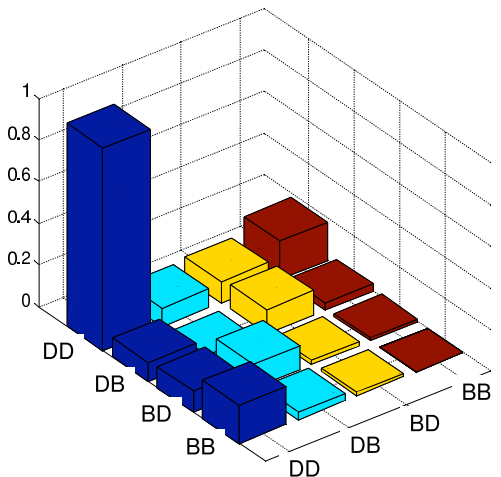


Figure 5.15: State preparation for the $|\downarrow\downarrow\rangle$ and $|\downarrow\uparrow\rangle$ states. Both even parity states have a higher preparation fidelity than the odd parity states.

of maximally entangled states required to reconstruct n copies of a given state [36]. For the data in Fig. 5.14, the values are $E_F = 0.65(8), 0.77(9), 0.49(6), 0.32(6)$. This is a more stringent indicator of fidelity and drops quickly with decreasing fidelity.

CHAPTER 6

Quantum Algorithms

6.1 Quantum Algorithms

Quantum computers promise dramatic speedup over conventional computers in some applications owing to the power of entangled superpositions [37]. Among the best-known quantum applications are the Deutsch-Jozsa algorithm (D-J), Shor’s factoring algorithm, and Grover’s search algorithm. The two main classes of algorithms are those utilizing quantum fourier transform and searching algorithms. Both D-J and Shor’s algorithm are based on quantum fourier transform, a powerful principle that leads to quantum computers capable of solving problems exponentially faster than any classical computer. While Grover’s algorithm does not attain the exponential speedup of Shor’s quantum factoring algorithm [38], it may be more versatile, by providing quadratic gains for almost any quantum algorithm [39] or accelerating NP-complete problems through exhaustive searches over possible solutions [40]. This section will outline the D-J algorithm, Shor’s algorithm, and Grover’s search algorithm. At the end of the chapter we will describe how we implemented Grover’s algorithm on a 4 element database with two trapped Cd ions.

6.1.1 Deutsch-Jozsa Algorithm

The D-J algorithm is an extension of Deutsch’s original proposal [4] in 1985 to know in a single query whether a function is constant or balanced. In 1992 Deutsch and Jozsa

expanded the algorithm to n qubits [41]. The basic idea of the algorithm is outlined as follows, suppose we have a string of binary numbers $\vec{x} = x_1, x_2, x_3 \dots, x_n$ and we are given a black box that computes $f(\vec{x})$ and returns a binary function of \vec{x} of either 0 or 1,

$f(\vec{x}) = \text{constant}$ (always 1 or always 0 for all values of x),

$f(\vec{x}) = \text{balanced}$ ($=1$ for $1/2$ of the inputs and 0 for the other $1/2$).

How many queries are needed to determine if $f(\vec{x})$ is constant or balanced? Classically we would need $2^{n-1} + 1$ queries. However, if we use quantum mechanics we can get the answer with just a single query.

The quantum protocol is

1. Initialize the state $|\Psi_0\rangle = |0\rangle^{\otimes n}|1\rangle$
2. create a superposition using Hadamard gates $|\Psi_1\rangle = \frac{1}{\sqrt{2^n}} \sum_{x=0}^{2^n-1} |x\rangle \left[\frac{|0\rangle - |1\rangle}{\sqrt{2}} \right]$
3. calculate the function $f |\Psi_2\rangle = \sum_x \frac{(-1)^{f(x)}|x\rangle}{\sqrt{2^n}} \left[\frac{|0\rangle - |1\rangle}{\sqrt{2}} \right]$
4. perform Hadamard transform $|\Psi_3\rangle = \sum_z \sum_x \frac{(-1)^{x \cdot z + f(x)}}{2^n} |z\rangle \left[\frac{|0\rangle - |1\rangle}{2} \right]$
5. measure to obtain final output z

Here a Hadamard gate is defined as $H = \frac{1}{\sqrt{2}} \begin{pmatrix} 1 & 1 \\ 1 & -1 \end{pmatrix}$. In step 4 we see that in only one measurement we can tell if the function was constant or balanced. Let's define $a_{0,1} = \sum_x \frac{(-1)^{x \cdot z + f(x)}}{2^n}$, which is the amplitude for the state to be in $|0\rangle^{\otimes n}|1\rangle$. If we measure $a_{0,1} = 1$, then, since $|\Psi_3\rangle$ is normalized, all other amplitudes must be zero and the function is constant. If we measure $a_{0,1} = 0$, then we know that there are some nonzero outputs and the function is balanced. By measuring all the qubits in the first query we can determine whether the function is constant or balanced.

Although this algorithm has no known uses, it is a fundamental proof of principle that a quantum computer can be used to speed up the computation time. Furthermore it shows how quantum interference can reduce the possible outcomes to a single state. This

algorithm was implemented for a single trapped ion in 2002 [42].

6.1.2 Shor's Factoring Algorithm

The most famous quantum computing algorithm is Shor's factoring algorithm. This algorithm uses quantum fourier transform to find the factors of a large number. If realized experimentally, this algorithm would be a massive threat to all the current encryption schemes that rely on large numbers to encode data, numbers so large that no current classical computer can factor them. The powerhouse behind this algorithm lies in the protocol to find the periodicity of a function $f(x) = a^x \text{mod} N$. The basic steps of the algorithm are shown in Fig. 6.1. They are (as outlined in [43]):

1. Initialize a first register of $n=2\log N$ bits to $|0\rangle \otimes |0\rangle |0\rangle \otimes |0\rangle \dots \otimes |0\rangle \equiv |0\rangle$ and a second register of $m=2\log N$ bits to $|0\rangle \otimes |0\rangle |0\rangle \otimes |0\rangle \dots \otimes |1\rangle \equiv |1\rangle$.
2. Apply a Hadamard gate to the first n qubits, so that the first register reaches $\sum_{x=0}^{2^n-1} \frac{|x\rangle}{\sqrt{2^n}}$
3. Multiply the second register by $f(x) = a^x \text{ mod } N$ to get $\sum_{x=0}^{2^n-1} \frac{|x\rangle |1 \times a^x \text{ mod } N\rangle}{\sqrt{2^n}}$. Since the first register is in a superposition of 2^n terms $|x\rangle$, the modular exponentiation is computed for 2^n values of x in parallel.
4. Perform the inverse QFT on the first register, giving $|\Psi_3\rangle = \sum_{y=0}^{2^n-1} \sum_{x=0}^{2^n-1} e^{2i\pi xy/2^n} |y\rangle |a^x \text{ mod } N\rangle / 2^n$.
5. Measure the qubits in the first register.

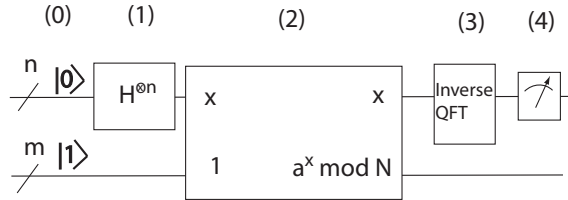


Figure 6.1: Circuit diagram to implement Shor's algorithm.

The measurement outcome in the last step is $c2^n/r$ where c is a constant, and r can be deduced on a classical computer via continued fractions. For a quantum computer the complexity of factoring a number $N \leq 2^n$ is $\mathcal{O}(n^3)$, meaning that it would take on the order of n^3 operations to factor a number. Classically a brute force search through all the possible factors would take $2^{n/2}$ operations. But even with the most efficient classical factoring algorithm, the number field sieve, it would still take $2^{cn^{1/2}(\log n)^{2/3}}$ operations. For $c=2$ this would take 6 months on a classical computer.

6.1.3 Grover's Search Algorithm

Grover's quantum search algorithm can search an unsorted database quadratically faster than any known classical search [44]. A common analogy for this searching algorithm is the problem of finding a person's name in a phone book given only their phone number [45]: for N entries in the phonebook, this requires of order N queries. However, if the correlation between name and phone number is encoded with quantum bits, the name can be found after only about \sqrt{N} queries.

At the heart of Grover's algorithm is the “oracle query,” which quickly checks if a proposed input “ x ” is a solution to the search problem. Quantum mechanically, the oracle marks a particular component of a quantum superposition by flipping the sign of its amplitude. Following the oracle, a number of quantum operations amplify the weighting of the marked state independent of which state is marked (see Fig 1). After many iterations of this query/amplification process, the marked state accumulates nearly all of the weight and is revealed following a measurement. The required number of queries can be shown to be the integer closest to $\pi/(4\sin^{-1}(N^{-1/2})) - 1/2$ [46] For $N \gg 1$, the marked element would thus appear with high probability after approximately $\pi\sqrt{N}/4$ iterations, and for the special case of $N = 4$ elements, a single query would provide the

marked element with unit probability. Classically, a single query of a 4-element search space followed by a guess can only result in a successful outcome with 50% probability.

6.2 Experimental Implementation of Grovers Algorithm

We implement the Grover search algorithm over a space of $N=4$ elements using two trapped atomic ion qubits [47, 48]. Grover’s algorithm has been implemented with ensembles of molecules using nuclear magnetic resonance [49, 50, 51], with states of light using linear optical techniques [52, 53], and with Rydberg states within individual atoms [54]. None of these systems are scalable however, as they require exponential resources as the number of qubits grows. The implementation of Grover’s algorithm reported here complements the repertoire of multi-qubit quantum algorithms recently demonstrated in the scalable system of trapped atomic ions [55, 56, 57, 58]. Unlike these earlier ion trap demonstrations, we use magnetically-insensitive “clock state” qubits and particular entangling gates that are uniquely suited to such qubits while remaining insensitive to external phase drifts between gates [31, 59, 25].

A standard quantum circuit for the Grover search algorithm for $N=4$ entries is shown in Figure 6.3(a) [37]. This scheme uses a third ancilla bit which marks one of the database elements through a Toffoli gate that effectively flips the sign of the marked element if and only if the two bit input is a solution to the problem. The oracle scheme to mark each of the four possibilities is shown below the circuit. The remainder of the circuit (shaded in dark gray) amplifies the weighting of the marked state, with the operations between the Hadamard gates flipping the sign of the amplitude of the $|00\rangle$ state.

Fig. 6.3(b) shows the experimental implementation of the algorithm for $N=4$ search elements. The Mølmer-Sørensen (M-S) entangling gate [60] is adapted to the algorithm for both the marking and state amplification steps and is accompanied by a variety of

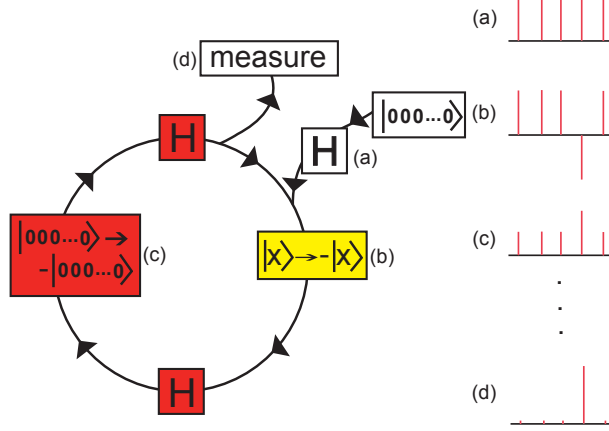


Figure 6.2: Schematic diagram of Grover’s quantum search algorithm over a space of n qubits ($N = 2^n$ entries). Initially, all qubits are prepared in the state $|000\dots0\rangle$. (a) A global Hadamard gate prepares an equal superposition of all states. (b) The oracle (shaded in light gray) flips the sign of the amplitude corresponding to the marked element, represented by the n -bit binary number x . (c) Two global Hadamard gates surround an additional phase gate (shaded in dark gray) that flips the sign of the amplitude corresponding to the initial state $|000\dots0\rangle$, amplifying the weight of the marked state. Steps (b) and (c) are repeated in sequence a prescribed number of times, and finally (d) the qubits are measured. An example of the distributions of quantum amplitudes at each stage are depicted at the right.

single qubit rotations. This circuit is identical in function to the circuit of Fig. 6.3(a) but does not use an ancilla qubit [61]. First, each qubit is initialized to the $|0\rangle$ state through optical pumping techniques. Next, an equal superposition of all qubit states is prepared with a global single qubit rotation of $\pi/2$, replacing the Hadamard gates of Figs 6.2 and 6.3(a). The oracle function (shaded in light gray) then marks one of the four possible states $|xx\rangle$ by flipping its sign. This is accomplished with a controlled-z phase gate (white boxes inside oracle) containing the M-S gate, that flips the sign of the $|11\rangle$ state. The phase gate is surrounded by rotations (shaded in black) that swap the marked state $|xx\rangle$ with the $|11\rangle$ state, depending on the settings of the of the rotation angles depicted in the table at the bottom of Fig 6.3(b). After the oracle query, a global rotation of $\pi/2$ (with a phase of $-\pi/2$ relative to the initial rotation) followed by a second application of the M-S gate amplifies the weighting of the marked state $|xx\rangle$ (operations shaded in dark gray).

The Mølmer-Sørensen gate directly entangles the clock state qubits and is insensitive

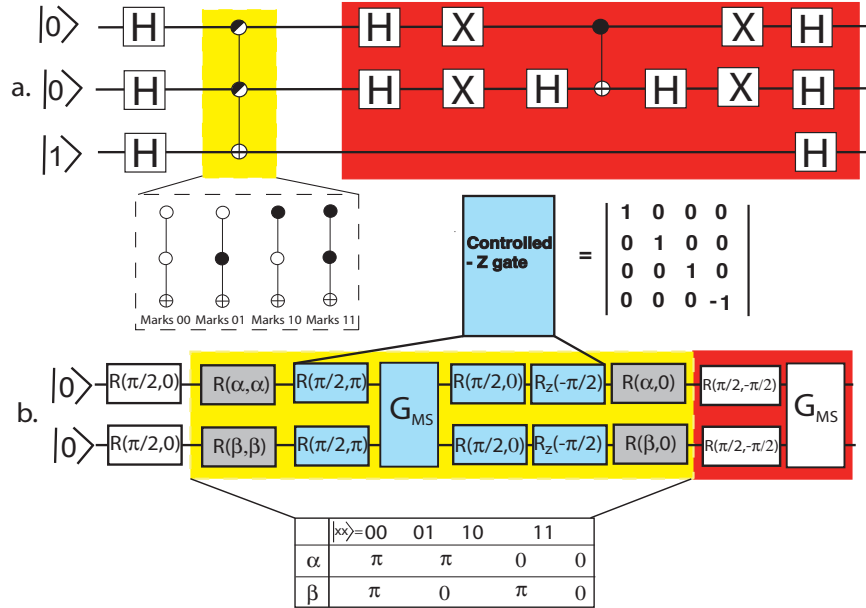


Figure 6.3: Quantum circuit to implement Grover's searching algorithm for $N=4$ entries [37]. (a.) Theoretical circuit using a third ancilla bit and standard gates including the Haddamard gate (H), the generalized Toffoli gate, a bit flip, X , and a controlled-NOT gate. The Toffoli gate implements the oracle (shaded in light gray), where the scheme to mark each of the four possibilities is shown below the circuit. The remainder of the circuit (shaded in dark gray) amplifies the weighting of the marked state. (b.) The experimental circuit to implement the algorithm for $n=2$ qubits, where $R(\theta, \phi)$ is a rotation on the Bloch sphere, $R_z(\phi)$ is a phase rotation about the \hat{z} -axis, and G_{MS} is the Mølmer-Sørensen entangling gate. The light gray shaded box identifies the oracle, where the value of the variables α and β (given in the table), determine which state is marked . The remainder of the circuit (shaded in dark gray) amplifies the weighting of the marked state.

to the relative optical phase of the Raman laser beams between gates [31, 59, 16]. This is an important consideration when multiple entangling gates are implemented because it suppresses decoherence from magnetic fields and optical phase noise that may fluctuate from gate to gate. The M-S entangling gate is realized by applying multiple sets of Raman beatnotes to the ions, simultaneously driving the first lower and upper motional sidebands for a particular duration. This entangles the spin states via their collective motional mode, in this case the stretch mode [60]. The evolution of the four basis states is given by:

$$|0\rangle|0\rangle \rightarrow |0\rangle|0\rangle - i|1\rangle|1\rangle$$

$$|1\rangle|1\rangle \rightarrow |1\rangle|1\rangle - i|0\rangle|0\rangle$$

$$|0\rangle|1\rangle \rightarrow |0\rangle|1\rangle - i|1\rangle|0\rangle$$

$$|1\rangle|0\rangle \rightarrow |1\rangle|0\rangle - i|0\rangle|1\rangle.$$

The desired states are produced with a fidelity of approximately 80%. There are additional phases not included in the above equation pertaining to the ion-ion spacing, the phase of the oscillator that defines the Raman beam beatnote, and Stark shifts from the applied Raman beams [31, 25]. These phases are set to zero for the present case since they are fixed before the experiment is run by first synchronizing the phase of the entangling gate with the phase of microwave $\pi/2$ pulses [31]. Then the phases of the two entangling gates used in the experiment are synchronized to each other through a Ramsey experiment. Note that phase noise from the Raman beam path fluctuations is suppressed due to the spectral arrangement of the Raman sidebands [16, 59]. The timescale for each operation in the algorithm is as follows: $10\mu\text{s}$ for a global microwave rotation, $20\mu\text{s}$ for a differential single qubit rotation, and $140\mu\text{s}$ for the Mølmer-Sørensen two qubit entangling gate, giving a total of $\sim 380\mu\text{s}$ to complete the 20 pulses that form the algorithm.

There are several approaches to gauging the performance of the algorithm implemen-

tation. One method is to compare the algorithm's success at recovering the marked state with the best that can be achieved classically. The classical counterpart is a simple shell game: suppose a marble is hidden under one of four shells, and after a single query the location of the marble is guessed. Under these conditions, the best classical approach gives an average probability of success $P_{cl} = 1/4 + 3/4(1/3) = 0.50$, because $1/4$ of the time the query will give the correct location of the marble while $3/4$ of the time a guess must be made amongst the three remaining choices each with $1/3$ probability of choosing the correct location. If Grover's algorithm is used, the answer to the single query would result in a 100% success rate at ‘guessing’ the marble’s location. As can be seen in figure 6.4(a) the marked state is recovered with an averaged probability over the four markings of 60(2)%, surpassing the classical limit of 50%.

It is interesting to consider the output of the algorithm when the final entangling gate used for state amplification is omitted. This situation shows how well the algorithm can do with only single qubit rotations outside the oracle. This scenario lies between the classical and quantum searches described above since entanglement is not used outside the oracle but quantum superpositions are used to find the marked element. In this case it can be shown that quantum mechanics without entanglement can do no better than what can be achieved with classical means: both methods have the outcome of finding the marked state with only 50% probability, assuming a perfect oracle. In addition, this diagnostic allows the performance of the oracle itself to be characterized. The rotations following the oracle convert the marked state into one of four Bell states each of which yields a maximum probability of 50% to recover the marked state. Figure 6.4b shows that the marked state is recovered with an average of 42(1)% probability, implying the oracle itself has a fidelity of roughly 80%.

The above figures of merit focus on the mean success probability and neglect the in-

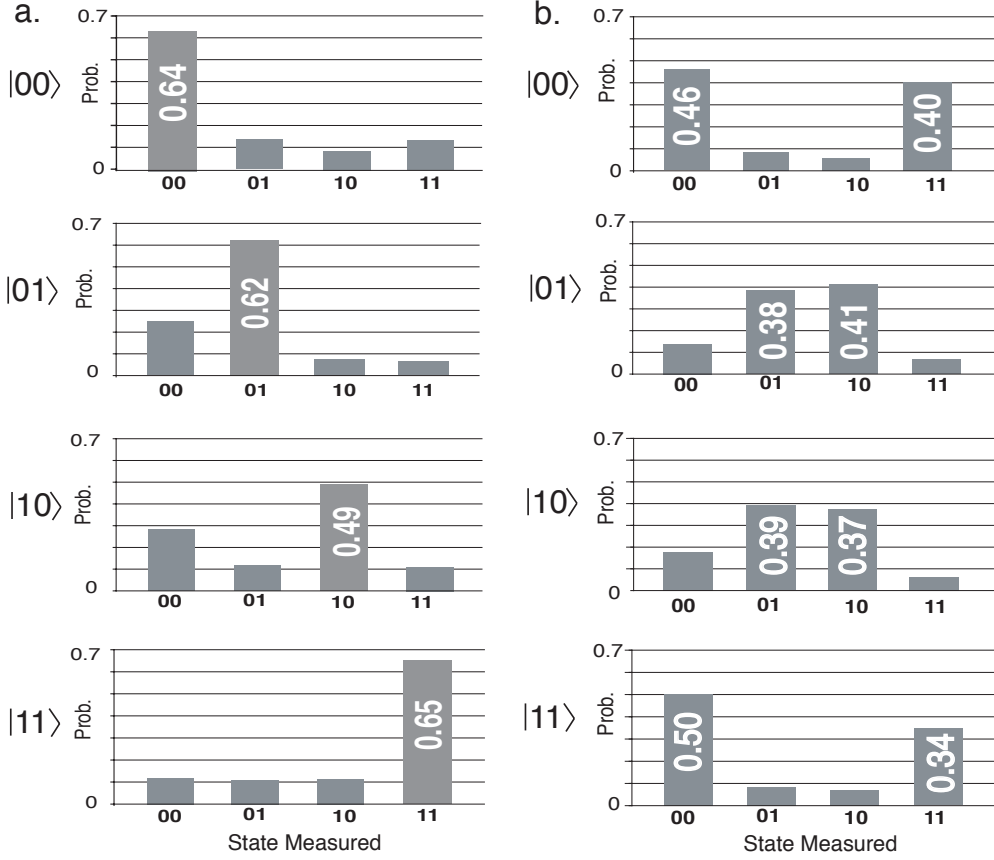


Figure 6.4: (a.) Output of the algorithm. The conditional probability of measuring each of four output states given one was marked is shown in sequence from top to bottom $|00\rangle$, $|01\rangle$, $|10\rangle$, $|11\rangle$. Each of the four data sets shows the distribution of measurements averaged over 500 trials. The marked state was recovered on average with 60(2)% compared to unit probability for the ideal quantum algorithm and 50% for the best possible classical algorithm. (b.) Output of the algorithm without the final entangling gate. This shows that the fidelity of the oracle is about 80%. Each of the four data sets was also averaged over 500 trials. The experimental average to recover the marked state is 41(2)% with the theoretical limit of 50%, both of which are less than the 60% from (a). The quoted errors are statistical.

formation content inherent in the distributions of figure 6.4a. The mutual information between the marking of the state and the measurement can be used to characterize this correlation and hence is another measure of the algorithm's success [37] (for other figures of merit see ref. [61]). The mutual information measures how much information two random variables, x , the measurement, and y , the marking, have in common. It is defined by:

$$H(x:y)=H(x)+H(y)-H(x,y), \text{ where } H(x,y)=-\sum_{x,y} p(x,y) \log_2 p(x,y)$$

is the joint Shannon entropy between the two distributions, $p(x,y) = p(x)p(y|x)$ is the joint probability distribution of x and y , and $p(y|x)$ is the conditional probability of y having been marked given that x was measured. $H(x)=-\sum_x p(x) \log_2 p(x)$ and $H(y)=-\sum_y p(y) \log_2 p(y)$ are the Shannon entropies of the individual variables. Classically the mutual information acquired after a single query of the oracle is $H(x:y)=0.25\log_2(0.25)-0.75\log_2(0.75)=0.81$ bits, meaning, on average, 0.81 bits of information are gained upon measurement. The ideal quantum algorithm would yield two bits of information upon measurement. For the data in fig.6.4a the mutual information is 0.44, so on average only about a half a bit of information is gained. Even though less information is gained per measurement than the classical case, the *probability* of finding the marked state in the experiment still exceeds the classical limit.

As the data in fig. 6.4a shows, the marked state is not recovered with unit probability. A large part of this infidelity is due to the Mølmer-Sørensen entangling gate. Each instance of the Mølmer-Sørensen gate has a fidelity of about 80%, and since there are two such gates in the algorithm, overall fidelities of approximately 60% are expected. The main sources of decoherence during the gate are spontaneous emission from off-resonant coupling to the excited state and fluctuating AC Stark shifts from the Raman beams that drive the entangling gate [59]. Both of these induced decoherence sources can be suppressed by increasing the detuning of the Raman beams from the excited

state, at the expense of slowing the gate. We choose the detuning to strike a balance between these induced decoherence sources and other slowly varying noise sources, such as motional heating [62, 63], fluctuating magnetic fields, and microwave oscillator phase drifts. Additional power in the Raman laser beams accompanied by larger detunings could suppress decoherence from spontaneous emission and AC Stark shifts while maintaining a reasonable gate speed (see [59] for more details). Fluctuating AC Stark shifts during the differential single qubit rotations due to technical intensity fluctuations and beam pointing instabilities add infidelities to the experiment on the order of 5-10%.

For Grover's algorithm to be useful it needs to extend beyond a few qubits. Using a quantum circuit similar to fig.6.3a, an n -qubit Grover algorithm can be implemented with n -qubit Toffoli gates, a series of two qubit gates, and single qubit rotations. It has been shown that an n -qubit Toffoli gate can be constructed with single qubit gates and controlled-NOT gates with order n basic operations [64]. A controlled-NOT gate can be constructed from the M-S entangling gate through the following sequence [60]: $[R_2(\pi/2, 0), R_1(\pi/2, \pi), R_2(\pi/2, \pi), G_{MS}, R_1(\pi/2, 0), R_2(\pi/2, 0), R_{z1}(-\pi/2), R_{z2}(-\pi/2), R_2(\pi/2, -\pi), R_{z1}(\pi)]$, where $R_{i=1,2}(\theta, \phi)$ is a rotation of ion i by angle θ and phase ϕ , $R_{zi}(\phi)$ is a z-rotation of ion i by angle ϕ , and G_{MS} is the Mølmer-Sørensen entangling gate. Since the ion system is scalable to a large number of qubits it is feasible to construct an efficient n -qubit Grover algorithm where each iteration scales polynomially with n . In this case, the isolation of individual ions could be accomplished through tight focusing of laser beams [65] or the shuttling of ions between separated trap zones [66, 67, 56, 57, 58].

CHAPTER 7

The Magneto-optical Trap

7.1 Introduction

The magneto-optical trap (MOT) is an indispensable source of cold atoms for a range of studies and applications in atomic physics, from precision atomic spectroscopy [68] and cold collisions [69] to atom interferometry and the generation of quantum-degenerate gases [70]. While nearly all cold atom experiments deal with the alkali atoms, there has been progress in the trapping of two-electron atomic species such as Ca, Mg, Sr, and Yb [71, 72, 73, 74], mainly for experiments involving high resolution spectroscopy of the $^1S \rightarrow ^3P$ intercombination lines. We report here the trapping of neutral Cd atoms in a deep-ultraviolet MOT operating on the $^1S_0 \rightarrow ^1P_1$ transition at 229 nm.

When producing a Cd MOT, the trapping light can also photoionize the atoms directly from the 1P_1 excited state. While this introduces losses on the trapping process, it also provides an opportunity to reliably create cold ions and atoms at the same location [75] for the investigation of ultracold atom-ion interactions [76, 77]. One interesting future possibility is the transfer of coherence between ground state hyperfine levels in a trapped ion to pure nuclear spin states in a neutral atom lacking electron spin. Because the nuclear spin can be extremely well-isolated from environmental influences [78], control of such a coherent transfer process may have applications to the long term storage of quantum

information.

In this work we realize the first Cd MOT and characterize the various trapping parameters. Results are compared with simple analytic and Monte-Carlo simulation models of the trapping process. Through a detailed investigation of the loss rate as a function of laser intensity, the absolute photoionization cross section from the 1P_1 state is determined.

7.2 Background

Cadmium has eight stable isotopes, six of which are relatively abundant. Fig. 7.1 shows the electronic structure of Cd for both bosons (nuclear spin $I=0$, even isotopes) and fermions ($I=1/2$, odd isotopes). Most of the the data presented here is for ^{112}Cd . The $^1S_0 - ^1P_1$ atomic transition used for the MOT occurs at a wavelength of $\lambda=228.8$ nm with an excited state lifetime of $\tau=1.8$ ns (radiative linewidth $\gamma/2\pi = 91$ MHz) and saturation intensity of $I_{sat}=\pi hc\gamma/(3\lambda^3) \sim 1.0$ W/cm². The saturated photon recoil acceleration on a Cd atom is $a_0 = \hbar/2\pi m\lambda = 4.4 \times 10^5 g$, which is 50 times that of Rb (here g is the acceleration due to gravity and m is the mass of a single Cd atom). Note that the 228.8 nm light can also excite atoms from the 1P_1 state directly to the ionization continuum.

In a vapor cell, the radiative forces accumulate atoms following the rate equation

$$\frac{dN}{dt} = L - \Gamma N - \beta \frac{N^2}{V}, \quad (7.1)$$

where N is the number of trapped atoms, L is the loading rate, Γ is the loss rate related to single atom effects, β is the loss rate due to binary collisions within the trap, and V is the effective volume occupied by the trapped atoms [79, 80, 81, 82]. Using simple kinetic gas theory at constant temperature one can show that $L \approx n V_c^{2/3} v_c^4 / v_{th}^3$, where V_c is the capture volume, v_c is the capture velocity [79], v_{th} is the thermal velocity, and n is the density of Cd atoms in the background vapor [83, 84]. For comparison to the data

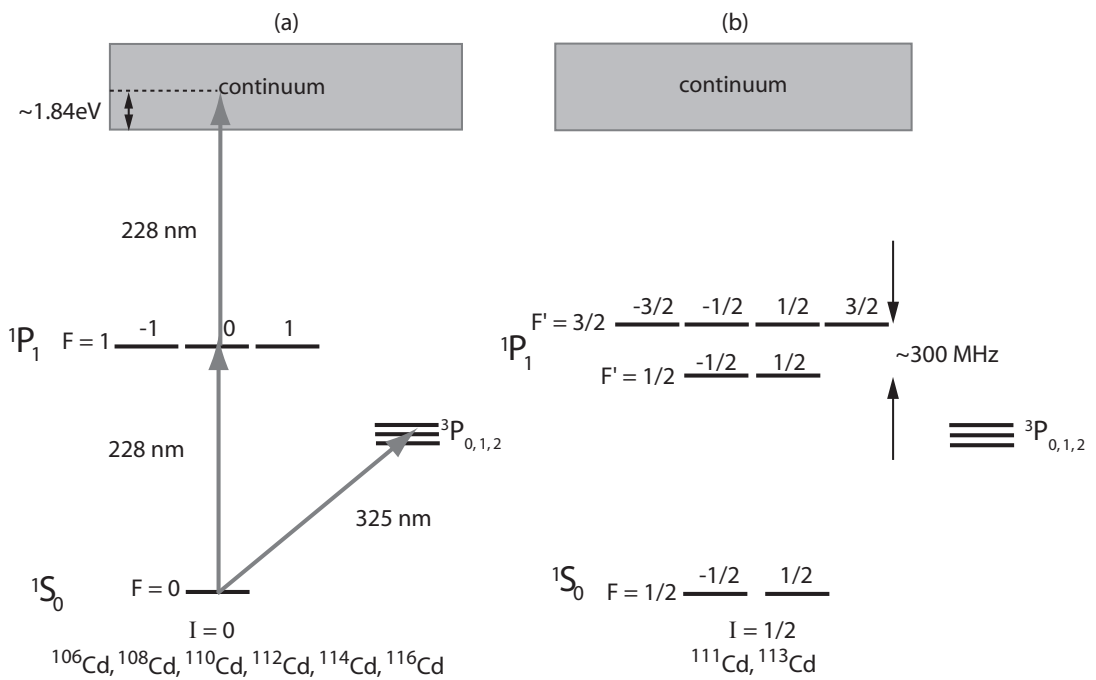


Figure 7.1: Cadmium energy level diagram (not to scale). a. The bosonic (even) isotopes ($I=0$) of Cd. b. The fermionic (odd) isotopes ($I=1/2$) of Cd, where the 1P_1 hyperfine splitting arises from $(L \cdot I)$ coupling. Individual levels are labeled with m_F .

we use a simple analytic 1-D laser cooling model to find the capture velocity, as detailed in appendix C1. Appendix C2 presents a 3-D Monte-Carlo simulation, which includes magnetic field and polarization effects, to directly estimate the loading rate.

When the MOT density is low ($< 10^9$ atoms/cm³), the atoms are essentially non-interacting and we expect the density to be limited by the cloud temperature. In this regime the spatial distribution of trapped atoms is expected to be Gaussian with a cloud radius that is independent of the trapped atom number. This contrasts with high density ($> 10^{10}$ atoms/cm³) MOTs where effects such as reradiation [85] must be considered. The Cd MOT reported here operates in the low density regime, and the last term of Eq. 7.1 can be neglected. Unlike conventional alkali MOTs, where single atom loss mechanisms primarily involve collisions between trapped atoms and the background gas, Cd (like Mg) has an additional single atom loss term due to photoionization [86, 17]. Solving Eq. 7.1 for the steady state number of trapped atoms gives $N_{ss} = L/\Gamma$, with the loss rate given by

$$\Gamma = \Gamma_0 + \Gamma_{ion}. \quad (7.2)$$

Here Γ_0 represents the rate at which trapped atoms are ejected due to collisions with the background vapor (dominated by Cd) and Γ_{ion} is the photoionization rate:

$$\Gamma_{ion} = \frac{\sigma P(I, \delta) I}{\hbar\omega}. \quad (7.3)$$

In this expression, σ is the photoionization cross section, $\hbar\omega$ is the photon energy, I is the total MOT laser beam intensity, and $P(I, \delta)$ is the fraction of atoms in the excited state

(1P_1) defined as

$$P(I, \delta) = \frac{s}{2(1 + s + 4\delta^2)}, \quad (7.4)$$

where $\delta = \Delta/\gamma$ is the laser detuning scaled to the natural linewidth and $s = I/I_{sat}$ is the saturation parameter.

7.3 Experimental Set-up and Procedure

A schematic of the experimental apparatus is shown in Fig. 7.2. Since Cd has a large linewidth, high magnetic field gradients are required to shift the Zeeman levels sufficiently for the atoms to feel a substantial trapping force at the edge of the laser beams. We use NdFeB permanent ring magnets with a 2.54 cm outer diameter, 0.64 cm inner diameter, and 0.95 cm thickness that are mounted coaxially on translational stages. By adjusting the axial separation of the magnets we can achieve magnetic field gradients up to 1500 G/cm at the trap center.

The trapping beams are generated with a frequency quadrupled Ti:Sapphire laser, yielding 2.5 mW at 228.8 nm. The ultraviolet light is split into six independent trapping beams in order to better control the intensity balance of the counter-propagating beams. The MOT can withstand an intensity imbalance of 10% between a pair of beams, and we can balance the intensity between any pair of counter-propagating beams to better than 5%. Typical beam waists range from $w = 0.5$ mm to 1.5 mm and the total power ranges from $P = 0.7$ mW to 2.0 mW, resulting in peak intensities ranging from about 0.03 W/cm² to 0.5 W/cm².

Approximately 200 μ W is split from the main laser beam and directed to a small cadmium vapor cell to stabilize the laser frequency. We use a dichroic atomic vapor laser lock (DAVLL) [87, 88] operating on the $^1S_0 \rightarrow ^1P_1$ transition in Cd. The cell is heated

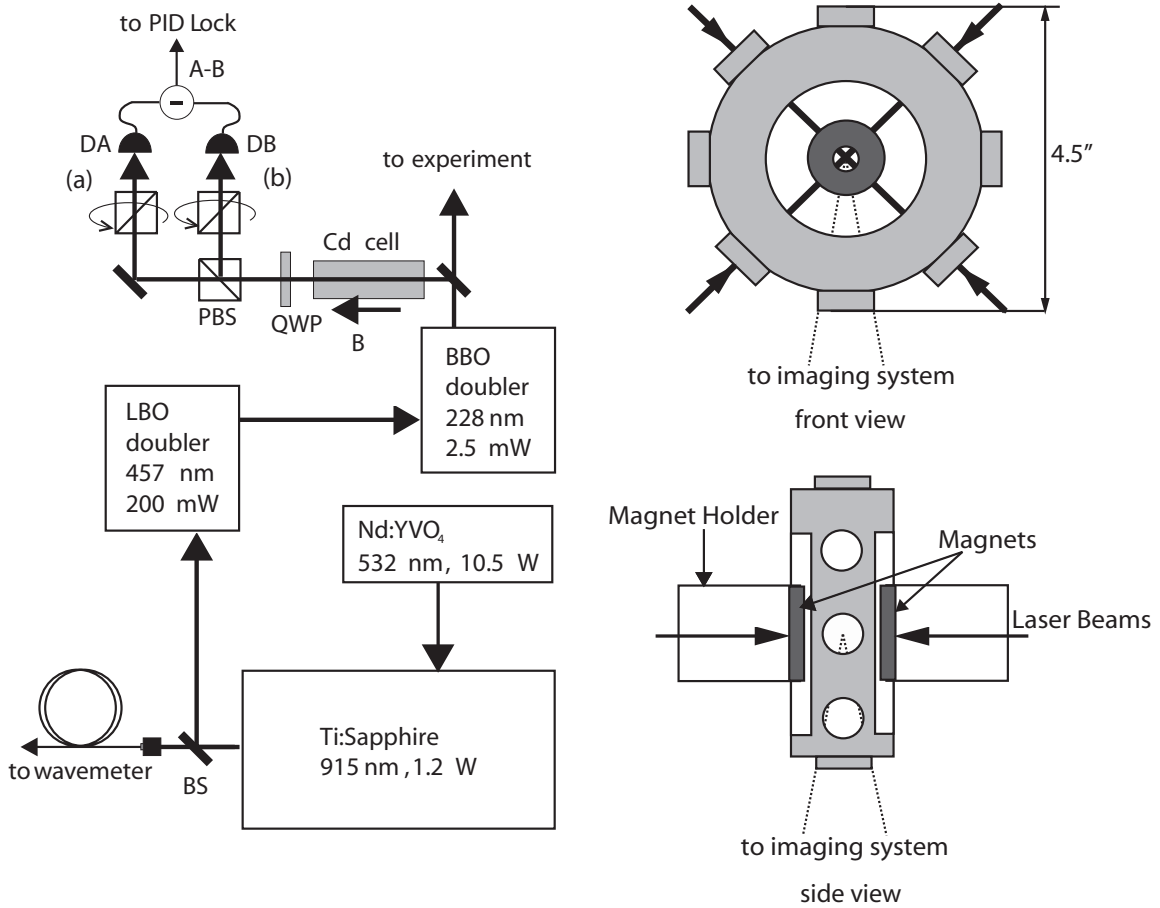


Figure 7.2: Left: Schematic diagram of the laser system and the laser lock (DAVLL). The laser lock consists of the Cd cell, a quarter wave plate (QWP), a polarizing beam splitter (PBS), and two photodetectors (DA, DB) for path a and b, respectively. Right: The MOT vacuum chamber and the laser beam geometry. The MOT is formed by 6 independent beams. The imaging system sits below the chamber, and the dark shaded regions are the NdFeB magnets.

to 80° C to increase optical absorption to about 80% through the 5 cm cell. A uniform magnetic field is applied along the laser beam axis to lift the degeneracy of the 1P_1 states. When linearly polarized light is sent through the cell the difference between absorption of the Zeeman-shifted σ^+ and σ^- transitions produces a dispersive-shaped signal and the laser is locked to the zero crossing point of this signal. The capture range is determined by the Zeeman splitting between the two transitions, or about 1.5 GHz in a 500 G field. To change the detuning we move the zero crossing point by attenuating the laser power in one of the polarization paths (a or b) after the cell (see Fig. 7.2). The lock is stable to within 30 MHz, or 0.3γ , over the 1.5 GHz capture range, and the dominant sources of fluctuations are beam-steering drifts and birefringence fluctuations of the cell windows from temperature drifts over times greater than 1 second.

The MOT chamber contains a 1 cm long hollow stainless steel tube of diameter 0.1 cm packed with about 0.02 g of pure Cd wire. We control the background Cd vapor pressure throughout the entire chamber by heating this small oven. When we direct the trapping beams into the chamber we see tracks of fluorescing Cd within the extent of the laser beams. Based on this atomic fluorescence, we estimate the background Cd vapor pressure to range between approximately 10^{-11} torr with the oven off to about 10^{-10} torr with the oven at approximately 300° C. We speculate that the Cd atoms sublimated from the oven do not readily stick to the chamber surface, resulting in good control of the Cd vapor pressure with the small oven. We note that the vapor pressure of Cd is predicted to be 10^{-11} torr at room temperature [89], which is consistent with our observations.

The atomic fluorescence from the trapped atoms is collected with an f/3 lens (a solid angle of $d\Omega/4\pi = 0.6\%$) and imaged onto an intensified charge coupled device (ICCD) camera. Every photon incident on the camera yields $\eta G \simeq 65$ counts, where $\eta=20\%$ is the quantum efficiency of the camera and G is the ICCD gain factor. Including an

optical transmission of $T \sim 50\%$ in the imaging system, we expect a total count rate of $\gamma P(I, \delta) G \eta T(d\Omega/4\pi) \sim 10^7$ counts/sec from each trapped atom in the MOT. In this way, we relate the total fluorescence count rate to the number of atoms in the MOT, with an estimated accuracy of 50%. For various settings of the MOT parameters, we are able to observe between about 10-3000 atoms in the MOT.

7.4 Results and Discussion

A typical observation of the fluorescence growth from trapped atoms in time is shown in Fig. 7.3, allowing a determination of the steady-state number of atoms and the net loss rate, Γ , from the trap. An image of the fluorescence distribution from the trapped atoms is also shown in Fig. 7.3, revealing a Gaussian-shaped atom cloud as expected from the temperature-limited density. The typical geometric mean rms radius of the MOT is 200 μm , with some dependence upon the magnetic field gradient, laser power and detuning. The largest MOT we have observed held approximately 3000 atoms, with a peak density of about 10^8 atoms/cm³.

Fig. 7.4 shows the steady state number of atoms, N_{ss} , in the MOT vs. magnetic field gradient, B' , for beam waist $w=1.25$ mm, detuning $\delta=-0.6$, and a total power $P=1.8$ mW. Under these conditions the maximum steady state number is observed at 500 G/cm. At this optimal field gradient, the Zeeman shift of the excited state levels at the edge of the laser beam is approximately one linewidth. Above this optimal value the steep magnetic field gradient shifts the atoms out of resonance with the laser beams, reducing the capture volume. At lower field gradients N_{ss} quickly decreases, presumably due to a lower trap depth resulting from an increased sensitivity to trapping parameters.

From the equipartition theorem we obtain a relation connecting the cloud radius and temperature, $\kappa r^2 = k_b T$, where r is the atomic cloud rms radius, k_b is Boltzmann's con-

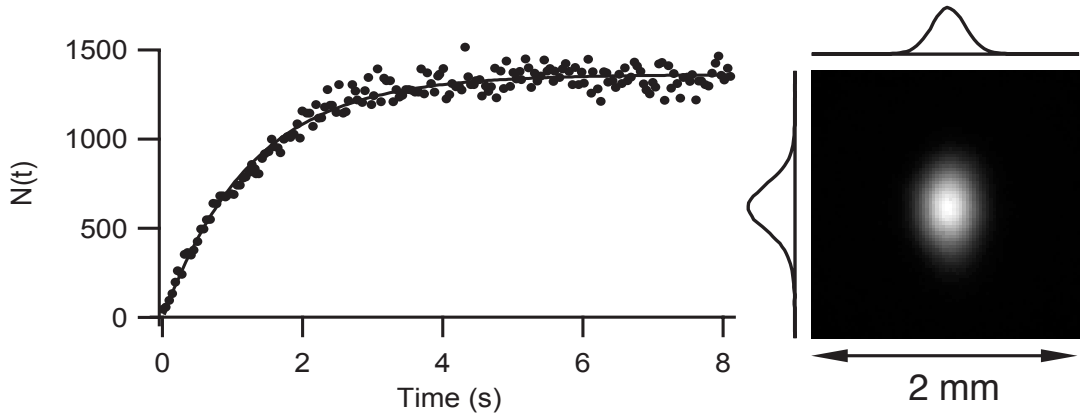


Figure 7.3: Left: Typical loading curve showing the buildup in the MOT fluorescence vs. time. For this data set, the MOT parameters are laser power $P=1.45$ mW, beam waist $w=1.25$ mm, detuning $\delta=-0.7$, and magnetic field gradient $B'=500$ G/cm. The steady state MOT number is calculated from the fluorescence signal and for this data the buildup time is 1.5 sec. Right: MOT image taken with the camera for $N_{ss}=1200$ atoms. The MOT parameters for this data set are $P = 1.45$ mW, $w=2.5$ mm, $\delta=-0.7$, and $B'=500$ G/cm. The integration time for the camera was 5 ms. A 2-D Gaussian fit to the image yields an rms radius of $200\ \mu\text{m}$ and a peak atom density of $10^8\ \text{atoms}/\text{cm}^3$.

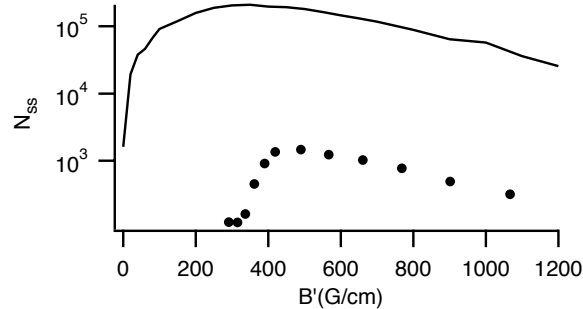


Figure 7.4: Observed steady-state MOT number vs. axial magnetic field gradient B' (points), along with the 3-D model (solid line) for $P=0.8$ mW, $\delta=-0.6$, and $w=2.5$ mm.

stant, T is the temperature in Kelvin, and κ is the trap spring constant $\kappa = 8\mu_b k s B' \delta / (1 + s + 4\delta^2)$ [19]. In this expression, μ_b is the Bohr magneton, and $k = 2\pi/\lambda$ is the wavenumber. Replacing T with the Doppler temperature, $T_D = \hbar\gamma(1 + s + 4\delta^2)/(8k_b|\delta|)$, gives a

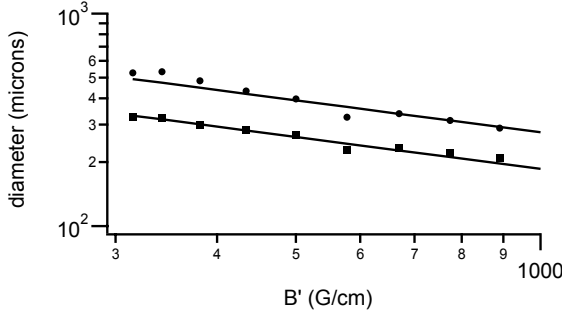


Figure 7.5: Atom cloud rms diameter vs. B' for $P=0.8$ mW, $\delta=-0.6$, and $w=2.5$ mm. A characterization is provided by the longest (circles) and shortest (squares) rms size of the elliptical MOT. The diameter is about 5 times larger than what Doppler theory predicts. The solid lines show the $(B')^{-1/2}$ dependence expected from Eq. 7.5.

relation between the temperature-limited cloud radius and the magnetic field gradient:

$$r = \sqrt{\frac{\hbar\gamma(1+s+4\delta^2)^3}{64\mu_b\delta^2ksB'}} \quad (7.5)$$

Fig. 7.5 shows the MOT rms radius vs. magnetic field gradient; as expected from Eq. 7.5, the cloud gets smaller as B' increases. The MOT diameter is roughly 5 times larger than what Doppler theory predicts. Similar results were found in Sr, where the MOT temperature exceeded the expected Doppler temperature [73].

The dependence of the steady-state number of trapped atoms on MOT detuning and laser power is shown in Figs. 7.6 and 7.7. In both figures, the experimental data is plotted along with the 1-D and 3-D theoretical predictions. The observed number of trapped atoms is 1-2 orders of magnitude below predictions, likely due to alignment imperfections and intensity imbalances not included in the models. Fig. 7.8 shows how the measured atom cloud size decreases as the MOT laser power is increased (at a fixed beam waist), as expected from Eq. 7.5.

In Fig. 7.9, the filling of the MOT is shown for Cd vapor pressures of approximately 10^{-10} torr and 10^{-11} torr. Unlike conventional vapor cell MOTs, we find that the filling

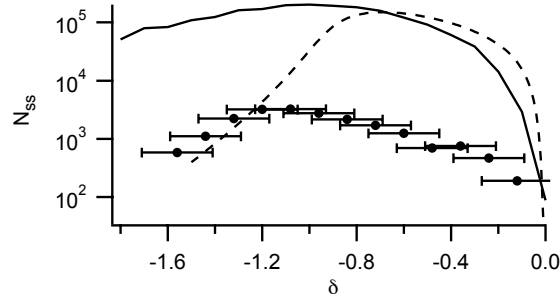


Figure 7.6: Observed steady-state atom number vs. δ (points) along with the 1-D (dotted line) and 3-D (solid line) models for $P=1.8$ mW, $B'=500$ G/cm and $w=2.5$ mm.

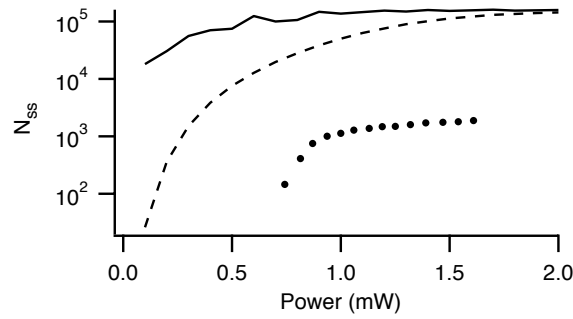


Figure 7.7: Observed steady-state atom number vs. power (points) for $\delta=-0.7$, $B'=500$ G/cm and $w=2.5$ mm along with the 1-D (solid line) and 3-D (dotted line) models.

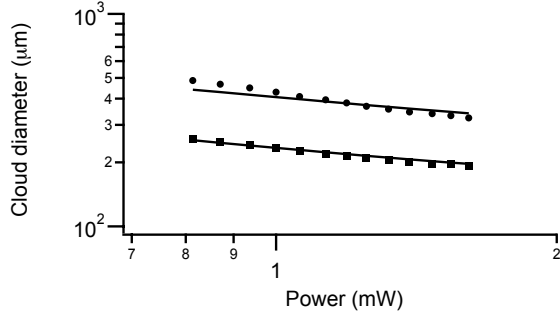


Figure 7.8: MOT cloud diameter vs. total MOT laser power for $\delta=-0.6$, $B'=500$ G/cm and $w=2.5$ mm. The solid lines show the expected dependence of the MOT diameter on power from Eq. 7.5.

time (loss rate) is independent of the background pressure, while the steady-state number of atoms in the MOT is strongly dependent on pressure. This indicates that collisions with the background gas have very little effect on the loss rate and instead we are limited

by photoionization loss from the MOT beams. This is investigated in more detail by measuring the filling time (loss rate) as the MOT laser intensity is varied, as shown in Fig. 7.10. We observe a roughly quadratic dependence of loss rate on intensity, consistent with Eq. 7.2. The extrapolated loss rate at zero intensity is much smaller than all of the observations, directly indicating that $\Gamma_0 \ll \Gamma_{ion}$, or that the loss rate in this experiment is dominated by photoionization. From this measurement, we can also directly extract the photoionization cross section from the 1P_1 state, given measurements of the intensity, excited state fraction $P(I,\delta)$, and the known wavelength of the light. We find that the photoionization cross section of the 1P_1 state of Cd from the 228.8 nm light is $\sigma = 2(1) \times 10^{-16} \text{ cm}^2$, with the error dominated by uncertainties in the laser intensity and detuning.

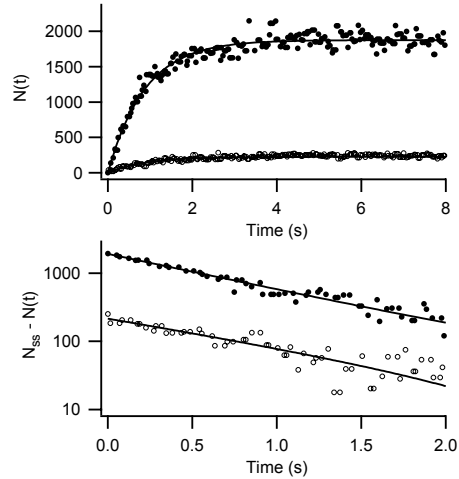


Figure 7.9: Top: Observed trapped atom number $N(t)$ for two different Cd background vapor pressures. The top curve corresponds to a pressure of 10^{-10} torr and the lower curve corresponds to 10^{-11} torr. By fitting the data to a growing exponential, $N(t) = N_{ss}(1 - e^{-\Gamma t})$, we find that the filling time, Γ^{-1} , is approximately 1 sec for each case. This is clear from the lower logarithmic plot of the data. Bottom: $N_{ss} - N(t)$ plotted for both vapor pressures on a log scale. The filling times are about 1 sec for each curve.

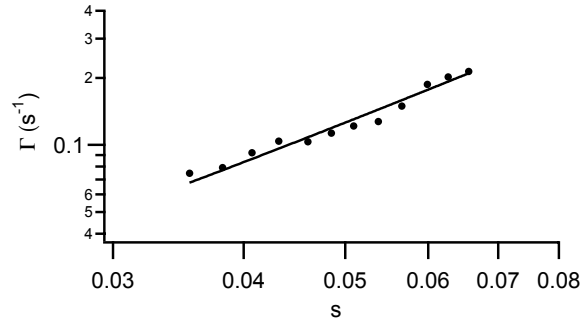


Figure 7.10: Observed loading rate vs the saturation parameter $s=I/I_{sat}$. The power is varied for a constant beam waist of $w=1.25$ mm. The photoionization cross section out of the 1P_1 state is determined from a quadratic fit to s given by Eq. 7.2. Extrapolating the curve to zero intensity (not shown here) gives information on the loss rate due to collisions with background gas.

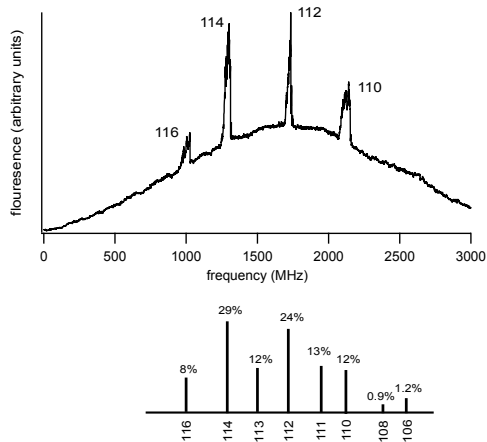


Figure 7.11: Top: Scan across frequency showing the different Cd isotope MOTs. The underlying curve is the Doppler fluorescence profile of the Cd atoms. At certain frequencies there is a large build up, due to the MOT accumulation as its resonance is crossed. Bottom: Natural abundance of neutral cadmium isotopes. Out of these eight isotopes, we are only able to clearly observe trapping of the four most abundant bosonic (even) isotopes.

7.5 Fermionic Isotopes

Scanning the laser frequency allows cooling and trapping of different cadmium isotopes, as shown in Fig. 7.11. We observe that the peak heights correspond to the natural abundance of each isotope, showing that the bosonic isotopes are equally capable of being trapped. However, there is a lack of evidence for the fermionic isotopes being loaded in

the MOT. This is due to the hyperfine structure present in the 1P_1 states of the fermionic isotopes. As shown in Fig. 7.1b, the two excited hyperfine states for both ^{111}Cd and ^{113}Cd are separated by about 300 MHz, which is comparable to the natural linewidth of Cd. A laser tuned to the red of the upper hyperfine state ($F'=3/2$) but to the blue of the lower hyperfine state ($F'=1/2$) may drive excessive transitions to the lower excited state, which could result in too much heating and prevent trapping. In addition, the optical transitions between the $F=1/2$ ground states and $F'=1/2$ excited states do not result in spatially dependent differential optical pumping by σ^+ and σ^- transitions, a necessary condition for a standard MOT. Similar results were reported for Yb [74], where much smaller or no MOT was observed for fermionic isotopes. In the present case it could be that there is a very small fermionic MOT being formed but it is not resolvable from the background noise. It may be possible to laser cool and trap fermionic isotopes with a dichroic MOT [90]. Here, the cooling laser is tuned to the red of the lower hyperfine transitions ($F'=1/2$) to provide the major scattering force for laser cooling and then a small fraction of the laser power is frequency shifted to the red of the upper hyperfine state (blue of the lower state). When this second laser beam is collimated with a smaller beam waist, and overlapped with the beam of the first color, the laser cooled atoms can be trapped in the MOT by driving the upper transitions ($F=1/2$ to $F'=3/2$). Alternatively, one can work in a much higher magnetic field gradient to overwhelm the excited state hyperfine structure. In this Paschen-Bach regime, one will drive $J = 0$ to $J = 1$ transitions to produce a MOT. Given a beam waist of 1.0 mm, the required field gradient for the MOT will be on the order of 10^4 G/cm, which can be realized by a pair of needle electromagnets [91]. The capture volume of the MOT will be much smaller, but this scheme may still be useful for single-atom MOT experiments. Another alternative is to use a higher laser power allowing one to tune to the red of both hyperfine states. With a larger detuning,

$|\delta| \gg \delta_{hf}$, the optical excitation to the lower and upper manifolds is driven more evenly and can produce both cooling and trapping forces for the atoms.

7.6 Conclusion

In this paper we present the first Cd magneto-optical trap, operating on the $^1S_0 - ^1P_1$ transition at 228.8 nm. A characterization of the MOT as a function of magnetic field gradient, detuning, and intensity is presented. The same beams that form the MOT also photoionize the atoms inside the MOT. We observe photoionization as the dominant loss mechanism, and characterize the photoionization cross section.

This system, when combined with cold ions, opens the possibility of studying ultracold charge exchange collisions. One outcome of these studies is the possible transfer of coherent information from the ion to the neutral atom. A possible experiment is to prepare the ion in a quantum superposition of the hyperfine qubit states and then allow the ion to undergo an ultracold charge exchange with a nearby neutral atom. This results in the charge neutralization of the ion, but could also leave some of the previously prepared quantum information intact in the nucleus. This could allow quantum information to be carried by pure nuclear spins with very little interaction with the environment. Subsequent coherent charge exchange with another ion could then allow the nuclear quantum information to be manipulated and processed using conventional ion trap techniques. In addition to applications for quantum information, the long-lived 3P_0 state could be of interest for optical clocks [68] and the narrow linewidth of the 1S_0 - 3P_1 transition (70 kHz) would allow for an extremely low cooling limit [73].

CHAPTER 8

Conclusion

In this thesis we have experimentally implemented all of the requirements for a quantum computer and realized a small scale searching algorithm for two trapped Cd ions. We have exhibited that the M-S entangling gate is a preferred gate scheme since it operates on the magnetic field insensitive qubit states. This allows for longer coherence times during operations since the magnetic field insensitive qubits decohere much slower than the magnetic field sensitive states, as was shown in Chapter 4. And though other trapped ion groups have created entangling gates [30, 29, 65, 92], we have gone a step further by controlling the phase between two consecutive gates and demonstrating that the phase due to the optical fields creating the gate can be eliminated. This is an important step in quantum computing because future algorithms will have more than two consecutive gates and any phase noise between the gates will likely interfere with the operation being performed. Ultimately this phase noise is an extra source of decoherence for the qubit states and must be eliminated.

One of the biggest issues left to tackle in trapped ion quantum computing is scaling the system up to an arbitrary number of qubits. In principle all the work done in this thesis can be scaled up with polynomial resources, not exponential. This is an important point for the scalability of a system. Current efforts include fabricationg novel ion traps with

new structures to make electrode connections simpler and make the assembly process easier by growing the traps out of materials such as GaAs and Si. Another big issue is that of error correction. To truly implement a large scale quantum computation additional qubits will be needed for error correction purposes. This is an area that is not as heavily studied as the other areas covered in this thesis, but in the future more work will be done towards this goal as the algorithms being created get more complicated.

This thesis also presented new ideas for quantum information processing involving neutral atoms and ions, and although this field is a new one, there is a great amount of work to be done. Combining the two systems could lead to a more robust quantum computer with longer storage and safer transportation available in the neutral atoms while the ions hold higher levels of manipulation and easier readout schemes.

APPENDICES

APPENDIX A

Raman Beam Effects: Rabi Flopping, Spontaneous Emission, and the AC Stark Shift

A.1 Raman Beam Effects

A.2 Rabi Flopping

For our qubit states we use the $S_{1/2}$ ground state hyperfine levels, in particular we use the (0,0) and (1,0) states. Stimulated two photon Raman transitions are used to drive spin flips between the two qubit states. For this process we use a laser beam detuned 300 GHz from the $P_{3/2}$ excited state. This third level is adiabatically eliminated in the process and so we can think of the states as a two level system. The equation governing this system is:

$$|\psi\rangle = \cos\left(\frac{\Omega t}{2}\right)|\downarrow\rangle + i\sin\left(\frac{\Omega t}{2}\right)|\uparrow\rangle \quad (\text{A.1})$$

The probabilities to be in the $|\downarrow\rangle$ or $|\uparrow\rangle$ are as follows:

$$P(\downarrow) = \cos^2\left(\frac{\Omega t}{2}\right) = \frac{1}{2} - \frac{1}{2}\cos(\Omega t) \quad (\text{A.2})$$

$$P(\uparrow) = \sin^2\left(\frac{\Omega t}{2}\right) = \frac{1}{2} - \frac{1}{2}\cos(\Omega t) \quad (\text{A.3})$$

where:

$$\Omega = \frac{g_1 g_2}{2\Delta} \quad (\text{A.4})$$

with $g = \frac{\gamma}{\sqrt{2}} \sqrt{\left(\frac{I}{I_{sat}}\right)}$, which is the transition strength between one qubit state to the excited state and $I = 2 * P/\pi * w^2$, the laser intensity. We assume $g_1 = g_2$ and $I_1 = I_2$.

In our experiment: $\gamma = 50MHz, \Delta = 236GHz$ (for Raman laser at 858.1710nm), $w = 10.97\mu m, P_{det} = 300\mu W, I_{sat} = .006\mu W/\mu m^2, I/I_{sat} = 263$

For these values we expect a Rabi frequency of $\Omega = 696.5kHz$, but this is without taking polarization or the Mach-Zehnder interferometer into account.

A.2.1 Mach-Zehnder contribution

To generate a beat-note frequency at 14.5 GHz we use an electro-optic modulator. This generates a frequency comb on the laser beam, with each line of the comb separated by 7.25 GHz. Then every pair of lines spaced by 14.5 GHz can drive a Raman transition. The EOM is placed prior to the last doubling stage in the blue and then the entire comb is sent through a doubling cavity to generate UV light. The output directly after the EO is:

$$E_{blue} = E_o e^{(i(kx - \omega t))} \sum_{n=-\infty}^{+\infty} \frac{J_n(\phi)}{1 - 2i\delta n} \exp(in(\delta kx - \Omega t)) + c.c \quad (\text{A.5})$$

Then after the doubling cavity the UV spectrum is as follows:

$$E_{uv} = \eta E_o^2 e^{(2i(kx - \omega t))} \sum_{m=-\infty}^{+\infty} \sum_{n=-\infty}^{+\infty} \frac{J_n(\phi)}{1 - 2i\delta n} \frac{J_m(\phi)}{1 - 2i\delta m} e^{(i(n+m)(\delta kx - \Omega t))} + c.c \quad (\text{A.6})$$

Lots of equations(to be filled in later) gives a factor of 0.244 to the Rabi frequency....taken directly from EOM paper. So with this $\Omega = \frac{0.244g_1g_2}{2\Delta} = 169.95kHz$

A.2.2 Polarization

To check our polarization we measured the Rabi frequency of the upper and lower Zeeman levels and compare to the carrier frequency.

We generate our Raman transitions with 2 beams, a north beam and a south beam.

In general terms we can write each field as:

$$E_N = \epsilon_N(a_N\hat{\sigma}^+ + b_N\hat{\sigma}^- + c_N\hat{\pi}) \quad (\text{A.7})$$

$$E_S = \epsilon_S(a_S\hat{\sigma}^+ + b_S\hat{\sigma}^- + c_S\hat{\pi}) \quad (\text{A.8})$$

with the condition that:

$$|a_N|^2 + |b_N|^2 + |c_N|^2 \quad (\text{A.9})$$

$$|a_S|^2 + |b_S|^2 + |c_S|^2 \quad (\text{A.10})$$

We can write the Rabi frequency as: $\Omega = \sum_m \frac{\langle f|E_S^*|m\rangle\langle m|E_S^*|i\rangle}{2\Delta}$

Then we can write the Rabi frequencies of each of the three Zeeman levels:

$$\Omega_{clock} = \frac{\epsilon_S^*\epsilon_N}{2\Delta}(a_S^*a_N + b_S^*b_N)$$

$$\Omega_+^{00 \rightarrow 11} = \frac{\epsilon_S^*\epsilon_N}{2\Delta}(c_S^*a_N + b_S^*c_N)$$

$$\Omega_-^{00 \rightarrow 1-1} = \frac{\epsilon_S^*\epsilon_N}{2\Delta}(a_S^*c_N + c_S^*b_N)$$

If E_N beam comes in perpendicular to B-field then $a_N = b_N$ If E_S beam comes in parallel to B-field then $c_S = 0$

Now we take ratios of Rabi frequencies:

$$\frac{\Omega_+}{\Omega_-} = \frac{c_S a_N + b_S c_N}{a_S c_N + c_S b_N} = \frac{b_S}{a_S}$$

$$\frac{\Omega_+}{\Omega_{clock}} = \frac{c_N}{a_N} \frac{b_S}{a_S + b_S} = \frac{c_N}{a_N} \left(1 + \frac{\Omega_-}{\Omega_+}\right)^{-1}$$

$$\frac{\Omega_-}{\Omega_{clock}} = \frac{c_N}{a_N} \frac{a_S}{a_S + b_S} = \frac{c_N}{a_N} \left(1 + \frac{\Omega_+}{\Omega_-}\right)^{-1}$$

Numerically:

$$\frac{\Omega_+}{\Omega_-} = \frac{b_S}{a_S} = \frac{0.19}{0.24} = 0.79$$

$$|a_S|^2 + |b_S|^2 = 1 \rightarrow a_S = 0.78 \text{ and } b_S = 0.62$$

So then $E_S = \epsilon_S(0.78\hat{\sigma}^+ + 0.62\hat{\sigma}^-)$. Ideally(if polarization were perfect we would get:

$$E_S = \epsilon_S(0.71\hat{\sigma}^+ + 0.71\hat{\sigma}^-)$$

Then from this we can solve for: $c_N = 0.30$ and $a_N = b_N = 0.68$, which gives $E_N = \epsilon_N(0.68\hat{\sigma}^+ + 0.68\hat{\sigma}^- + 0.30\hat{\pi})$

From this we can see how far away we are from the maximum rabi frequency on the clock states:

$$\Omega_{clock}^{ideal} = 1$$

$$\Omega_{clock}^{actual} = 0.78(0.68) + 0.62(0.68) = 0.95$$

Assuming that the north beam is perpendicular to B-field and south beam is parallel we are at 95% of the maximum Rabi frequency.

Last but not least the C-G coefficients add a factor of 1/3. So our Rabi frequency is:

$$\Omega = \frac{0.244(0.95)g_1g_2}{2(3)\Delta} = 53.82 kHz$$

Experimentally we measure: $\frac{\Omega}{2\pi} = \frac{1}{30\mu s} = 30 kHz$

A.3 Spontaneous Emission

Ultimately it is the spontaneous emission in an experiment that will limit the decoherence times of entangling gates.

The expression for spontaneous emission is:

$$R_{sc} = \frac{S_0\gamma/2}{(1 + S_0 + (2\Delta/\gamma)^2)} \quad (\text{A.11})$$

But in the limit of large detuning, and with polarization taken into account, this can be reduced to:

$$R_{sc} \approx \frac{2(2\pi)S_0}{3} \left(\frac{\gamma}{2}\right)^3 \left(\frac{1}{\Delta}\right)^2 \quad (\text{A.12})$$

Then to obtain the spontaneous emmission rate we must multiply the scatter rate by $\frac{1}{3}$, this is from the Clebsch-Gordon coefficients, there is a $1/3$ probability to scatter a photon from the $(0,0)$ state. This gives us:

$$\frac{\gamma_{se}}{2\pi} = \frac{R_{sc}}{3} = 0.1 \text{ kHz} \quad (\text{A.13})$$

Numerically this is equal to 0.1 kHz. But we measure a probability to be in the bright state of .3 in 1 ms, this gives us a rate of 0.3 kHz. This is a factor of 3 larger than what we would expect.

A.4 Stark Shift

The third effect from the Raman beams that we see is an a.c. stark shift, or a light shift. When we hit the ion with the Raman beams each of the states gets shifted by some amount. This shift is the Stark shift.

The energy shift is defined as:

$$\Delta_{st} = \frac{g^2}{4\Delta} \quad (\text{A.14})$$

But we have to look at the stark shift for each state individually and then subtract them to find the differential stark shift. For the (0,0) state we get:

$$\Delta_{st}^{00} = \frac{g^2}{4\Delta} \left(\frac{1}{2}\sigma_{cg}^+ + \frac{1}{2}\sigma_{cg}^- \right) = \frac{g^2}{4\Delta} \left(\frac{1}{2} \left(\frac{2}{3} \right) + \frac{1}{2} \left(\frac{2}{3} \right) \right) = \frac{2}{3} \frac{g^2}{4\Delta} \quad (\text{A.15})$$

Then for the (1,0) state, and for this state we have to account for the 14.5GHz hyperfine splitting:

$$\Delta_{st}^{10} = \frac{g^2}{4} \frac{1}{(\Delta - hf)} \left(\frac{1}{2}\sigma_{cg}^+ + \frac{1}{2}\sigma_{cg}^- \right) = \frac{g^2}{4} \frac{1}{(\Delta - hf)} \left(\frac{1}{2} \left(\frac{2}{3} \right) + \frac{1}{2} \left(\frac{2}{3} \right) \right) = \frac{2}{3} \frac{g^2}{4} \frac{1}{(\Delta - hf)} \quad (\text{A.16})$$

The total differential stark shift is(substituting the value of g):

$$\frac{\Delta_{st}}{2\pi} = \frac{\gamma^2 S_0}{2(4)} \left(\frac{2}{3} \right) \left(\frac{1}{\Delta} - \frac{1}{\Delta - hf} \right) = 15.2 \text{kHz} \quad (\text{A.17})$$

Experimentally we measure $\frac{\Delta_{st}}{2\pi} = 50 \text{ kHz}$.

APPENDIX B

Decoherence Effects: Temperature and Heating

B.1 Decoherence from temperature and heating

This appendix outlines the decoherence due to temperature and heating during the spin dependent force gates. Here the temperature and heating effects are worked out for the σ_{phi} gate, but the same arguments hold for the σ_z gate.

B.2 Temperature

At finite temperature the system has an average energy $\langle E \rangle = k_B T = \bar{n} \hbar \omega_1$ and follows a Maxwell-Boltzmann distribution with a probability of being in the n^{th} vibrational state defined as

$$P(n) = \left(\frac{n}{1 - \bar{n}} \right)^n e^{-n\hbar\omega_1/k_B T}. \quad (\text{B.1})$$

The displacement operator acts on each initial vibrational level $|n\rangle$, which evolves as

$$|\Psi_n(t)\rangle = \frac{1}{\sqrt{2}} e^{i\Phi(t)} |\uparrow\rangle D(\hat{\alpha}(t)) |n\rangle - \frac{e^{i\phi}}{\sqrt{2}} e^{i\Phi(t)} |\uparrow\rangle D(-\hat{\alpha}(t)) |n\rangle. \quad (\text{B.2})$$

By summing over the Maxwell-Boltzmann distribution of all initial vibrational levels of a single mode, we can find the probability of the ion to be in the $|\downarrow\rangle$ state.

$$P_{thermal}(\downarrow) = \sum_{n=0}^{\infty} \frac{1}{1+\bar{n}} \left(\frac{\bar{n}}{1+\bar{n}} \right)^n |\langle \downarrow | \Psi_n(t) \rangle|^2 \quad (\text{B.3})$$

$$= \frac{1}{2} - \frac{1}{2} e^{-(\bar{n}-1/2)|2\alpha|^2}. \quad (\text{B.4})$$

B.3 Heating

We can model background heating as random displacements in phase space, and then the interference pattern for a given displacement can be calculated and averaged over the distribution of the displacement.

APPENDIX C

1-D Cooling Model and 3-D Monte Carlo simulation

C.1 1-D derivation for steady-state number of atoms cooled to rest in a vapor cell

The following appendix estimates the number of atoms cooled to rest in a vapor cell.

For simplicity we assume the laser beams to have a top-hat profile.

The force on an atom moving with velocity, v , in two counter-propagating laser beams is

$$F_{scat} = \frac{\hbar k \gamma}{2} \left[\frac{s}{1 + s + 4(\delta - u)^2} - \frac{s}{1 + s + 4(\delta + u)^2} \right], \quad (\text{C.1})$$

where the scaled velocity is defined as $u = kv/\gamma$.

To find the capture velocity v_c , that is the maximum velocity an atom can possess and still be slowed to rest within the cooling laser beams, we must integrate the velocity-dependent acceleration $a(v)$

$$\int_{v_c}^0 \frac{vdv}{a(v)} = \int_{x_0}^{x_0+l} dx. \quad (\text{C.2})$$

Here l is the laser beam diameter, x_o is defined to be the edge of the laser beam, and

$$a(v) = \frac{\hbar k \gamma}{2m} \left[\frac{s}{1 + s + 4(\delta - u)^2} - \frac{s}{1 + s + 4(\delta + u)^2} \right]. \quad (\text{C.3})$$

Solving Eq. C.2 gives

$$\frac{-16\hbar k^3 s \delta l}{2m\gamma} = \frac{16}{5} u_c^5 + \frac{8}{3}(1+s-4\delta^2)u_c^3 + (1+s+4\delta^2)^2 u_c. \quad (\text{C.4})$$

This fifth order polynomial can be solved numerically to find the capture velocity, $v_c = \gamma u_c/k$.

From the steady state solution to Eq. 7.1 given above, we get

$$N_{ss} = \frac{fn\hbar\omega l^2 v_c^4}{v_{th}^4 \hbar\omega \sigma_c n + v_{th}^3 \sigma_{ion} IP(I, \delta)}, \quad (\text{C.5})$$

where σ_c is the collision cross section, σ_{ion} is the photoionization cross section, and f is the relative abundance of the isotope of interest.

BIBLIOGRAPHY

- [1] R. FEYNMAN, *There is plenty of room at the bottom.* <http://www.zyvex.com/nanotech/feynman.html>. 1
- [2] P. BENIOFF, *The computer as a physical system: A microscopic quantum mechanical hamiltonian model of computers as represented by turing machines,* Journal of Statistical Physics, 22 (1980), pp. 563–591. 1
- [3] R. P. FEYNMAN, *Simulating physics with computers,* Int. J. Th. Phys., 21 (1981), pp. 467–488. 1
- [4] D. DEUTSCH, *Quantum-theory, the church-turing principle and the universal quantum computer,* Proceedings of the Royal Society of London Series A - Mathematical, Physical, and Engineering Sciences, 400 (1985), pp. 97 – 117. 2, 93
- [5] P. W. SHOR, *Algorithms for quantum computation: Discrete logarithms and factoring,* in Proceedings of the 35th Annual Symposium on the Foundations of Computer Science, New York, 1994, IEEE Computer Society, IEEE Computer Society Press, p. 124. 2
- [6] J. I. CIRAC AND P. ZOLLER, *Quantum computation with cold, trapped ions,* 74 (1995), pp. 4091–4094. 2
- [7] C. MONROE, D. M. MEEKHOF, B. E. KING, W. M. ITANO, AND D. J. WINELAND, *Demonstration of a fundamental quantum logic gate,* 75 (1995), pp. 4714–4717. 2
- [8] C. E. WIEMAN, D. E. PRITCHARD, AND D. J. WINELAND, *Atom cooling, trapping, and quantum manipulation,* Reviews of Modern Physics, 71 (1999), pp. S253–S262. 2
- [9] D. P. DIVINCENZO, *The physical implementation of quantum computation,* Fortschritte der Physik, 48 (2000), pp. 771–783. 3, 38
- [10] W. PAUL, *Electromagnetic traps for charged and neutral particles,* 62 (1990), pp. 531–540. 7
- [11] M. ABRAMOWITZ AND I. A. STEGUN, *Handbook of Mathematical Functions,* U.S. Gov’t. Printing Office, Washington, D.C., 1964. 9, 44
- [12] D. J. WINELAND AND W. M. ITANO, *Laser cooling of atoms,* 20 (1979), pp. 1521–1540. 11
- [13] W. HENSINGER, S. OLMSCHENK, D. STICK, D. HUCUL, M. YEO, M. ACTON, L. DESLAURIERS, C. MONROE, AND J. RABCHUK, *T-junction ion trap array for two-dimensional ion shuttling, storage, and manipulation,* Applied Physics Letters, 88 (2006). 12
- [14] H. G. DEHMELT, *Radiofrequency spectroscopy of stored ions i: Storage,* 3 (1967), pp. 53–72. 14
- [15] M. ACTON, K.-A. BRICKMAN, P. C. HALJAN, P. J. LEE, L. DESLAURIERS, AND C. MONROE, *Near-perfect simultaneous measurement of a qubit register,* Quantum Information and Computation, 6 (2006), pp. 465–482. 23

- [16] P. J. LEE, B. B. BLINOV, K. BRICKMAN, L. DESLAURIERS, M. J. MADSEN, R. MILLER, D. L. MOEHRING, D. STICK, AND C. MONROE, *Atomic qubit manipulations with an electro-optic modulator*, 28 (2003), p. 1852. 30, 54, 100
- [17] L. DESLAURIERS, M. ACTON, B. BLINOV, K. BRICKMAN, P. HALJAN, W. HENSINGER, D. HUCUL, S. KATNIK, R. KOHN, P. LEE, M. MADSEN, P. MAUNZ, S. OLMSCHENK, D. MOEHRING, D. STICK, J. STERK, M. YEO, K. YOUNGE, AND C. MONROE, *Efficient photoionization loading of trapped ions with ultrafast pulses*, 74 (2006), p. 063421. 31, 108
- [18] J. J. SAKURAI, *Modern Quantum Mechanics*, Addison-Wesley, 1993. 39
- [19] *Laser Cooling and Trapping*. 41, 113
- [20] D. J. WINELAND, C. MONROE, W. M. ITANO, D. LEIBFRIED, B. E. KING, AND D. M. MEEKHOF, *Experimental issues in coherent quantum-state manipulation of trapped atomic ions*, J. Res. Natl. Inst. Stand. Tech., 103 (1998), pp. 259–328. 48
- [21] R. OZERI, C. LANGER, J. D. JOST, B. DEMARCO, A. BEN-KISH, B. R. BLAKESTAD, J. BRITTON, J. CHIAVERINI, W. M. ITANO, D. B. HUME, D. LEIBFRIED, T. ROSENBERG, P. O. SCHMIDT, AND D. J. WINELAND, *Hyperfine coherence in the presence of spontaneous photon scattering*, 95 (2005), p. 030403. 52
- [22] G. J. MILBURN, S. SCHNEIDER, AND D. F. V. JAMES, *Ion trap quantum computing with warm ions*, Fortschr. Phys., 48 (2000), pp. 9–11, 801–810. 61, 64
- [23] K. MØLMER AND A. SØRENSEN, *Multiparticle entanglement of hot trapped ions*, 82 (1999), pp. 1835–1838. viii, 61, 68, 81
- [24] J. J. GARCIA-RIPOLL, P. ZOLLER, AND J. I. CIRAC, *Speed optimized two-qubit gates with laser coherent control techniques for ion trap quantum computing*, 91 (2003), p. 157901. 61
- [25] P. J. LEE, K. A. BRICKMAN, L. DESLAURIERS, P. C. HALJAN, L. M. DUAN, AND C. MONROE, *Phase control of trapped ion quantum gates*, J. Opt. B: Quantum Semiclass. Opt., 7 (2005), pp. S371–S383. 66, 81, 97, 100
- [26] Q. A. TURCHETTE, D. KILEPINSKI, B. E. KING, D. LEIBFRIED, D. M. MEEKHOF, C. J. MYATT, M. A. ROWE, C. A. SACKETT, C. S. WOOD, W. M. ITANO, C. MONROE, AND D. J. WINELAND, *Heating of trapped ions from the quantum ground state*, 61 (2000), p. 063418. 72
- [27] D. F. WALLS AND G. J. MILBURN, 31 (1985), p. 2403. 72
- [28] P. C. HALJAN, P. J. LEE, K. A. BRICKMAN, M. ACTON, L. DESLAURIERS, AND C. MONROE, *Entanglement of trapped-ion clock states*, quant-ph/0504163, (2005). 73, 74
- [29] D. LEIBFRIED, B. DEMARCO, V. MEYER, D. LUCAS, M. BARRETT, J. BRITTON, W. M. ITANO, B. JELENKOVIC, C. LANGER, T. ROSENBERG, AND D. J. WINELAND, *Experimental demonstration of a robust, high-fidelity geometric two ion-qubit phase gate*, 422 (2003), pp. 412–415. viii, 79, 81, 120
- [30] C. MONROE, D. M. MEEKHOF, B. E. KING, AND D. J. WINELAND, *A “Schrödinger Cat” superposition state of an atom*, Science, 272 (1996), pp. 1131–1136. 79, 120
- [31] P. C. HALJAN, K.-A. BRICKMAN, L. DESLAURIERS, P. J. LEE, AND C. MONROE, *Spin-dependent forces on trapped ions for phase-stable quantum gates and motional schrödinger cat states*, 94 (2005), p. 153602. 81, 97, 100
- [32] G. VIDAL AND R. F. WERNER, *Computable measure of entanglement*, Phys. Rev. A, 65 (2002), p. 032314. 89

- [33] J. EISERT AND M. B. PLENIO, *A comparison of entanglement measures*, Journal of Modern Optics, (1999). 89
- [34] A. PERES, *Separability criterion for density matrices*, Phys. Rev. Lett., 77 (1996), pp. 1413–1415. 89
- [35] M. HORODECKI, P. HORODECKI, AND R. HORODECKI, *Mixed-state entanglement and distillation: Is there a bound? entanglement in nature?*, Phys. Rev. Lett., 80 (1998), pp. 5239–5242. 89
- [36] W. K. WOOTTERS, *Entanglement of formation of an arbitrary state of two qubits*, 80 (1998), pp. 2245–2248. 92
- [37] M. A. NIELSEN AND I. L. CHUANG, *Quantum Computation and Quantum Information*, Cambridge University Press, 2000. viii, 93, 97, 99, 103
- [38] P. W. SHOR, *Algorithm for fast factoring*, SIAM J. Comp, 26 (1997), p. 1484. 93
- [39] L. K. GROVER, *A framework for fast quantum mechanical algorithms*, in Proc. 20th ACM Symp. Theory Comp., New York, 1998, ACM Press, pp. 53–62. 93
- [40] N. J. CERF, L. K. GROVER, AND C. P. WILLIAMS, *Nested quantum search and structured problems*, Phys. Rev. A, 61 (2000), p. 032303. 93
- [41] D. DEUTSCH AND R. JOZSA, *Rapid solution of problems by quantum computation*, 439 (1992), pp. 553–558. 94
- [42] S. GULDE, M. RIEBE, G. P. T. LANCASTER, C. BECHER, J. ESCHNER, H. HAFFNER, F. SCHMIDT-KALER, I. L. CHUANG, AND R. BLATT, *Implementation of the deutsch-jozsa algorithm on an ion-trap quantum computer*, Nature, 421 (2003), pp. 48–50. 95
- [43] L. M. K. VANDERSYPEN, M. STEFFEN, G. BREYTA, C. S. YANNONI, M. H. SHERWOOD, AND I. L. CHUANG, *Experimental realization of shor’s quantum factoring algorithm using nuclear magnetic resonance*, Nature, 414 (2001), pp. 883–887. 95
- [44] L. K. GROVER, *Quantum mechanics helps in searching for a needle in a haystack*, PRL, 79 (1997), pp. 325–328. 96
- [45] G. BRASSARD, *Searching a Quantum Phone Book*, Science, 275 (1997), pp. 627–628. 96
- [46] M. BOYER, G. BRASSARD, P. HOYER, AND A. TAPP, *Tight bounds of quantum searching*, Fortschritte der Physik, 46 (1998), p. 493. 96
- [47] M. FENG, *Grover search with pairs of trapped ions*, Phys. Rev. A, 63 (2001), p. 052308. 97
- [48] C. D. HILL AND H.-S. GOAN, *Comment on “grover search with pairs of trapped ions”*, Physical Review A (Atomic, Molecular, and Optical Physics), 69 (2004), p. 056301. 97
- [49] I. L. CHUANG, N. GERSHENFELD, AND M. KUBINEC, *Experimental implementation of fast quantum searching*, Phys. Rev. Lett., 80 (1998), pp. 3408–3411. 97
- [50] J. A. JONES, M. MOSCA, AND R. H. HANSEN, *Implementation of a quantum search algorithm on a quantum computer*, Nature, 393 (1998), pp. 344–346. 97
- [51] M. S. ANWAR, D. BLAZINA, H. A. CARTERET, S. B. DUCKETT, AND J. A. JONES, *Implementing grover’s quantum search on a para-hydrogen based pure state nmr quantum computer*, Chemical Physics Letters, 400 (2004), pp. 94–97. 97
- [52] P. G. KWIAT, J. R. MITCHELL, P. D. D. SCHWINDT, AND A. G. WHITE, *Grover’s search algorithm: an optical approach*, Journal of Modern Optics, 47 (2000), pp. 257–266. 97

- [53] P. WALTHER, K. J. RESCH, T. RUDOLPH, E. SCHENCK, H. WEINFURTER, V. VEDRAL, M. ASPELMEYER, AND A. ZEILINGER, *Experimental one-way quantum computing*, Nature, 434 (2005), pp. 169–176. 97
- [54] J. AHN, T. C. WEINACHT, AND P. H. BUCKSBAUM, *Information Storage and Retrieval Through Quantum Phase*, Science, 287 (2000), pp. 463–465. 97
- [55] M. RIEBE, H. HAFFNER, C. F. ROOS, W. HANSEL, J. BENHELM, G. P. T. LANCASTER, T. W. KORBER, C. BECHER, F. SCHMIDT-KALER, D. F. V. JAMES, AND R. BLATT, *Deterministic quantum teleportation with atoms*, Nature, 429 (2004), pp. 734–737. 97
- [56] M. D. BARRETT, J. CHIAVERINI, T. SCHAETZ, J. BRITTON, W. M. ITANO, J. D. JOST, E. KNILL, C. LANGER, D. LEIBFRIED, R. OZERI, AND D. J. WINELAND, *Deterministic quantum teleportation of atomic qubits*, Nature, 429 (2004), pp. 737–739. 97, 104
- [57] T. SCHAETZ, M. D. BARRETT, D. LEIBFRIED, J. CHIAVERINI, J. BRITTON, W. M. ITANO, J. D. JOST, C. LANGER, AND D. J. WINELAND, *Quantum dense coding with atomic qubits*, Physical Review Letters, 93 (2004), p. 040505. 97, 104
- [58] J. CHIAVERINI, J. BRITTON, D. LEIBFRIED, E. KNILL, M. D. BARRETT, R. B. BLAKESTAD, W. M. ITANO, J. D. JOST, C. LANGER, R. OZERI, T. SCHAETZ, AND D. J. WINELAND, *Implementation of the semiclassical quantum fourier transform in a scalable system*, Science, 308 (2005), pp. 997–1000. 97, 104
- [59] P. C. HALJAN, P. J. LEE, K.-A. BRICKMAN, M. ACTON, L. DESLAURIERS, AND C. MONROE, *Entanglement of trapped-ion clock states*, Physical Review A (Atomic, Molecular, and Optical Physics), 72 (2005), p. 062316. 97, 100, 103, 104
- [60] A. SØRENSEN AND K. MØLMER, *Quantum computation with ions in thermal motion*, 82 (1999), pp. 1971–. 97, 100, 104
- [61] J. L. DODD, T. C. RALPH, AND G. J. MILBURN, *Experimental requirements for grover’s algorithm in optical quantum computation*, Phys. Rev. A, 68 (2003), p. 042328. 98, 103
- [62] Q. A. TURCHETTE, D. KILEPINSKI, B. E. KING, D. LEIBFRIED, D. M. MEEKHOF, C. J. MYATT, M. A. ROWE, C. A. SACKETT, C. S. WOOD, W. M. ITANO, C. MONROE, AND D. J. WINELAND, *Heating of trapped ions from the quantum ground state*, 61 (2000), p. 063418. 104
- [63] L. DESLAURIERS, P. C. HALJAN, P. J. LEE, K.-A. BRICKMAN, B. B. BLINOV, M. J. MADSEN, AND C. MONROE, *Zero-point cooling and low heating of trapped cd ions*, 70 (2004), p. 043408. 104
- [64] A. BARENCO, C. H. BENNETT, R. CLEVE, D. P. DiVINCENZO, N. MARGOLUS, P. SHOR, T. SLEATOR, J. A. SMOLIN, AND H. WEINFURTER, *Elementary gates for quantum computation*, Phys. Rev. A, 52 (1995), pp. 3457–3467. 104
- [65] F. SCHMIDT-KALER, H. HAFFNER, M. RIEBE, S. GULDE, G. P. T. LANCASTER, T. DEUSCHLE, C. BECHER, C. F. ROOS, J. ESCHNER, AND R. BLATT, *Realization of the cirac-zoller controlled-not quantum gate*, Nature, 422 (2003), pp. 408–411. 104, 120
- [66] M. A. ROWE, A. BEN-KISH, B. DEMARCO, D. LEIBFRIED, V. MEYER, J. BEALL, J. BRITTON, J. HUGHES, W. M. ITANO, B. JELENKOVIC, C. LANGER, T. ROSENBOAND, AND D. J. WINELAND, *Transport of quantum states and separation of ions in a dual rf ion trap*, Quantum Information and Computation, 2 (2002), pp. 257–271. 104
- [67] D. KIELPINSKI, C. MONROE, AND D. J. WINELAND, *Architecture for a large-scale ion-trap quantum computer*, Nature, 417 (2002), pp. 709–711. 104

- [68] C. W. HOYT, Z. W. BARBER, C. W. OATES, T. M. FORTIER, S. A. DIDDAMS, AND L. HOLMBERG, *Observation and absolute frequency measurements of the [sup 1]s[sub 0]-[sup 3]p[sub 0] optical clock transition in neutral ytterbium*, Physical Review Letters, 95 (2005), p. 083003. 105, 119
- [69] J. WEINER, V. S. BAGNATO, S. ZILIO, AND P. S. JULIENNE, *Experiments and theory in cold and ultracold collisions*, Rev. Mod. Phys., 71 (1999), pp. 1–85. 105
- [70] A. J. LEGGETT, *Bose-einstein condensation in the alkali gases: Some fundamental concepts*, Rev. Mod. Phys., 73 (2001), pp. 307–356. 105
- [71] C. W. OATES, F. BONDU, R. W. FOX, AND L. HOLMBERG, *A diode-laser optical frequency standard based on laser-cooled ca atoms: Sub-kilohertz spectroscopy by optical shelving detection*, Eur. Phys. J. D, 7 (1999), p. 449. 105
- [72] K. SENGSTOCK, U. STERR, J. H. MÄLLER, V. RIEGER, D. BETTERMANN, AND W. ERTMER, *Optical ramsey spectroscopy on laser-trapped and thermal mg atoms*, Applied Physics B: Lasers and Optics, 59 (1994), pp. 99–115. 105
- [73] X. XU, T. H. LOFTUS, M. J. SMITH, J. L. HALL, A. GALLAGHER, AND J. YE, *Dynamics in a two-level atom magneto-optical trap*, Phys. Rev. A, 66 (2002), p. 011401. 105, 114, 119
- [74] C. Y. PARK AND T. H. YOON, *Efficient magneto-optical trapping of yb atoms with a violet laser diode*, Phys. Rev. A, 68 (2003), p. 055401. 105, 118
- [75] M. CETINA, A. GRIER, J. CAMPBELL, I. CHUANG, AND V. VUELTIĆ, *Bright source of cold ions for surface-electrode traps*. arxiv:physics/0702025. 105
- [76] R. CÔTÉ, V. KHARCHENKO, AND M. D. LUKIN, *Mesoscopic molecular ions in bose-einstein condensates*, Phys. Rev. Lett., 89 (2002), p. 093001. 105
- [77] Z. IDZIASZEK, T. CALARCO, AND P. ZOLLER. arxiv:physics/0704.1037. 105
- [78] T. E. CHUPP, R. J. HOARE, R. L. WALSWORTH, AND B. WU, *Spin-exchange-pumped ³he and ¹²⁹xe zeeman masers*, Phys. Rev. Lett., 72 (1994), pp. 2363–2366. 105
- [79] C. MONROE, W. SWANN, H. ROBINSON, AND C. WIEMAN, *Very cold trapped atoms in a vapor cell*, Phys. Rev. Lett., 65 (1990), pp. 1571–1574. 106
- [80] T. W. D. HOFFMAN, P. FENG, *Measurements of rb trap-loss collision spectra*, J. Opt. Soc. Am. B, 11 (1994), p. 712. 106
- [81] M. S. SANTOS, P. NUSSENZVEIG, L. G. MARCASSA, K. HELMERSON, J. FLEMMING, S. C. ZILIO, AND V. S. BAGNATO, *Simultaneous trapping of two different atomic species in a vapor-cell magneto-optical trap*, Phys. Rev. A, 52 (1995), pp. R4340–R4343. 106
- [82] T. P. DINNEEN, K. R. VOGEL, E. ARIMONDO, J. L. HALL, AND A. GALLAGHER, *Cold collisions of sr* – sr in a magneto-optical trap*, Phys. Rev. A, 59 (1999), pp. 1216–1222. 106
- [83] K. LINDQUIST, M. STEPHENS, AND C. WIEMAN, *Experimental and theoretical study of the vapor-cell zeeman optical trap*, Phys. Rev. A, 46 (1992), pp. 4082–4090. 106
- [84] S. C. K. E. GIBBLE, S. KASAPI, *Improved magneto-optic trapping in a vapor cell*, Optics Letters, (1992). 106
- [85] T. WALKER, D. SESKO, AND C. WIEMAN, *Collective behavior of optically trapped neutral atoms*, Phys. Rev. Lett., 64 (1990), pp. 408–411. 108
- [86] D. N. MADSEN AND J. W. THOMSEN, *Measurement of absolute photo-ionization cross sections using magnesium magneto-optical traps*, Journal of Physics B: Atomic, Molecular and Optical Physics, 35 (2002), pp. 2173–2181. 108

- [87] K. L. CORWIN, Z. T. LU, C. F. HAND, R. J. EPSTEIN, AND C. E. WIEMAN, *Frequency-stabilized diode laser with the zeeman shift in an atomic vapor*, Appl. Opt., (1998). 109
- [88] J. M. REEVES, O. GARCIA, AND C. A. SACKETT, *Temperature stability of a dichroic atomic vapor laser lock*, Appl. Opt., (2006). 109
- [89] R. R. ADZHIMAMBETOV, I. S. MUZHDAEVA, A. T. TURSUNOV, AND Ā. Ā. KHALILOV, *Study of the cds crystal evaporation kinetics by laser step atomic photoionization*, Technical Physics, 48 (2003), pp. 1020–1023. 111
- [90] J. FLEMMING, L. G. MARCASSA, R. J. HOROWICZ, S. C. ZILIO, AND V. S. BAGNATO, *Enhanced loading of a two-color vapor-cell magneto-optical trap for sodium atoms*, Optics Letters, (1995). 118
- [91] T. W. H. V. VULETIC AND C. ZIMMERMANN, *Steep magnetic trap for ultra cold atoms*, Europhys. Lett, (1996). 118
- [92] J. P. HOME, M. J. McDONNELL, D. M. LUCAS, G. IMREH, B. C. KEITCH, D. J. SZWER, N. R. THOMAS, S. C. WEBSTER, D. N. STACEY, AND A. M. STEANE, *Deterministic entanglement and tomography of ion–spin qubits*, New Journal of Physics, 8 (2006), p. 188. 120

ABSTRACT

Implementation of Grover's Quantum Search Algorithm with Two Trapped Cadmium
Ions

by

Kathy-Anne Brickman

Chair: Christopher Monroe

Over the past decade, the field of trapped ion quantum computing has emerged as one of the leaders in quantum information processing due the level of manipulation available and the long coherence times possible in the system. As this thesis will demonstrate, all of the necessary building blocks for a quantum computer have been exhibited in ion traps and small scale quantum algorithms have been implemented in this system.

In the trapped ion system presented here, quantum bits (qubits) consist of the first order magnetic field insensitive ground state hyperfine levels of $^{111}\text{Cd}^+$. The qubits are manipulated via both resonant and off-resonant coherent laser interactions. We experimentally realize Grover's quantum search algorithm over a space of $N=4$ elements with $n=2$ trapped $^{111}\text{Cd}^+$ ion qubits. One of the four states is marked, and with a single query it is recovered, on average, with a 60% probability. This exceeds the performance of any

possible classical search, which can only succeed with 50% probability following a single query. The algorithm consists of two Molmer-Sorensen entangling gates, that utilize bichromatic stimulated Raman transitions to create a spin dependent force on the ions, paired with several single-qubit rotations and near-perfect qubit measurements. The spectral arrangement of the Raman beams is tailored to suppress phase noise accumulation between gates. This suppression is critical for reliably performing consecutive operations during the algorithm.

Additionally, this thesis discusses the possibility of combining trapped ions with trapped neutral atoms for the purpose studying ultra-cold charge exchange interactions. It may be possible to conceal quantum information, initially prepared in an ionic qubit, inside a pure nuclear spin qubit for the purpose of transportation and storage. As a first step towards this investigation, we present the laser-cooling and confinement of Cd atoms in a magneto-optical trap, and characterize the loading process from the background Cd vapor. The trapping laser drives the $^1S_0 \rightarrow ^1P_1$ transition at 229 nm in this two-electron (valence electron) atom and also photoionizes atoms directly from the 1P_1 state. This photoionization overwhelms the other loss mechanisms and allows a direct measurement of the photoionization cross section, which we measure to be $2(1) \times 10^{-16} \text{ cm}^2$ from the 1P_1 state.

ABSTRACT

Implementation of Grover's Quantum Search Algorithm with Two Trapped Cadmium
Ions

by

Kathy-Anne Brickman

Chair: Christopher Monroe

Over the past decade, the field of trapped ion quantum computing has emerged as one of the leaders in quantum information processing due the level of manipulation available and the long coherence times possible in the system. As this thesis will demonstrate, all of the necessary building blocks for a quantum computer have been exhibited in ion traps and small scale quantum algorithms have been implemented in this system.

In the trapped ion system presented here, quantum bits (qubits) consist of the first order magnetic field insensitive ground state hyperfine levels of $^{111}\text{Cd}^+$. The qubits are manipulated via both resonant and off-resonant coherent laser interactions. We experimentally realize Grover's quantum search algorithm over a space of $N=4$ elements with $n=2$ trapped $^{111}\text{Cd}^+$ ion qubits. One of the four states is marked, and with a single query it is recovered, on average, with a 60% probability. This exceeds the performance of any

possible classical search, which can only succeed with 50% probability following a single query. The algorithm consists of two Molmer-Sorensen entangling gates, that utilize bichromatic stimulated Raman transitions to create a spin dependent force on the ions, paired with several single-qubit rotations and near-perfect qubit measurements. The spectral arrangement of the Raman beams is tailored to suppress phase noise accumulation between gates. This suppression is critical for reliably performing consecutive operations during the algorithm.

Additionally, this thesis discusses the possibility of combining trapped ions with trapped neutral atoms for the purpose studying ultra-cold charge exchange interactions. It may be possible to conceal quantum information, initially prepared in an ionic qubit, inside a pure nuclear spin qubit for the purpose of transportation and storage. As a first step towards this investigation, we present the laser-cooling and confinement of Cd atoms in a magneto-optical trap, and characterize the loading process from the background Cd vapor. The trapping laser drives the $^1S_0 \rightarrow ^1P_1$ transition at 229 nm in this two-electron (valence electron) atom and also photoionizes atoms directly from the 1P_1 state. This photoionization overwhelms the other loss mechanisms and allows a direct measurement of the photoionization cross section, which we measure to be $2(1) \times 10^{-16} \text{ cm}^2$ from the 1P_1 state.